SYNTHESIS AND STUDY OF PALLADIUM-CONTAINING NANOMATERIALS FOR HYDROGEN TECHNOLOGIES

A Thesis Presented to

The Faculty of Graduate Studies

Lakehead University

By

BRIAN D. ADAMS

In partial fulfillment of the requirements for the degree of

Master of Science

September 2010

Abstract

We are currently facing a climate change and global warming effect due to the emission of greenhouse gases from our existing energy sources. A hydrogen-based economy is one solution to uphold our standard of living while lowering our carbon emissions. Palladium has the potential to play a major role in many aspects of the hydrogen-based economy, from purifying hydrogen to harnessing the energy via fuel cells and storing hydrogen as PdH_x. In my M.Sc. study, Pd-based nanomaterials have been synthesized and examined for their applications in various hydrogen technologies. Surface properties of the synthesized Pd-based nanomaterials were characterized by scanning electron microscopy (SEM), transmission electron microscopy (TEM), energy dispersive X-ray spectrometry (EDS), X-ray diffraction (XRD), X-ray photoelectron spectroscopy (XPS), and N_2 gas adsorption/desorption. Electrochemical analysis of the fabricated materials was performed using cyclic voltammetry (CV), linear sweep voltammetry (LSV), and chronoamperometry (CA). Other characterization methods were also applied such as inductively-coupled plasma atomic emission spectroscopy (ICP-AES), density functional theory (DFT) calculations, and hydrogen gas adsorption/absorption.

For the first time, PdCd nanostructures were prepared by a hydrothermal reduction technique and their hydrogen electrosorption properties were examined. A large expansion of the lattice constant due to the α (solid solution) to β-phase (metal hydride) hydrogen transition causes hydrogen embrittlement. For the Pd-Cd nanostructures, the α to β phase transition was determined to be the slowest step in the absorption process. This transition was practically eliminated when the composition was $Pd_{0.85}Cd_{0.15}$ which increases the kinetics of hydrogen absorption.

Three different hydrogen dissociation catalysts (Pd, PdAg, and PdCd) were dispersed onto surfaces of activated carbon; their effect on the hydrogen gas adsorption properties was systematically studied. At room temperature, hydrogen spillover was observed from the catalysts to the carbon material. The hydrogen capacity is related to the adsorption strength of the catalyst particle surface atoms which is verified with DFT calculations. The hydrogen capacity of the PdCd dispersed activated carbon sample was increased by 108% due to spillover hydrogen from the PdCd nanoparticles.

Pd/C, Pt/C, and PdPt/C catalysts were fabricated and tested for their activity towards the electrochemical reduction of H_2O_2 in acidic conditions. The PdPt catalysts outperformed both Pt and Pd in terms of hydrogen peroxide reduction activity. The catalyst of composition $Pd_{0.25}Pt_{0.75}$ had the greatest activity towards hydrogen peroxide electroreduction.

The adsorption of the catalytically poisoning species, carbon monoxide, was also examined on Pd, PdPt, and PdAu nanostructures. The relative quantities of CO molecules adsorbed to surface of the catalysts decrease in the order of: PdPt > Pd > PdAu. It was found that the possible adsorption sites of CO can be tuned by alloying Pd with metals to which CO has different binding strengths.

The work done in this thesis shows that by alloying Pd with other metals, both geometric and electronic properties are changed drastically. This has a major influence on the applications of Pd for hydrogen technologies.

Acknowledgements

Table of Contents

List of Abbreviations and Symbols

Abbreviation   Name

6-31G*	A Polarized Split-Valence Double-ζ Basis Set
ATR	Attenuated Total Reflectance
AES	Atomic Emission Spectroscopy
AFC	Alkaline Fuel Cell
AUG-CC-PVTZ	Augmented Correlation-Consistent Polarized Valence Triple-ζ Basis Set
B3LYP	Beck, Three-Parameter, Lee-Yang-Par Functional
BET	Brunauer, Emmett, and Teller
BJH	Barret-Jayner-Halenda
BSSE	Basis Set Superposition Error
CA	Chronoamperometry
CV	Cyclic Voltammetry
DA	Dubinin Astakhov
DBFC	Direct Borohydride Fuel Cell
DFAFC	Direct Formic Acid Fuel Cell
DFT	Density Functional Theory
E	Potential
E_{ads}	Adsorption Energy
EDS	Energy Dispersive Spectroscopy
FTIR	Fourier Transform Infrared Spectroscopy
FWHM	Full Width at Half Maximum
HOMO	Highest Occupied Molecular Orbital
HOR	Hydrogen Oxidation Reaction
ICP	Inductively Coupled Plasma
j	Current Density
LANL2DZ	Los Alamos National Laboratory 2-Double-ζ Basis Set
LUMO	Lowest Unoccupied Molecular Orbital
LVE	Limited Volume Electrode

LSV	Linear Sweep Voltammetry
MCFC	Molten Carbonate Fuel Cell
MSFC	Metal Semi-Fuel Cells
NLDFT	Non-local Density Functional Theory
ORR	Oxygen Reduction Reaction
PAC200	Commercially Available Norit PAC 200 Activated Carbon
PAFC	Phosphoric Acid Fuel Cell
PBE	Perdew-Burke-Ernzerhof Functional
PEMFC	Proton Exchange Membrane Fuel Cell
Q_{CO}	Carbon Monoxide Oxidation Charge
Q_H	Hydrogen Oxidation Charge
QSDFT	Quenched Solid Density Functional Theory
RDE	Rotating Disk Electrode
SCE	Saturated Calomel Electrode
SEM	Scanning Electron Microscopy
SHE	Standard Hydrogen Electrode
SOFC	Solid Oxide Fuel Cell
TEM	Transmission Electron Microscopy
XPS	X-ray Photoelectron Spectroscopy
XRD	X-ray Diffraction

Chapter 1

Introduction

1.1 The Hydrogen Economy

Our global society has become strongly dependent on the excessive use of energy. Technological advancement during the past few decades has led to improved living conditions of people in developed countries, and every year, a larger percentage of our global population seeks to improve their standard of living at the expense of the environment.[1] Industrial growth coupled with the desire to improve quality of life has come at a major cost. Oil, coal and natural gas have been extensively used to power automobiles, power plants and factories, causing a dramatic build-up of greenhouse gases in the atmosphere.[2] We are currently facing a climate change and global warming effect due to the emission of greenhouse gases from our existing energy sources.

Unlike fossil fuels, the combustion of hydrogen does not generate CO_2. On the other hand, hydrogen almost never occurs by itself in nature (at least on Earth) and, therefore, must first be produced. For this reason, hydrogen should not be considered as an energy source, but rather an energy carrier. The ultimate goal of a hydrogen-based economy is to produce hydrogen with little or no greenhouse gas emission, to store or transport the hydrogen, and then to harness the energy by combustion or with a fuel cell.[3]

Hydrogen can be produced from either hydrocarbons or water using a wide array of techniques. Currently, the majority of H_2 is produced in the form of *syngas*, generated by gasification of coal, heavy oil, natural gas or other hydrocarbons (equation 1.1), or by steam reforming of methane (equation 1.2). The water gas shift reaction (equation 1.3) is then commonly used to obtain more hydrogen.

$$C_aH_b + [Ox] \rightarrow xH_2 + yCO + zCO_2 \tag{1.1}$$

$$CH_4 + H_2O \rightarrow 3H_2 + CO \tag{1.2}$$

$$CO + H_2O \rightarrow H_2 + CO_2 \tag{1.3}$$
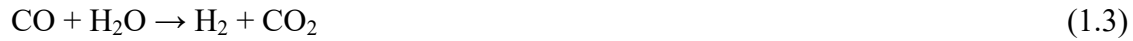
In equation 1.1, C_aH_b represents the hydrocarbon ($a \geq 1$, $b \geq a$) and [Ox] represents an oxidant such as H_2O, O_2, or CO_2. All of these production techniques from fossil fuels produce large amounts of CO_2. An alternative approach is biomass gasification which is heating organic materials such as wood and crop wastes so that they release H_2 and carbon monoxide.[1] This technique is carbon-neutral, as any carbon emissions are offset by the CO_2 absorbed by the plants during their growth. The last, and most environmentally friendly production technique, is the electrolysis of water using off-peak power or power from renewable sources such as wind turbines or solar cells.

Once hydrogen fuel has been produced, the energy can be harnessed either by combustion to produce heat, or in a fuel cell to produce electricity. A fuel cell is an electrochemical device that converts the chemical energy in a fuel (such as hydrogen) and an oxidant (eg., oxygen, pure or in air) directly into electricity. The main by-products are water and heat. There are five different types (Table 1.1), which are categorized according to the electrolyte that they use: (1) proton exchange membrane fuel cell (PEMFC), (2) alkaline fuel cell (AFC), (3) phosphoric acid fuel cell (PAFC), (4) molten carbonate fuel cell (MCFC), and (5) solid oxide fuel cell (SOFC). There is also a subclass of PEMFC, called direct X fuel cells, where X is a small organic molecule fuel such as methanol or formic acid that is fed directly into the fuel cell rather than being reformed into H_2 first. These are applicable for small, portable electronics, such as laptops and cell phones, due to the low temperature of operation (0-60 °C).[4]

Table 1.1. General characteristics of some types of fuel cells.[4]

	PEMFC	AFC	PAFC	MCFC	SOFC
Primary Applications	Automotive and stationary power	Space vehicles and drinking water	Stationary power	Stationary power	Vehicle auxiliary power
Electrolyte	Polymer (plastic) membrane	Concentrated (30-50%) KOH in H_2O	Concentrated 100% phosphoric acid	Molten Carbonate retained in a ceramic matrix of $LiAlO_2$	Yttrium-stabilized Zirkondioxide
Operating Temperature Range	50-100 °C	50-200 °C	150-220 °C	600-700 °C	700-1000 °C
Charge Carrier	H^+	OH^-	H^+	CO_3^{2-}	O^{2-}
Catalysts	Pt-based	Pt-based	Pt-based	Ni-based	Perovskites
Primary Fuel	H_2	H_2	H_2	H_2, CO, CH_4	H_2, CO
Start-up Time	Sec-min	Sec-min	Hours	Hours	Hours
Power Density (kW/m^3)	3.8-6.5	~1	0.8-1.9	1.5-2.6	0.1-1.5
Combined Cycle Efficiency	50-60%	50-60%	55%	55-65%	55-65%

Hydrogen storage and transportation are perhaps the most challenging issues to overcome before a hydrogen-based economy becomes a reality. Hydrogen is gaseous at room temperature and forms explosive mixtures with air. As a reference, a compact passenger vehicle powered by a fuel cell would require approximately 4 kg of H_2 for a driving range of 400 km.[5] To store hydrogen in a gas tank at ambient temperature, 700 atm is needed for compression to reasonable volume. This pressure is dangerously high. Storage of hydrogen in the liquid state requires a large energy consumption for liquefication at 20 K and also suffers from "boil-off".

There are three categories of materials currently under study for hydrogen storage in automotive applications: organic chemical hydrides; metal hydrides; and carbon materials for

physisorption. The critical properties they should possess are (i) light weight, (ii) inexpensive and readily available, (iii) high volumetric and gravimetric density of hydrogen, (iv) fast sorption kinetics, (v) easy to activate, (vi) low temperature of dissociation or decomposition, (vii) appropriate thermodynamic properties, (viii) long-term cycling stability, and (ix) high degree of reversibility.[6] In 2002 the US Department of Energy set quantitative goals for the hydrogen content of storage devices (6 wt% by 2010, then 9 wt% by 2015). These targets have not been met and the DOE has revised the target to 5.5 wt% for 2015.[7]

1.2 Catalytic and Hydrogen Absorbing Properties of Pd

Absorption of hydrogen gas into Pd was discovered by Graham[8] in 1866 and electrolytic insertion was first examined in 1939.[9] PdH_x is possibly the most widely studied metal hydride, owing to its large volumetric hydrogen capacity at room temperature, the noble character of Pd, the availability of pure samples, and the fact that no surface treatments of the bulk metal are usually required.[10] People have studied the absorption/desorption process of PdH_x in terms of thermodynamics, kinetics, and structural properties ever since its discovery and, as a result, it is perhaps the best-understood metal hydride.

The dissociative adsorption of molecular hydrogen on transition metal surfaces is the first elementary step in a catalytic hydrogenation reaction.[11] Palladium is a widely used catalyst for the hydrogenation of alkenes and alkynes.[12] Ni is also widely used for this purpose, but requires higher temperatures, whereas Pd dissociate the hydrogen molecule at room temperature. Molecular H_2 dissociation is also the first step in absorption and the subsequent formation of metal hydrides. On most metals (other than Pd), this requires energy to overcome an activation barrier and is the reason that high pressures of hydrogen or high temperatures are required. The temperatures and equilibrium pressures for the formation of various metal hydrides are compared

in Table 1.2. It can be seen that Pd is the only metal which can form a hydride at ambient conditions. The superior hydrogen dissociative properties of Pd enable it to be used as a catalyst to facilitate hydrogen absorption and desorption in other metal hydrides. On top of that, its selectivity for hydrogen, fast sorption kinetics, and reversibility of hydride formation, allow membranes made from Pd-based alloys to purify hydrogen gas up to 99.99999%.[13]

Table 1.2. Intermetallic compounds and their hydrogen storage properties.[14]

Type	Metal	Hydride	Structure	wt.% H	P_{eq}, T
Elemental	Pd	$PdH_{0.6}$	Fm3m	0.56	0.02 bar, 298 K
AB_5	$LaNi_5$	$LaNi_5H_6$	P6/mmm	1.37	2 bar, 298 K
AB_2	ZrV_2	$ZrV_2H_{5.5}$	Fd3m	3.01	10-8 bar, 323 K
AB	FeTi	$FeTiH_2$	Pm3m	1.89	5 bar, 303 K
A_2B	Mg_2Ni	Mg_2NiH_4	P6222	3.59	1 bar, 555 K
Body-centered cubic	TiV_2	TiV_2H_4	b.c.c.	2.60	10 bar, 313 K

Carbon-supported Pt is commonly used as both the anode and cathode electrocatalysts in low temperature fuel cells fuelled with hydrogen or small organic molecules.[15] The cost of Pt and the limited world supply are barriers to the widespread use of these types of fuel cells. Pt and Pd belong to the same group in the periodic table, have the same face-centered cubic crystal structure, and have similar atomic size. Pd is of great interest as a substitute material for Pt, either partially or completely, due to its chemical similarity to Pt, but at approximately 1/5 of the cost and 50 times the abundance on Earth.[15] So far in 2010, the average spot price of Palladium has been roughly $471 USD/OZ (www.kitco.com). This price is still too high to extensively use Pd for industrial applications. However, with appropriate cost-saving research methods such as alloying with less expensive metals and using nanoscale materials, palladium has the potential to play a major role in many aspects of the hydrogen economy, from purifying hydrogen to harnessing the energy via fuel cells and storing hydrogen as PdH_x.

1.3 Hydrogen Purification

The performance of PEMFCs strongly depends on the purity of the hydrogen feed. A high purity gas stream of hydrogen is crucial since certain species act as poisons to the catalysts even in very low concentrations.[16] In the case of CO, a strong adsorbing species, less than 10 ppm is usually required. If hydrogen is not produced via electrolysis, the application of a highly selective palladium-based membrane can be used to purify the gas. Commercially available small-scale hydrogen purification units using palladium-based dense metallic membranes have been used to selectively produce high purity hydrogen (e.g., 99.99999%) for specialized industrial applications.[13] The cost of Pd-alloy membranes used for hydrogen separation can be reduced by depositing a thin Pd-alloy layer on a suitable gas-permeable porous substrate to form a composite membrane. Almost all development efforts are focused on preparing thin and defect-free Pd-alloy layers.

Hydrogen permeation through palladium occurs in seven steps: (1) gas phase diffusion to the feed membrane surface; (2) dissociative adsorption on the surface; (3) passage from the surface to the membrane bulk; (4) diffusion through the bulk to the permeate side; (5) passage from bulk to surface; (6) associative desorption from the permeate surface; and (7) gas phase diffusion away from the permeate surface.[16] Strongly adsorbing poison species, such as CO and H_2S, can pose difficulties for hydrogen in step (2). Another major problem for membranes made from pure Pd is hydrogen embrittlement.[17]

The absorption of hydrogen into Pd occurs in two distinct phases. At low concentrations of hydrogen (solid solution) the α-phase appears, which possesses a lattice constant very similar to pure Pd. At high concentrations of hydrogen (metal hydride), the β phase forms, with an increase in the lattice constant. Above a critical hydrogen concentration α_{max}, bulk PdH_x enters

the α/β-phase co-existence region, and a portion of the system undergoes a first-order phase transition to the β-phase until another critical hydrogen concentration β_{min} is reached and the system transforms entirely to the β-phase.[10]

Associated with the α/β-phase transition is a dilation of the face-centered cubic lattice constant due to increasing concentration of hydrogen atoms occupying octahedral interstitial sites. This large expansion of the lattice constant can cause cracking of the membrane (hydrogen embrittlement). In general, β_{min} decreases and α_{max} increases with an increase in temperature. As a result, the width of the co-existence region or miscibility gap (β_{min} - α_{max}) decreases with an increase in temperature until a critical temperature T_c = 570 K (bulk Pd) is reached. Above T_c, the miscibility gap is no longer observed. For this reason, membranes made from pure Pd are held above 570 K to avoid hydrogen embrittlement.[10]

It has been shown in the past that the size of the Pd particles has an effect on this phase transition. The miscibility gap and T_c are decreased with nanosized particles. Yamauchi et al.[18] compared hydrogen absorption isotherms for Pd black (bulk Pd) and Pd nanoparticles and found that the hysteresis in the pressure-composition isotherm of Pd particles (2.6±0.4 nm in diameter) disappeared at 393 K. The absence of hysteresis, in addition to the absence of a plateau region in the equilibrium pressure, implies that the critical state of the α- and β-phases was attained. The critical temperature (T_c) in the bulk system is reported to be 565 K. Thus, a remarkable decrease in T_c was recognized in Pd nanoparticles. This particular behavior of the Pd nanoparticles is one that arises from the nanosize effects on hydrogen storage in Pd.[18]

By alloying palladium with other metals, the lattice sizes and the number of vacant d-band holes change remarkably. The hydrogen solubility in different phases, the plateau pressure and the extent of the miscibility gap varies from alloy to alloy. This also occurs with varying the

amount of alloying elements.[19] Hydrogen embrittlement can also be controlled at ambient temperatures by alloying Pd with metals which have larger atoms than Pd itself. In PdAg, for example, which is the most common hydrogen extraction metal alloy used by industry,[20] the lattice has already been expanded by silver atoms and is thus less influenced by hydrogen than a pure Pd lattice.[21]

From a general heterogeneous catalysis point of view, it is usually considered that poisons (e.g., sulfur, arsenic, thiourea, and carbon monoxide) deactivate catalyzed reactions through irreversible adsorption on the metal at active centers.[22] There is competitive adsorption between the poison and the reactant at the catalyst surface. In the case of Pd-based hydrogen selective membranes, poisoning species tend to inhibit the dissociative adsorption of hydrogen at the surface, which is the first step in the absorption/desorption process.

Pd is especially vulnerable to sulfur (H_2S) and carbon monoxide (CO) which are amoung the contaminant species present in hydrocarbon fuels used for hydrogen production,.[13] Alloying of Pd with Cu has been reported to offer significant tolerance to H_2S in the hydrogen gas stream when a PdCu membrane is operated at high temperature. At 908 K, hydrogen transport through $Pd_{47}Cu_{53}$ is not significantly inhibited by 1000 ppm H_2S.[23] On the other hand, at 623 K both Pd and $Pd_{47}Cu_{53}$ suffer greatly from H_2S poisoning. O'Brien et al.[24] studied Pd and $Pd_{47}Cu_{53}$ foils at 623 K to determine the deactivation mechanism by H_2S. Analysis of a Pd foil by X-ray diffraction (XRD) and scanning electron microscopy (SEM) reveals that Pd reacts with H_2S to form a palladium sulfide corrosion product, Pd_4S, which is about 6.6 μm thick. XPS depth profiling of a $Pd_{47}Cu_{53}$ foil reveals that sulfur penetrates only ~3 nm into the $Pd_{47}Cu_{53}$ surface. Rapid formation of a Pd–Cu–S terminal layer, which is either inactive for hydrogen dissociation

or impermeable to hydrogen atoms, is responsible for the deactivation of the $Pd_{47}Cu_{53}$ alloy membrane in H_2S at 623 K.

Electrochemical hydrogen absorption experiments have been performed on Pd in the presence of CO. Cyclic voltammetric experiments performed on Pd electrodes[25-27] have revealed that the product of CO adsorption strongly blocks hydrogen insertion as well as its removal into/from the metal. The hydrogen permeance of $Pd_{0.75}Ag_{0.25}$ membranes was measured in the presence of pure H_2 or mixtures of H_2 with CO and H_2O at temperatures in the range of 300-773 K and at atmospheric pressure by Nguyen et al.[28] Their experimental data indicated a strong inhibition by CO, due to the strong interaction between CO and Pd, however the effect was eliminated at temperatures higher than 623 K. Much of the work done on poisoning species with respect to Pd-based hydrogen permeable membranes has suggested that operating hydrogen purification at elevated temperatures can decrease the problematic effects.

1.4 Hydrogen Storage

Palladium not only acts as a catalyst for hydrogen dissociation and facilitates hydrogen uptake in other metal hydrides, it can also protect the surface from corrosion, allowing for the study of air-sensitive samples in ambient conditions.[29] Below ~250 K, absorption and desorption is effectively hindered and the hydrogen concentration is frozen in the sample. This allows for absorption of a desired hydrogen concentration at room temperature, followed by rapid cooling to cryogenic temperatures for analysis of the sample. A capping layer of 2-5 nm is usually sufficient for this purpose.[29] Yamada et al.[30] examined Mg–Ni alloys capped with Pd. The Pd film acted as a catalyst to take up hydrogen gas as well as protection of the Mg–Ni layer from oxidation.

Although hydrogenation is most commonly carried out in a high-pressure hydrogen atmosphere at elevated temperature, metals such as Pd and its alloys can be charged with hydrogen electrochemically at ambient temperature.[31] By contrast, magnesium and its alloys cannot be electrochemically charged with hydrogen as they dissolve in acidic solution and form magnesium hydroxide in alkaline media.[32] However, Mg can be electrochemically hydrogenated when Pd covers its surface. Vermeulen et al.[33] have shown that a thin (~120 nm), magnetron-sputtered film of Mg_xTi_{1-x} capped with a thin (3-4 nm) layer of Pd can be electrochemically charged with hydrogen. The hydrogen storage capacity of this material amounts up to 1750 mAh/g, corresponding to 6.4 wt%.

Many types of hydrogen storage materials have been studied, and it is thought that inexpensive, lightweight, and high capacity metal hydrides, such as MgH_2 (7.6 wt%), are the best candidates for practical applications.[34-36] There are two major problems with MgH_2: (i) the sorption kinetics involved are quite sluggish; and (ii) MgH_2 has a high thermodynamic stability requiring temperatures higher than 300 °C for the desorption of hydrogen.[34,37,38] Electrochemical loading of MgH_2 is also problematic due to corrosion and degradation in both alkaline and acidic electrolytes and subsequent loss of hydrogen capacity, but can be solved with a Pd capping layer.[37,39,40]

Even though many metals absorb hydrogen exothermally, it is necessary to overcome a certain activation energy barrier in order to dissociate the hydrogen molecule.[29] The height of the activation energy barrier depends on the surface elements. The activation energy of absorption corresponds to the activation barrier for the dissociation of the H_2 molecule and the formation of hydrogen atoms. Since many metals have slow hydrogenation kinetics, Pd can be used as a catalyst to dissociate the hydrogen molecule, facilitating the hydrogen uptake. The activation

energies of H_2 sorption for bulk MgH_2, mechanically milled MgH_2 and nanocatalyst-doped MgH_2 have been studied.[6] It was found that the activation barrier was drastically lowered by nanocatalyst doping. Similarly, Zaluska et al.[41] discovered that it takes pure Mg approximately 3 times longer to obtain the same hydrogen capacity as Pd-doped Mg. Tang et al.[38] examined Pd/Mg/Pd nanoblades for hydrogen storage and found that the effect of Pd catalyst on reducing the hydrogen desorption temperature is significantly strong.

Pozzo and Alfè[34] performed a systematic DFT/PBE study of hydrogen dissociation and subsequent diffusion over Mg surfaces doped with different transition metals. The dopants investigated were Ti, Zr, V, Fe, Ru, Co, Rh, Ni, Pd, Cu and Ag. They found that the transition metals on the left of the periodic table (Ti, V, Zr), together with Ru, eliminate the dissociation barrier altogether, however, the hydrogen atoms stick too strongly to the metal dopant, therefore hindering migration from the catalytic site. This would result in a quick deactivation of the catalyst and a slow absorption process. The transition metals on the right of the periodic table do not bind too strongly to the H atoms, allowing easy migration to the Mg surface. However, their effect on the reduction of the dissociation barrier is small. Based on their results, it appears that an optimal hydrogen dissociation catalyst should have not only good dissociation abilities but also a low sticking strength of the dissociated hydrogen atoms to the metal. Pd shows a good compromise of these properties and it could be enhanced by alloying Pd with other metals.

Another class of hydrogen storage materials mentioned in Section 1.1 is carbon. Carbon offers advantages of being light-weight and inexpensive, on-board reversibility and rapid sorption kinetics. In contrast to the chemisorption in metal hydrides,[42] the phenomenon of physical adsorption is essentially accumulation of the undissociated hydrogen molecules on a surface of microporous carbon fibers or particles. This property is due to the ability of carbon to

be prepared in a very fine powdered or fiber form with highly porous structure and due to specific interactions between carbon atoms and gas molecules. Activated carbon is well known as one of the best adsorbents for gases.[43] For conventional activated carbon, the hydrogen uptake is proportional to its surface area and pore volume, and a high hydrogen adsorption capacity (3 ~ 8 wt%) can be only obtained at very low cryogenic temperatures or very high pressures.[44] Operating at cryogenic temperatures poses certain challenges such as maintaining the storage vessel at low temperatures. This requires use of vacuum super-insulation and tank design features to minimize conduction paths to the ambient.[45] Storing hydrogen on carbon materials at practical temperatures relies on a chemical reaction between the carbon and hydrogen atoms (as opposed to physical adsorption of hydrogen molecules, which occurs at cryogenic temperatures). This requires breaking of the hydrogen-hydrogen bond in the H_2 molecule, which can be accomplished by transition metal catalysts.[46]

Metal doping of carbon materials results in the following phenomena, collectively termed as the hydrogen spillover mechanism: (1) H_2 molecules dissociate on the metal catalyst particles; (2) H atoms migrate from the metal catalyst particles to the carbon substrate material; and (3) H atoms diffuse on the substrate by a site-hopping mechanism.[47] Hydrogen spillover from metal particles to carbon materials can be assessed in a number of ways, but perhaps the most common is simple calculation of the hydrogen capacity of the metal and the hydrogen capacity of the carbon material at a given H_2 pressure. When spillover occurs, the hydrogen capacity of the combined system (carbon + metal) will typically exceed that of the individual components. An advantage to using Pd as the catalyst is that some hydrogen is stored in the catalyst itself as PdH_x, so the capacity of the overall material should be higher than that of a non-absorbing metal.

1.5 Fuel Cell Catalysis

As mentioned in Section 1.1, Pt is the most commonly used electrocatalyst in low temperature fuel cells.[14] The cost of Pt and the limited world supply are barriers to the widespread use of these types of fuel cells. Also, Pt suffers CO poisoning if carbon monoxide is present in the H_2 feed stream or is produced as an intermediate in the oxidation of small organic molecules.[48] Lastly, although Pt has the highest activity among pure metals towards the cathodic oxygen reduction reaction, it alone is still not satisfactory for this sluggish reaction. Numerous studies have been conducted to find alternative catalyst materials that can replace Pt partly or completely. Pt-based alloys such as Pt-Ru[49] and Pt-Pb[50] are not only less expensive; they exhibit enhanced oxidative activity relative to Pt. Although Pd is of great interest in a substitute material for Pt, either partially or completely, Pd alone does not seem to be active enough for use as the catalyst for most oxidation or reduction reactions. Therefore, alloys and composites of Pd have been widely explored for these purposes.

In acidic medium, Pd alone has poor activity for the hydrogen oxidation reaction (HOR), but the addition of very low amounts of Pt (5-10 at%) to Pd achieves HOR activity comparable to pure Pt.[14] Carbon-supported Pd performed poorly compared to Pt, but all of the Pd-Pt bimetallic catalysts had activity similar to Pt. Although Pd possesses very low CO tolerance, inferior to that of pure Pt, tests in PEMFCs fuelled with H_2 + CO revealed that the presence of Pd increases the tolerance of Pt and Pt-Ru catalysts. For direct methanol fuel cells, Pd is completely inactive for electrooxidation of methanol in acid solutions.[51] Pd-Pt catalysts have been found to outperform Pt through a synergistic effect since the activity of the alloys is higher than the weighted activity of the two metals.[14] On Pt electrodes, strongly bound species, such as $(COH)_{ads}$ require three neighbouring Pt sites to be adsorbed. The alloying of Pt with Pd results in

diluting Pt sites, which prevents the presence of the three adjacent sites necessary for the formation of the strongly bound intermediates.

Direct formic acid fuel cells are an alternative class of fuel cells to direct methanol fuel cells. A higher performance can be obtained using formic acid as the fuel rather than methanol because the rate of formic acid crossover through the proton exchange membrane is 5 times less than that of methanol.[52,53] Also, the optimal operating concentration of formic acid can be as high as 20 M, ten times more than methanol.[54] On Pt, the formic acid oxidation proceeds via an indirect mechanism, where CO (a poisoning intermediate) is formed. On Pd, the oxidation of formic acid proceeds through a direct mechanism, avoiding the formation of CO. This causes Pd to greatly outperform Pt in activity and stability for formic acid oxidation.

Platinum has the highest catalytic activity for oxygen reduction among pure metals. Carbon-supported Pt is the standard cathode material in low temperature fuel cells. The kinetic limitations of the oxygen reduction reaction (ORR) create cathodic overpotential losses of 0.3-0.4 V under typical operating conditions. The development of more active ORR electrocatalysts has been the subject of numerous studies. Antolini[14] wrote an excellent review on the use of palladium in fuel cell catalysis. In this review he covered the use of both Pt and Pd-based alloys for ORR. Pd-Pt alloys display ORR activity similar or slightly higher than that of pure Pt for most fuel cells, but in direct methanol fuel cells specifically they show noteworthy advantages. This is due to the tolerance of Pd to crossover methanol. Binary Pd-M, where M=Co, Ni, Se, P, Cu, Fe, Au, Mo, W or Cr and ternary Pd-Co-M, where M=Au or Mo, have been studied as low-cost alternatives to Pt and Pt-alloys. In the absence of methanol, the ORR activity decreased in the order of PdCoM > PdM ≥ Pt > Pd. In the presence of methanol, the ORR activity was similar for PdM and Pd, which were all much higher than Pt. The transition from Pt-based catalysts to

Pd-based catalysts has begun and will lead the way to develop cheaper and more active materials for the commercialization of fuel cells.

Recently, attention has been directed towards the use of hydrogen peroxide as the oxidant in fuel cells. Hydrogen peroxide is a powerful oxidizer and its reduction takes place via a two-electron transfer.[55] This has a much lower activation barrier, and thus, much faster kinetics than the four-electron reduction of oxygen.[56] It is suspected that this is due to the difference in energy required to break the single oxygen bond of H_2O_2 (146 kJ/mol) and the double oxygen bond of the O_2 molecule (494 kJ/mol).[56] Conveniently, hydrogen peroxide is a liquid, which allows hydrogen peroxide fuel cells to be used underwater or for space exploration where air is not readily available.[57] Also, the reduction at the cathode occurs at a solid/liquid interface, which is much more reliable than a solid/liquid/gas three-phase region (gas diffusion electrode).[56] For these reasons, the use of hydrogen peroxide as a fuel cell oxidant could provide a simpler route to accomplishing the commercialization of fuel cells. Several types of fuel cells using hydrogen peroxide as the oxidant have already been tested including metal semi-fuel cells (MSFCs),[57-61] direct borohydride fuel cells (DBFCs),[62-67] and direct formic acid fuel cells (DFAFCs).[68]

Compared to research on catalyst materials for oxygen reduction, studies on catalyst materials for hydrogen peroxide electroreduction are very rare. Catalysts which have been studied for cathodic hydrogen peroxide reduction include Pd,[56] Pd-Ir,[57,59,60] Pd-Ag,[58] Cu,[69] Ag,[61,70] Au,[67,71] Pd-Ru,[55] CuO/Nafion/Pt,[72] and Prussian Blue-modified electrodes.[65,73] Of those examined for hydrogen peroxide reduction, Pd-based catalysts show the best results in terms of activity and selectivity.[66,74]

1.6 Rationale and Scope of This Thesis

The main intent of this M.Sc. thesis is to examine the properties of Pd-based nanomaterials for their applications in various hydrogen technologies. The first and most hopeful ongoing research goal is to decrease the cost of material required for a given application. Generally, Pd-based catalysts present a larger particle size than Pt-based catalysts. One target of this research is to develop new synthesis methods which lead to high surface area Pd. An increase in the surface area/volume ratio for catalysts decreases material costs.

It appears that for all hydrogen absorbing applications (purification and storage) there are two common issues which need to be addressed: hydrogen embrittlement and poisoning species. In addition, hydrogen solubility plays an important role in some applications. For hydrogen dissociation applications (hydrogen storage and catalysis), where surface interactions are of greater concern than bulk phase absorption, the adsorption strength of atomic hydrogen is the most crucial factor. All of these properties can be modified by alloying Pd with other metals. Another goal of this research is to investigate the alloying effect of Pd in order to develop efficient Pd-based nanostructured catalysts.

This thesis is composed of seven chapters. In the next chapter, the experimental methods of synthesizing Pd-based nanomaterials will be discussed as well as the methods used to analyze their structure and physical properties. Chapter 3 will present the results of a study on the electrosorption of hydrogen into Pd-Cd nanostructures. Chapter 4 will discuss the hydrogen gas absorption properties of Pd, Pd-Ag, and Pd-Cd nanostructures as well as the use of these materials as hydrogen dissociation catalysts for hydrogen spillover to activated carbon. Hydrogen peroxide reduction on carbon-supported Pd-Pt nanoparticles will be examined in Chapter 5. Chapter 6 will present the results of a study of the poisoning species, CO, on small

metal clusters including Pd, PdPt, and PdAu, using density functional theory (DFT) calculations as well as experimental electrochemical and attenuated total reflection Fourier transform infrared spectroscopy (ATR-FTIR) techniques. The final chapter, Chapter 7, will provide a summary of the results and conclusions.

References

1. K. Rajeshwar, R. McConnell, K. Harrison, S. Licht, *Solar Hydrogen Generation*, *Chapter 1: Renewable Energy and the Hydrogen Economy*, Springer Science+Business Media, LLC., New York, **2008**.

2. A.W.C. van den Berg, C.O. Areán, *Chem. Commun*. **2008**, 668.

3. A. Chen, P. Holt-Hindle, *Chem. Rev.* **2010,** *110,* 3767.

4. R.K. Shah, *Recent Trends in Fuel Cell Science and Technology*, *Chapter 1: Introduction to Fuel Cells*, Anamaya Publishers, New Delhi, **2007**.

5. L. Wang, R.T. Yang, *Energy Environ. Sci*. **2008**, 1, 268.

6. M.U. Niemann, S.S. Srinivasan, A.R. Phani, A. Kumar, D.Y. Goswami, E.K. Stefanakos, *J. Nanomater*. **2008**, *950967*, 1.

7. L. Schlapbach, *Nature*, **2009**, *460*, 809.

8. T. Graham, *Philo*s. *Trans*. *R. Soc*. **1866**, *156*, 415.

9. A. Michael, *Chim*. *Ind*. **1939**, *41*, 632.

10. D.G. Narehood, S. Kishore, H. Goto, J.H. Adair, J.A. Nelson, H.R. Gutiérrez, P.C. Eklund, *Int. J. Hydrogen Energ*. **2009**, *34*, 952.

11. V. Ledentu, W. Dong, P. Sautet, *Surf. Sci*. **1998**, *412/413*, 518.

12. R.K. Joshi, S. Krishnan, M. Yoshimura, A. Kumar, *Nanoscale Res. Lett*. **2009**, *4*, 1191.

13. A. Damle, *Hydrogen Fuel: Production, Transportation, and Storage*, *Chapter 8: Hydrogen separation and purification*, CRC Press, Taylor & Francis Group, Boca Raton, **2009**.

14. L. Schlapbach, A. Züttel, *Nature*, **2001**, *414*, 353.

15. E. Antolini, *Energy Environ. Sci*. **2009**, *2*, 915.

16. A.L. Mejdell, M. Jondahl, T.A. Peters, R. Bredesen, H.J. Venvik, *Sep. Purif. Technol*. **2009**, *68*, 178.

17. H. Li, H. Xu, W. Li, *J. Membrane Sci*. **2008**, *324*, 44.

18. M. Yamauchi, H. Kobayashi, H. Kitagawa, *ChemPhysChem* **2009**, *10*, 2566.

19. A.K.M. Fazle, Y. Sakamoto, *Int. J. Hydrogen Energ*. **2000**, *25*, 853.

20. Y. Sun, Z. Tao, J. Chen, T. Herricks, Y. Xia, *J. Am. Chem. Soc*. **2004**, *126*, 5940.

21. E.L. Foletto, J.V.W. Da Silveira, S.L. Jahn, *Lat. Am. Appl. Res*. **2008**, *38*, 79.

22. J.-N. Han, S.-I. Pyun, T.-H. Yang, *J. Electrochem. Soc.,* **1997***,* 144, 4266.

23. B.D. Morreale, M.V. Ciocco, B.H. Howard, R.P. Killmeyer, A.V. Cugini, R.M. Enick, *J. Membr. Sci.* **2004**, *241*, 219.

24. C.P. O'Brien, B.H. Howard, J.B. Miller, B.D. Morreale, A.J. Gellman, *J. Membr. Sci*. **2010**, *349*, 380.

25. A. Czerwiski, *J. Electroanal. Chem.* **1994**, *379*, 487.

26. A. Czerwiski, S. Zamponi, R. Marassi, *J. Electroanal. Chem.* **1991**, *304*, 233.

27. A. Czerwiski, G. Maruszczak, M. Zelazowska, *Polish. J. Chem.* **1993**, *67*, 2037.

28. T.H. Nguyen, S. Mori, M. Suzuki, *Chem. Eng. J*. **2009**, *155*, 55.

29. A. Remhof, A. Borgschulte, *ChemPhysChem* **2008**, *9*, 2440.

30. Y. Yamada, S. Bao, K. Tajima, M. Okada, M. Tazawa, A. Roos, K. Yoshimura, *J. Appl. Phys*. **2010**, *107*, 043517.

31. C. Gabrielli, P.P. Grand, A. Lasia, H. Perrot, *J. Electrochem. Soc.*, **2004**, *151*, A1925.

32. R. Juškėnas, V. Kapočius, P. Miečinskas, V. Karpavičienė, *J. Alloy. Compd*. **2009**, *467*, 524.

33. P. Vermeulen, R.A.H. Niessen, P.H.L. Notten, *Electrochem. Commun*. **2006**, *8*, 27.

34. M. Pozzo, D. Alfè, *Int. J. Hydrogen Energ*. **2009**, *34*, 1922.

35. H. Shao, T. Liu, Y. Wang, H. Xu, X. Li, *J. Alloy. Comp*. **2008**, *465*, 527.

36. A.F. Gross, C.C. Ahn, S.L. Van Atta, P. Liu, J.J. Vajo, *Nanotechnology,* **2009**, *20*, 204005.

37. O. Friedrichs, L. Kolodziejczyk, J.C. Sánchez-López, A. Fernández, L. Lyubenova, D. Zander, U. Köster, K.F. Aguey-Zinsou, T. Klassen, R. Bormann, *J. Alloy Comp*. **2008**, *463*, 539.

38. F. Tang, T. Parker, H.-F. Li, G.-C. Wang, T.-M. Lu, *Nanotechnology* **2008**, *19*, 465706.

39. T. Ma, Y. Hatano, T. Abe, K. Watanabe, *J. Alloy. Comp*. **2005**, *391*, 313.

40. X. Xiao, L. Chen, Z. Hang, X. Wang, S. Li, C. Chen, Y. Lei, Q. Wang, *Electrochem. Commun*. **2009**, *11*, 515.

41. A. Zaluska, L. Zaluski, J.O. Ström-Olsen*, J. Alloy. Compd*. **1999**, *288*, 217.

42. C.I. Contescu, C.M. Brown, Y. Liu, V.V. Bhat, N.C. Gallego *J. Phys. Chem. C* **2009**, *113,* 5886.

43. A.D. Lueking, R.T. Yang, *Appl. Catal A-Gen*. **2004**, *265*, 259.

44. H. Wang, Q. Gao, J. Hu, *J. Am. Chem. Soc*. **2009**, *131*, 7016.

45. R.K. Ahluwalia, J.K. Peng, *Int. J. Hydrogen Energ*. **2009**, *34*, 5476.

46. C.-S. Tsao, Y.-R. Tzeng, M.-S. Yu, C.-Y. Wang, H.-H. Tseng, T.-Y. Chung, H.-C. Wu, T. Yamamoto, K. Kaneko, S.-H. Chen, *J. Phys. Chem. Lett*. **2010**, *1*, 1060.

47. L. Chen, A.C. Cooper, G.P. Pez, H. Cheng, *J. Phys. Chem. C* **2007**, *111*, 18995.

48. X. Li, I.-M. Hsing, *Electrochim. Acta* **2006**, *51*, 3477.

49. E.V. Spinacé, A.O. Neto, M. Linardi, *J. Power Sources* **2004**, 129, 121.

50. J. Wang, R.M. Asmussen, B. Adams, D.F. Thomas, A. Chen, *Chem. Mater.*, **2009**, *21*, 1716.

51. A. Capon, R. Parsons, *J. Electroanal. Chem*. **1973**, *44*, 239.

52. X. Wang, J.M. Hu, I.M. Hsing, *J. Electroanal. Chem*., **2004**, *562*, 73.

53. S. Ha, B. Adams, R.I. Masel, *J. Power Sources* **2004**, *128*, 119.

54. Y.W. Rhee, S. Ha, C. Rice, R.I. Masel, *J. Power Sources* **2003**, *117*, 35.

55. L. Sun, D. Cao, G. Wang, *J. Appl. Electrochem*. **2008**, *38*, 1415.

56. D. Cao, L. Sun, G. Wang, Y. Lv, M. Zhang, *J. Electroanal. Chem*. **2008**, *621*, 31.

57. M.G. Medeiros, R.R. Bessette, C.M. Deschenes, C.J. Patrissi, L.G. Carreiro, S.P. Tucker, D.W. Atwater, *J. Power Sources* **2004**, *136*, 226.

58. W. Yang, S. Yang, W. Sun, G. Sun, Q. Xin, *Electrochim. Acta* **2006**, *52*, 9.

59. R.R. Bessette, J.M. Cichon, D.W. Dischert, E.G. Dow, *J. Power Sources* **1999**, *80*, 248.

60. R.R. Bessette, M.G. Medeiros, C.J. Patrissi, C.M. Deschenes, N.N. LaFratta, *J. Power Sources* **2001**, *96*, 240.

61. W. Yang, S. Yang, W. Sun, G. Sun, Q. Xin, *J. Power Sources* **2006**, *160*, 1420.

62. C. Ponce de León, F.C. Walsh, A. Rose, J.B. Lakeman, D.J. Browning, R.W. Reeve, *J. Power Sources* **2007**, *164*, 441.

63. N.A. Choudhury, R.K. Raman, S. Sampath, A.K. Shukla, *J. Power Sources* **2005**, *143*, 1.

64. N. Luo, G.H. Miley, K.-J. Kim, R. Burton, X. Huang, *J. Power Sources* **2008**, *185*, 685.

65. G. Selvarani, S.K. Prashant, A.K. Sahu, P. Sridhar, S. Pitchumani, A.K. Shukla, *J. Power Sources* **2008**, *178*, 86.

66. J. Ma, Y. Sahai, R.G. Buchheit, *J. Power Sources* **2010**, *195*, 4709.

67. R.K. Raman, S.K. Prashant, A.K. Shukla, *J. Power Sources* **2006**, *162*, 1073.

68. E. Kjeang, A.G. Brolo, D.A. Harrington, N. Djilali, D. Sinton, *J. Electrochem. Soc*. **2007**, *154*, B1220.

69. K.L. Stewart, A.A. Gewirth, *Langmuir* **2007**, *23*, 9911.

70. K. Doblhofer, G. Flätgen, S. Horswell, B. Pettinger, S. Wasle, K.G. Weil, *Surf. Sci*. **2009**, *603*, 1900.

71. R. Zeis, T. Lei, K. Sieradzki, J. Snyder, J. Erlebacher, *J. Catal.* **2008**, *253*, 132.

72. X.-M. Miao, R. Yuan, Y.-Q. Chai, Y.-T. Shi, Y.-Y. Yuan, *J. Electroanal. Chem*. **2008**, *612*, 157.

73. R. Araminaitė, R. Garjonytė, A. Malinauskas, *J. Solid State Electrochem*. **2010**, *14*, 149.

74. L. Gu, N. Luo, G.H. Miley, *J. Power Sources* **2007**, *173*, 77.

Chapter 2

Experimental Methods

2.1 Introduction

In the previous chapter, the significant roles of Pd for various hydrogen involving technologies and the underlying challenges for its commercial applications were discussed. Also, the objectives for this thesis research were outlined. In this chapter, the main experimental methodology and techniques used in this M.Sc. project will be briefly introduced. For clarification, some details on the experimental procedures and equipment, pertaining to each specific study, will be presented in Chapters 3 – 6.

2.2 Chemicals and Materials

The following chemicals were used as received from Sigma-Aldrich: sulfuric acid (99.999%); perchloric acid (70%); hydrochloric acid (37.5%); nitric acid ($\geq$69%); ammonium formate (99.995%); ethylene glycol ($\geq$99%); hydrogen peroxide (30%); sodium borohydride ($\geq$98%); AgNO$_3$ ($\geq$99.0%); Pd(NO$_3$)$_2$·2H$_2$O; and Nafion$^{®}$ perfluorinated ion-exchange resin (10 wt. % dispersion in water).

The following chemicals and materials were used as received from Alfa-Aesar: titanium wire (99.7%, 2 mm diameter); titanium strip (99.2%, 1.25 cm x 0.5 mm); Pt wire (99.9%, 0.5 mm diameter); HAuCl$_4$·xH$_2$O (99.9%); H$_2$PtCl$_6$·6H$_2$O (99.9%); PdCl$_2$ (99.9%); and Cd(NO$_3$)$_2$·4H$_2$O (99.9%).

The following gases were used throughout this thesis research: argon (PRAXAIR, UHP, 99.999%); nitrogen (PRAXAIR, UHP, 99.999%); hydrogen (BOC Gases, UHP, 99.999%); and carbon monoxide (PRAXAIR, Grade 2.5, 99.5%).

Two carbon materials were obtained as support materials for nanoparticles. The carbon black powder used to support PdPt catalysts for hydrogen peroxide reduction was Vulcan XC72R from Cabot Corp. The activated carbon powder used in the hydrogen gas adsorption studies was Norit PAC 200 (M-1620) from Norit Americas Inc.

Pure water (18 MΩcm) obtained from a NANOpure® Diamond[TM] UV ultrapure water purification system was used for cleaning purposes and preparation of all solutions and electrolytes.

2.3 Fabrication of Nanomaterials

2.3.1 Ti-supported Nanostructures

The nanostructures used as electrodes in the hydrogen electrosorption studies (Chapter 3) and CO adsorption studies (Chapter 6), were directly grown onto Ti plates using a facile hydrothermal reduction method, described previously.[1,2] The Ti substrate plates (1.25cm x 0.80cm x 0.5mm) were first degreased in an ultrasonic bath of acetone for 10 minutes followed by 10 minutes in pure water. The substrates were then etched in 18% HCl at approximately 85 °C for 30 minutes. The etched Ti substrates were transferred into Teflon-lined autoclaves along with 10 mL of an aqueous mixture containing 5 mM inorganic metal precursor and 1 M reducing agent. In the case of PdX bimetallic nanostructures, varying amounts of the X precursor were added to obtain the desired ratio of Pd:X. The autoclaves were sealed and heated at 180 °C for 2 hours in an oven which had been preheated. After 2 hours, the autoclaves were immediately

removed from the oven and allowed to cool to room temperature for approximately 4 hours. The Ti plates coated with the nanostructures were then removed from the autoclaves, dried under argon, and then rinsed with pure water. The coated Ti plates were annealed by heating them to 250 °C at a ramp rate of 8 °C/minute and then held at 250 °C for 2 hours in a tube furnace under argon to ensure good surface adhesion of the nanostructures.

2.3.2 Carbon-supported Nanoparticles

Carbon supported nanoparticles were used for hydrogen gas adsorption studies (Chapter 4) and for hydrogen peroxide electroreduction (Chapter 5). All of the carbon-supported samples were prepared using a room temperature impregnation method. The metal precursors, water (5 mL), and the appropriate amount of carbon material were added to a beaker, such that the coating load was 5 wt% in the case of hydrogen adsorption materials (Chapter 4) and 20 wt% metal in the case of the hydrogen peroxide reduction catalysts (Chapter 5). This mixture was then sonicated for 20 minutes. Using 0.5 M NaOH, the pH was adjusted between 9.5 and 10 and the mixture was allowed to stir for 5 minutes to provide a better dispersion of metal precursors on the carbon surface. The reducing agent (0.125 M $NaBH_4$), in 10 times molar excess of the metal content, was added dropwise while constantly stirring. The reduction process was allowed to continue for 1 hour before the catalysts were centrifuged and washed with pure water until the pH remained constant. The catalysts were finally dried on a glass plate in a drying oven at 60 °C for 12 hours.

Inductively coupled plasma atomic emission spectroscopy (ICP-AES) was used to verify completion of the reduction of the metal catalysts and the final composition of the carbon

supported nanoparticles. This was accomplished by analyzing the solution after reduction with sodium borohydride to ensure no metal remained.

2.4 Surface Analysis

The surface morphology of the fabricated samples was characterized using a JEOL JSM 590LV scanning electron microscope (SEM) and/or a JEOL 2010 transmission electron microscope (TEM). Surface composition was examined by an Oxford Links ISIS energy dispersive X-ray spectrophometer (EDS), and the crystallographic properties were analyzed using X-ray diffraction (XRD) (Philips PW 1050-3710 or PAN analytical X'Pert Pro MPD).

X-ray photoelectron spectrophotometric (XPS) analysis was performed using a Thermo Scientific K-Alpha XPS spectrometer. The samples were run at a take-off angle (relative to the surface) of 90°. A monochromatic Al K_α X-ray source was used, with a spot area (on a 90° sample) of 400 μm. The position of the energy scale was adjusted to place the main C 1s feature (C-C) at 284.6 eV. XPSPEAK 4.1 software was used to analyze the raw data and to fit the spectra.

2.5 Electrochemical Experiments

For all electrochemical experiments, a three-electrode cell system and a VoltaLab PGZ402 potentiostat were used. The counter electrode used was a Pt wire coil (10 cm^2) and this was cleaned before each experiment by flame annealing and quenching with pure water. The reference electrode was either a saturated calomel electrode (SCE) or an Ag/AgCl reference electrode. The prepared nanostructured materials were used as the working electrodes in all cases. The electrolytes were prepared using pure water, $HClO_4$, H_2SO_4, and H_2O_2. The solutions

were deaerated with ultrapure argon gas prior to measurements to remove any dissolved oxygen. All experiments were performed at room temperature (22 ± 2 °C). Data acquisition and analysis were performed using VoltMaster 4 software.

2.6 Gas Sorption Studies

The N_2 and H_2 gas adsorption studies were performed using a Quantachrome Nova 2200 surface area and pore size analyzer. The samples were first degassed at 250 °C for a minimum of 12 hours under vacuum. Nitrogen adsorption/desorption was performed at liquid nitrogen temperature (77 K) and hydrogen adsorption/absorption was performed at both liquid nitrogen temperature and room temperature in a water bath. The Brunauer-Emmet-Teller (BET) surface area was then calculated from N_2 adsorption at liquid nitrogen temperature (77 K) with a multipoint method using 5 points within the relative pressure (P/P_0) range of 0.10 to 0.30. The total pore volumes were calculated from the N_2 isotherm at a relative pressure of 0.99. The micropore volumes and modal micropore diameters were obtained using the Dubinin Astakhov (DA) method of analysis. The Barret-Jayner-Halenda (BJH) method was used to determine the volume of mesopores and modal mesopore diameters using the desorption branches of the N_2 isotherms and ignoring points below a relative pressure of 0.35.

2.7 Computational Methods

Density functional theory (DFT) calculations were carried out using the Gaussian 03 software package[12] with the use of the Becke's three parameter hybrid exchange functional[13] combined with the Lee–Yang–Parr non-local correlation functional[14] (B3LYP). The double-zeta quality effective core potential basis set LANL2DZ[15] was employed for all transition metals,

while the 6-31G* basis set was used for the C and O atoms and the aug-cc-pVTZ basis set[16] was used for the H atoms.

2.8 Attenuated Total Reflection Fourier Transform Infrared Spectroscopy

All *in situ* attenuated total reflection-Fourier transform infrared spectroscopy (ATR-FTIR) experiments were performed using a Nicolet Fourier transform infrared spectrometer with a liquid N_2-cooled MCT detector. The spectro-electrochemical cell consisted of a Teflon chamber with a ZnSe hemisphere window sealed on the bottom. The synthesized nanoparticles were suspended in pure water with the aid of ultrasonic treatment and then coated onto the ZnSe window. The incidence angle of the IR beam was controlled with a variable angle home-made accessory and was set to 60º for all experiments. The spectra were recorded using a single potential step procedure in which the electrode potential was controlled by a potentiostat and increased in steps of +0.10 V. All interferograms were acquired at 4 cm^{-1} resolution, and 400 scans were added and averaged. The interferograms were shown in terms of relative change of the electrode reflectivity, which is defined as $\Delta R/R = (R(E_2)-R(E_1)) / R(E_1)$, where $R(E_1)$ and $R(E_2)$ are the thin films' reflectivity at potentials E_1 and E_2, respectively. The spectra recorded at $E_1 = -0.20$ V were used as reference.

2.9 Summary

This chapter presented the materials used in the research throughout this thesis. The experimental methods and equipment used for synthesizing and characterizing Pd-based nanomaterials were discussed in detail. The following chapter will present a study of PdCd nanostructures for hydrogen electrosorption.

References

1. B.D. Adams, G. Wu, S. Nigro, A. Chen, *J. Am. Chem. Soc*. **2009**, *131*, 6930.

2. B.D. Adams, C.K. Ostrom, A. Chen, *Langmuir*, **2010**, *26,* 7632.

3. M.J. Frisch, G.W. Trucks, H.B. Schlegel, G.E. Scuseria, M.A. Robb, J.R. Cheeseman, J.A. Montgomery Jr., T. Vreven, K.N. Kudin, J.C. Burant, J.M. Millam, S.S. Iyengar, J. Tomasi, V. Barone, B. Mennucci, M. Cossi, G. Scalmani, N. Rega, G.A. Petersson, H. Nakatsuji, M. Hada, M. Ehara, K. Toyota, R. Fukuda, J. Hasegawa, M. Ishida, T. Nakajima, Y. Honda, O. Kitao, H. Nakai, M. Klene, X. Li, J.E. Knox, H.P. Hratchian, J.B. Cross, V. Bakken, C. Adamo, J. Jaramillo, R. Gomperts, R.E. Stratmann, O. Yazyev, A.J. Austin, R. Cammi, C. Pomelli, J.W. Ochterski, P.Y. Ayala, K. Morokuma, G.A. Voth, P. Salvador, J.J. Dannenberg, V.G. Zakrzewski, S. Dapprich, A.D. Daniels, M.C. Strain, O. Farkas, D.K. Malick, A.D. Rabuck, K. Raghavachari, J.B. Foresman, J.V. Ortiz, Q. Cui, A.G. Baboul, S. Clifford, J. Cioslowski, B.B. Stefanov, G. Liu, A. Liashenko, P. Piskorz, I. Komaromi, R.L. Martin, D.J. Fox, T. Keith, M.A. Al-Laham, C.Y. Peng, A. Nanayakkara, M. Challacombe, P.M.W. Gill, B. Johnson, W. Chen, M.W. Wong, C. Gonzalez, J.A. Pople, *Gaussian 03*, revision D.01, Gaussian, Inc., Wallingford, CT, **2004**.

4. A.D. Becke, *J. Chem. Phys.* **1993**, *98*, 5648.

5. C. Lee, W. Yang, R.G. Parr, *Phys. Rev. B* **1988**, *37*, 785.

6. P.J. Hay, W.R. Wadt, *J. Chem. Phys*. **1985**, *82*, 270.

7. R.A. Kendall, T.H. Dunning Jr., R.J. Harrison, *J. Chem. Phys.* **1992**, *96*, 6796.

Chapter 3

Hydrogen Electrosorption into PdCd Nanostructures[*]

3.1 Introduction

The shape-controlled synthesis of metal nanostructures has attracted considerable interest because their properties and applications are influenced greatly by their morphologies. A variety of fabrication methods have been used to produce nanostructures with different shapes.[1-3] Palladium is a metal which can absorb a large volumetric quantity of hydrogen and has been studied extensively in the past for this attractive property in both the gas phase[4-6] and under electrochemical conditions[7-10] because it allows a simplistic model in comparison to those of complex alloys.[11-13] On the other hand, Pd-based alloys offer a class of attractive materials for studying metal hydrides because of higher solubility and permeability of hydrogen than pure Pd.[14]

Extremely large currents generated from the electrochemical absorption and desorption of hydrogen in bulk Pd (wires or foils) can be avoided by using so-called „limited volume electrodes" (LVEs).[15-20] These LVEs consist of a thin layer of Pd or Pd-alloy deposited onto a matrix, such as gold, which does not absorb hydrogen. LVEs allow for the control of the amount of absorbed hydrogen in the thin layer. Pd[7,8,10,16,21] and various Pd-alloys have been studied this way, including PdPt,[17] PdRh,[19,20] PdNi,[15] PdP,[17] and PdAu.[22] All of the Pd-based materials studied using this technique were prepared using electrodeposition.

In the past, it has been found that nanostructured Pd can store more hydrogen than bulk Pd metal due to trapping of hydrogen in grain boundaries.[8,14,23] This also gives better resistance

---

[*] This chapter has been published as two separate articles (References 25 and 26).

to hydrogen embrittlement.[24] In this chapter, the properties of PdCd nanostructures for hydrogen electrosorption will be explored by applying the LVE technique. The inexpensive price of Cd makes it an attractive material to combine with Pd, and by incorporating the larger Cd atoms into the Pd crystal lattice, the lattice expansion due to hydrogen absorption can be effectively controlled and tuned. Cadmium is a relatively abundant element. It is used in batteries, cadmium pigments, coatings, and plating alloys as stabilizers for plastics although it is a potential environmental hazard. The nanostructured PdCd alloys with compositions ranging from 0 to 20 at.% Cd were directly grown onto Ti substrates using a hydrothermal reduction method. The effects of sweep rate, potential, and composition of Cd on hydrogen adsorption have been systemically studied. This study has shown that the α to β phase transition is the slowest step in the hydrogen absorption process, which can be practically eliminated when optimum amount of Cd atoms is doped. This chapter is a combination of the results which have been published as two separate articles.[25,26]

3.2 Experimental Section

The PdCd nanostructures were directly grown onto Ti plates using the hydrothermal reduction method described in Chapter 2. Ammonium formate was as used as the reducing agent and the metal precursors were $PdCl_2$ and $Cd(NO_3)_2 \cdot 4H_2O$. Stoichiometric amounts of the $Cd(NO_3)_2 \cdot 4H_2O$ precursor were added to obtain the desired ratio of Pd:Cd. Table 3.1 displays ICP-AES results for the amount of precursors remaining in solution (i.e., not reduced) after the hydrothermal reductions.

The surface morphology of the fabricated samples was characterized using a JEOL JSM 590LV SEM. Surface composition was investigated by an Oxford Links ISIS energy dispersive X-ray spectrometer as well as XPS for the PdCd(10%) sample. The normalized atomic surface

compositions based on quantitative EDS analysis are reported as an average value from readings taken at various spots on each sample surface. It was found throughout the experiments that the surface composition based on EDS analysis was consistent with the stoichiometric composition of metal precursors added to the hydrothermal vessels prior to reduction and the ICP-AES results. The XRD patterns of the as-prepared samples were recorded using a Philips PW 1050-3710 Diffractometer with Cu Kα radiation.

Table 3.1. ICP-AES results of the concentrations of Pd and Cd remaining in solution after the hydrothermal reductions. Initial concentrations were calculated based on the amount of $PdCl_2$ and $Cd(NO_3)_2$ added to hydrothermal vessels.

Molar Ratio Pd:Cd	Initial [Pd] (ppm)	Initial [Cd] (ppm)	Final [Pd] (ppm)	Final [Cd] (ppm)
100:0	532.10	0.00	0.006	0.000
98.5:1.5	532.10	8.56	0.000	0.005
97:3	532.10	17.38	0.003	0.006
95:5	532.10	29.58	0.002	0.006
90:10	532.10	62.45	0.002	0.008
85:15	532.10	99.19	0.008	0.008
80:20	532.10	140.51	0.045	0.040

For the hydrogen electrosorption measurements, the cell setup was described in Chapter 2. The reference electrode was a SCE connected to the cell through a salt bridge. All potentials mentioned herein are with respect to the SCE reference electrode. The working electrodes used were the prepared Ti/PdCd plates (1 cm^2). The coating loads of the electrodes, for calculating the H/PdCd ratios, were determined by weighing the Ti plates before and after being coated with the PdCd nanostructures with a mass balance accurate to 0.01 mg. It was found that all of the electrodes fabricated and studied had similar coating loads between 0.90 mg and 1.10 mg. The electrolyte for these studies was 0.1 M $HClO_4$, and the solution was deaerated with ultrapure argon gas prior to measurements to remove any dissolved oxygen, and argon gas was continuously bubbled into the solution during the experiments to increase mass transport.

Hydrogen absorption was performed at a constant potential for 10 minutes, which was sufficient to ensure full hydrogen saturation. A scan rate of 20 mV/s was used for the cyclic voltammetry as this was found to be appropriate to desorb the full amount of hydrogen. The amount of absorbed hydrogen was calculated from the hydrogen oxidation charge, Q_H, obtained by the integration of voltammetric curves recorded during hydrogen desorption and the mass of the PdCd film, and is reported as the H/(Pd+Cd) atomic ratio according to the following equations:

$$\frac{H}{Pd+Cd} = \frac{n_H}{(n_{Pd}+n_{Cd})} \tag{3.1}$$

$$n_H = \frac{Q_H}{F} \tag{3.2}$$

$$(n_{Pd} + n_{Cd}) = \frac{m_{Pd_xCd_y}}{xM_{Pd}+yM_{Cd}} \tag{3.3}$$

In these equations, n_H, n_{Pd}, and n_{Cd} are the number of moles of hydrogen, palladium, and cadmium, respectively, F is Faraday"s constant (96485.34 C/mol), m_{PdxCdy} is the mass of the PdCd film, and M_{Pd} and M_{Cd} are the molecular weights of Pd and Cd, respectively.

3.3 Surface Analysis of the Electrodes

Typical SEM images of the formed Pd-Cd nanostructures are displayed in Figure 3.1, showing that the addition of Cd drastically changes the morphology. Pure Pd (Figure 3.1a) exhibits nanoporous morphology with randomized small particles. The addition of small amounts of Cd (as little as 1.5%) triggers the formation of dendrites. The formed dendrites decrease in size with increasing amounts of Cd from 1.5% (Figure 3.1b) to 15.0% (Figure 3.1e). The morphology of the Pd-Cd materials with 10% Cd tends to be very similar to that of those with a composition of 15%. Further increasing the Cd content to 20%, causes the formation of large particles ranging in size from 50 nm to 1 μm (Figure 3.1f).
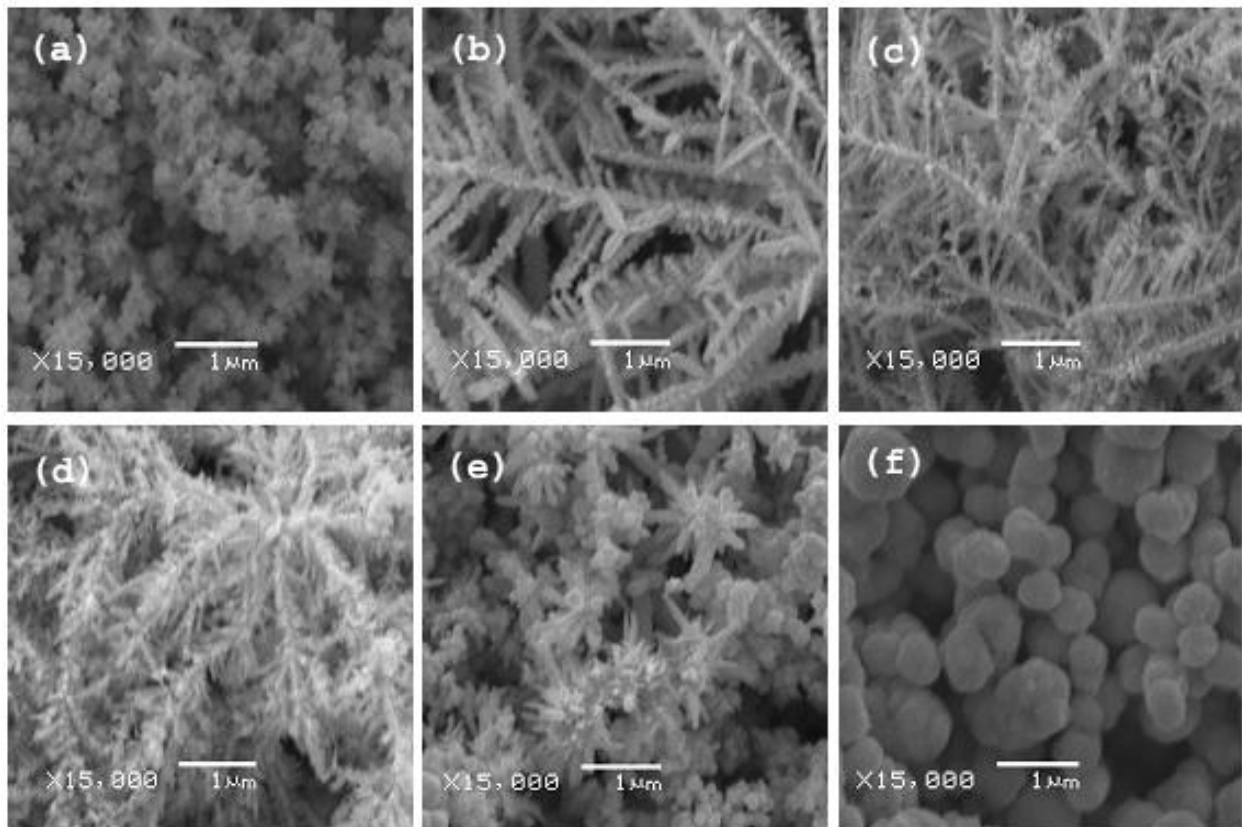
Figure 1. SEM images at 15000x magnification of the Pd-Cd surfaces with normalized atomic ratios of Pd:Cd of 100:0 (a); 98.5:1.5 (b); 97:3 (c); 95:5 (d); 85:15 (e); and 80:20 (f).

Based on computational modeling,[27-31] it is believed that dendritic growth reflects a competition between order associated with the symmetries of the crystal structure and morphological instabilities arising from the nonlinear diffusion process.[30] Simulations of the morphology of a diffusion-limited aggregate show that a change in the random noise level can vary the morphology from an ordered anisotropic shape into an irregularly branching pattern.[27] In the present work, 100% Pd species, when reduced, did not produce dendritic morphology, while the presence of small amounts of Cd massively triggers dendritic growth. The Cd atoms at the low percentages (e.g., 1.5%, 3% and 5%) can be treated as "foreign impurities" with respect to the Pd matrix. This could correspond to the aforementioned "instabilities" in crystal growth and "random noise" in computer simulations, both of which are essential for inducing the dendritic growth. In the case of our hydrothermal process, the reducing agent ammonium formate is always present in large excess compared to the metal precursors. This ensures the co-reduction of both metal cations and produces sufficiently fast reaction kinetics to cause supersaturation during the crystal nucleation phase. In the subsequent crystal growth phase, diffusion of the reduced Pd and Cd is the dominant driving force responsible for the dendritic growth. When a small amount of Cd is introduced, the reduced Cd species serve as "pinning centers" and interfere with the growth front of the main trunks. Since the interfering Cd atoms have the possibility of occupying certain crystal lattice points during the diffusion process, and the anisotropic growth of Pd atoms along the preferred crystal lattice is kinetically fast enough to engulf the Cd atoms and further accommodate these foreign atoms inside the crystal lattice, the formed intermetallic nanocrystals are consistent in composition with the original aqueous mixture of the precursors. This is further supported by our EDS analysis and ICP-AES results (Table 3.1).

X-ray diffraction was used to identify the internal crystalline structures of the prepared Pd-Cd nanomaterials. As seen in Figure 3.2, the XRD patterns show that all of the peaks, except those arising from the Ti substrates, can be referenced to a face-centered cubic (fcc) unit cell. For pure Pd, the 2θ values of 40.02°, 46.56°, 68.04°, and 82.05°, can be indexed to the diffraction of (111), (200), (220) and (311) planes of Pd, respectively (JCPDS file no. 46-1043). As more Cd is added, all the peaks are shifted slightly to smaller 2θ values, indicative of increased d-spacing and a dilation of the lattice constant, due to the incorporation of increasing amounts of the larger Cd atoms into the Pd fcc lattice. No hexagonal Cd peaks appear, indicating that alloyed Pd-Cd intermetallic nanostructures were formed.

The lattice constants were calculated from the (220) peak using the equation:[32]

$$a = \frac{\sqrt{2}\lambda}{\sin\theta} \tag{3.4}$$

In this equation, a is the lattice constant, λ is the wavelength of X-ray radiation (Cu Kα = 0.15405 nm), and θ is the location of the (220) peak in radians. Pure Pd had a lattice constant of 0.389 nm while the Pd-Cd(20%) had a lattice constant of 0.396 nm. A plot of the lattice constant vs. the normalized atomic composition of Cd in the film (Vegard"s plot) is shown in Figure 3.3. The dependence of the lattice constant on the composition obeys Vegard"s law which is common for many binary intermetallic compounds. It is generally assumed that hydrogen diffuses into a perfect palladium crystal by jumping from one octaedric site to another.[7] Due to the dilation of the lattice constant by the addition of Cd, the diffusion of hydrogen is expected to increase.[33]

It is known that properties of nanomaterials depend on the size of their crystallites.[8,28,34,35] Small crystallite size increases the number of grain boundaries in which hydrogen can be stored.[8,14,28] The average crystallite size of the Pd-Cd nanostructured alloys were calculated from
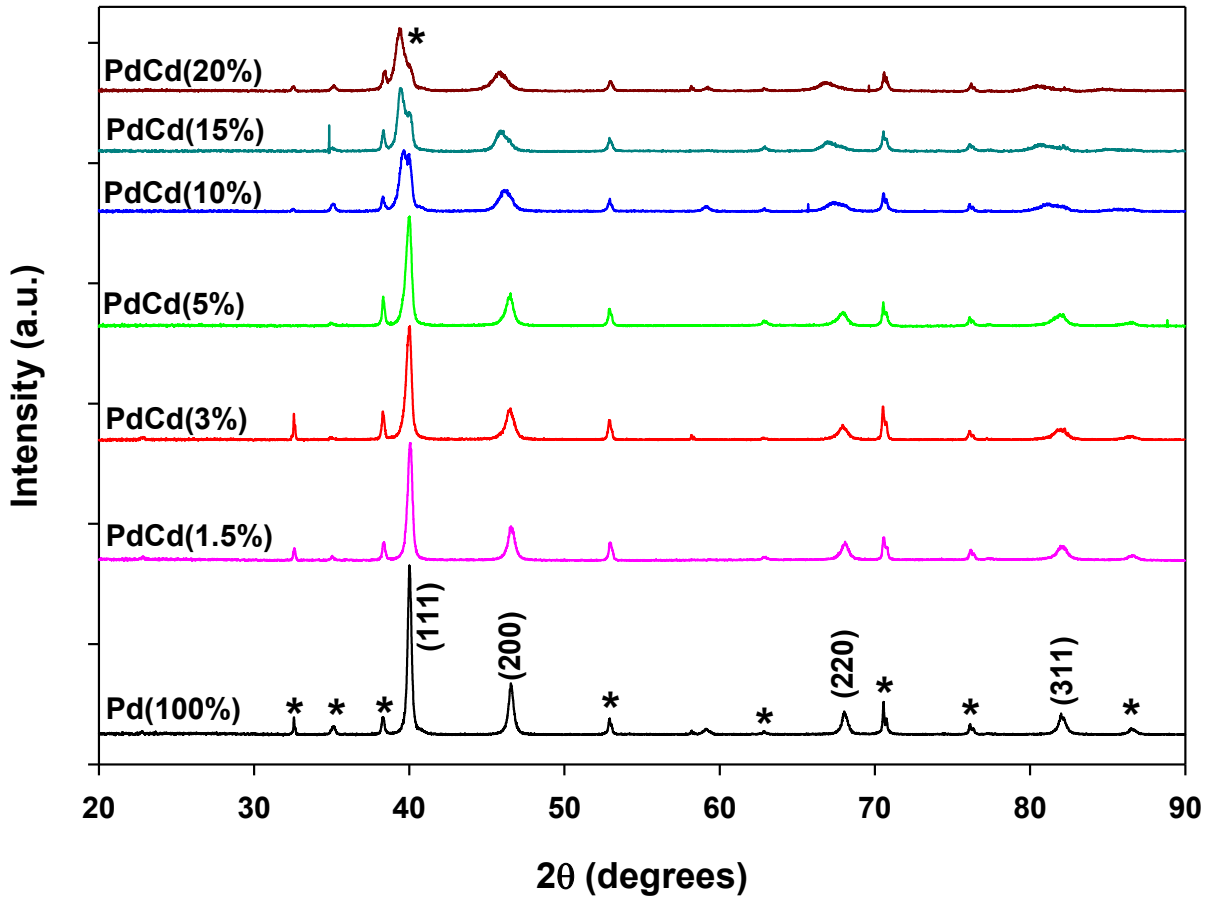
Figure 3.2. XRD patterns of the prepared PdCd films. Diffraction peaks belonging to the Ti substrate are labelled with (*).
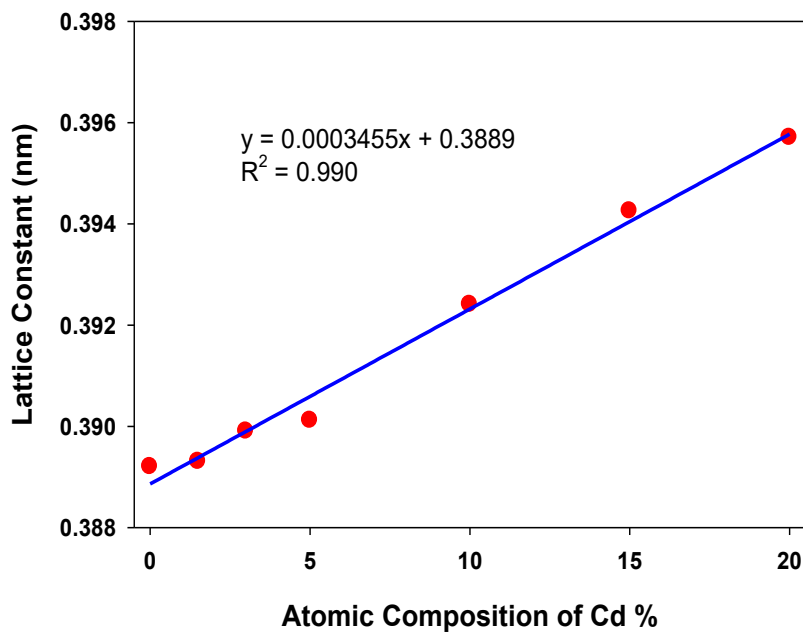
Figure 3.3. Vegard's plot showing the dependence of the fcc lattice constant on the normalized atomic composition of Cd.
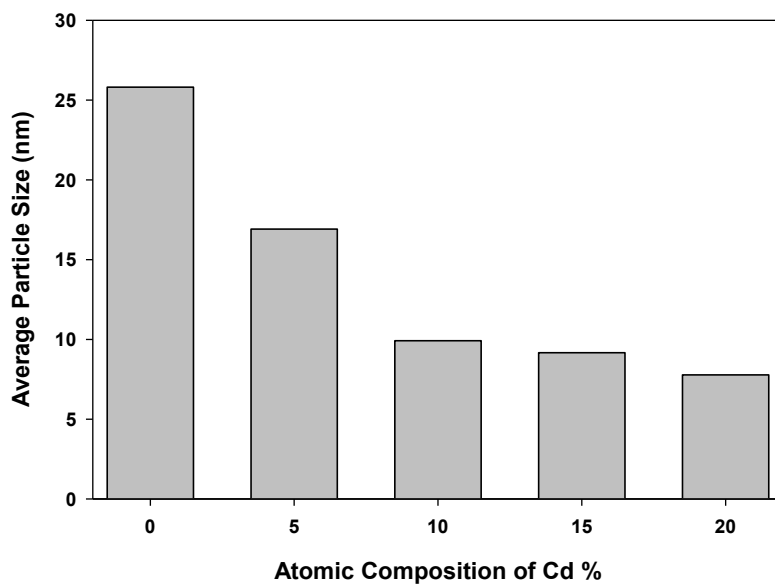

Figure 3.4. The average particle size of the PdCd nanostructures vs. the atomic composition of Cd as calculated from equation 2.

37

the (200) peak (Figure 2) using the Scherrer equation:[36]

$$L = \frac{0.94\lambda}{\beta \cos\theta} \qquad\qquad (3.5)$$

where L is the average crystallite size, 0.94 is a constant for small spherical particles of similar size and distribution, λ is the wavelength of X-ray radiation (Cu Kα = 0.15405 nm), β is the full-width at half maximum (FWHM) in radians, and θ is the location of the (200) peak. As seen in Figure 3.4, the average size of the crystallite decreased as the amount of Cd was increased. When the amount of Cd was increased from 0% to 15%, the crystallite size decreased from 25.81 nm to 9.16 nm.

X-ray photoelectron spectroscopic (XPS) studies of the Pd-Cd(10%) sample verified the composition and revealed an electronic interaction between the Pd and Cd species upon alloying. Figure 3.5 shows the high resolution XPS spectra for the Pd 3d and Cd 3d regions. It was found that the actual surface contains a mixture of metallic Pd and Cd, as well as Pd and Cd in higher oxidation states. The Pd $3d_{5/2}$ peak is located at 335.2 eV and the Cd $3d_{5/2}$ peak is located at 404.0 eV. XPS was also performed on a Pd sample to examine the electronic interaction upon the addition of Cd. For pure Pd, the $3d_{5/2}$ peak is located at 335.5 eV, indicating a negative shift of 0.3 eV for PdCd(10%). The negative shift of the Pd 3d peak suggests that there is a slight electron transfer from Cd to Pd, which agrees with the electronegativity series (2.20 for Pd and 1.69 for Cd). Using the area of the fitted curves for the Pd and Cd in both the metallic and higher oxidation states, the ratio of metal/metal oxide was calculated. It was found that 88% of the Pd was in its metallic state and 76% of the Cd was in its metallic state. Both of these values are quite high, indicating that the hydothermal method of preparing the Pd-Cd nanostructures is efficient, and since only the surface layer was examined, the bulk of the Pd-Cd phase could be
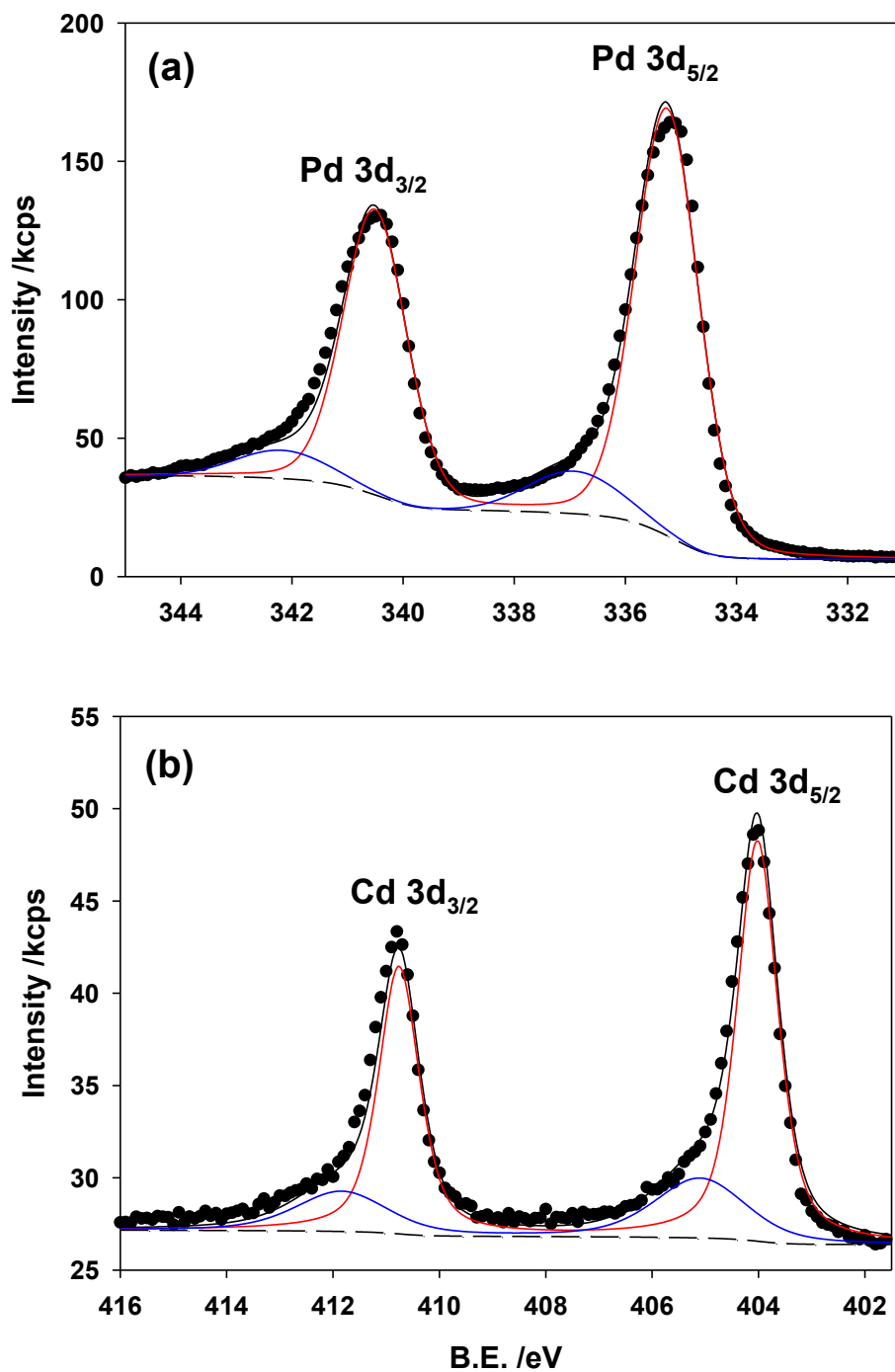
Figure 3.5. XPS spectra of the Pd 3d (a) and Cd 3d (b) regions for the Pd-Cd(10%) sample. The dots, dashed lines, and red, blue, and black solid lines represent the raw data, baseline, individual components (zero and high oxidation states) and total fit, respectively.

pure metals. The actual atomic composition of Cd was calculated, from the area under the peaks, to be 11.46 %. This is very close to the nominal ratio of 90:10 palladium to cadmium.

3.4 General Cyclic Voltammetric Behaviour of the PdCd Nanostructures

Figure 3.6 shows typical cyclic voltammograms (CVs) of the thin films of the PdCd nanostructures in 0.1 M HClO$_4$. There are three regions present in these cyclic voltammograms: the hydrogen region (1 and 2); the oxide region (3 and 4); and the double layer region (5). In the hydrogen region, absorption/adsorption (1) and subsequent desorption (2) take place, and in the oxide region, surface oxide formation (oxygen adsorption, 3), and oxide reduction (oxide desorption, 4) occur. These two regions are separated by the double layer region; a potential range where no faradic current flows.[22] It can be seen, however, that at this potential scan rate, the double layer almost disappears for the PdCd(10%) and PdCd(15%) nanostructures as the current due to the desorption of hydrogen carries into this range. It can also be noted that only one set of peaks are visible for hydrogen absorption/adsorption and desorption. This is thought to be because of the diffusion of dissolved hydrogen from the thicker nanostructured films to the surface as compared to the LVEs studied by others which only consist of electrodeposited monolayers.[8] The current due to the absorbed (and desorption of absorbed) hydrogen from the bulk of the metal hides current due to the adsorption (and desorption of adsorbed) hydrogen or hydrogen in the α-phase of the bulk metal. It should also be noted that, with an increasing amount of Cd, the adsorption/absorption current becomes increasingly negative and there is a negative shift in the peak potential. The area under both the adsorption and desorption peaks becomes larger with more Cd, indicating a larger amount of hydrogen can be electrosorbed.
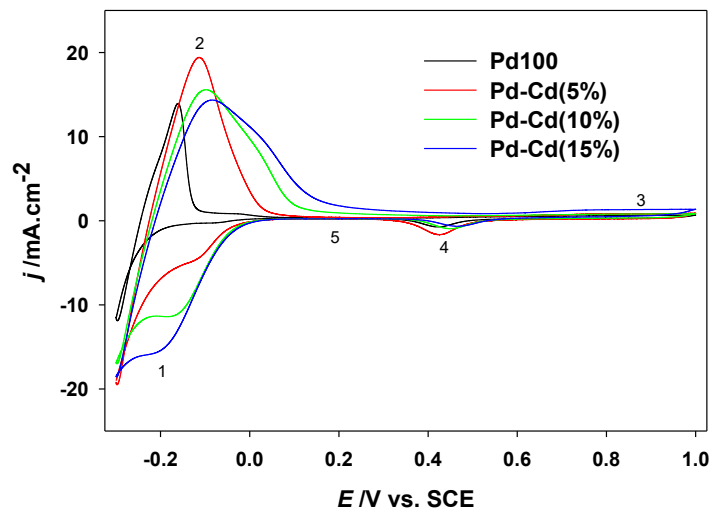
Figure 3.6. Cyclic voltammograms of the Pd-Cd nanostructures in 0.1 M HClO$_4$ at a scan rate of 20 mV/s.
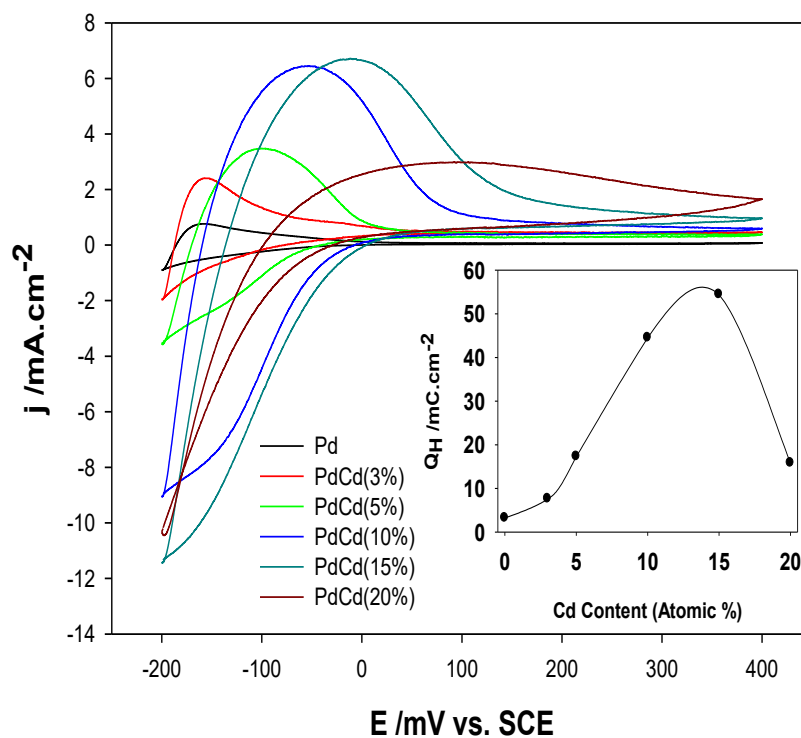

Figure 3.7. Cyclic voltammograms of the Pd-Cd electrodes in 0.1 M HClO$_4$ performed with a scan rate of 20 mV/s. The total hydrogen oxidation charge Q$_H$ vs. the normalized atomic composition of Cd is shown in the inset.

41

The capacity of the prepared Pd-Cd nanostructures for hydrogen adsorption/ absorption was studied with cyclic voltammetry. Figure 3.7 shows short-range cyclic voltammograms recorded in the hydrogen region (-200 to 400 mV) at a scan rate of 20 mV/s. Under the acid conditions used here, the region of hydrogen sorption/desorption can be clearly separated from the potential of the palladium oxide formation, which is contrary to the situation in alkaline solutions.[16,36,37] However, it is difficult to decouple adsorption from absorption.[8]

The total charge, Q_H, due to hydrogen adsorption and absorption in the Pd-Cd nanostructures was obtained by integrating the area under the anodic peaks in the cyclic voltammograms. The charges for hydrogen oxidation on the Pd-Cd nanostructures with 0%, 3%, 5%, 10%, 15%, and 20% Cd were 3.20, 7.57, 17.28, 44.45, 54.38, and 15.79 mC/cm^2, respectively. These electrochemical tests were determined to be reproducible within 10%. A maximum ratio of H/Pd between 0.6 and 0.71 has been reported, depending on the thickness of the Pd film.[8] This maximum ratio cannot be expressed here, however, since the Pd-Cd films were not saturated with hydrogen prior to the oxidation of hydrogen and the cathodic potential used is not negative enough to absorb a maximum amount of hydrogen. The Pd-Cd(15%) has the highest capacity for hydrogen adsorption/absorption. Further increasing Cd to 20% dramatically decreases the hydrogen adsorbing/absorbing capacity.

3.5 Sweep Rate Dependence of Hydrogen Electrosorption

The dependence of the sweep rate on the amount of hydrogen which was absorbed into the PdCd nanostructures was examined. Shown in Figure 3.8a are the cyclic voltammograms of the hydrogen region at various sweep rates for the PdCd(10%) electrode. The double layer region becomes clearly visible here as the sweep rate is decreased. The charge due to hydrogen desorption was calculated from the anodic part of the curves and is displayed in Figure 3.8b. The
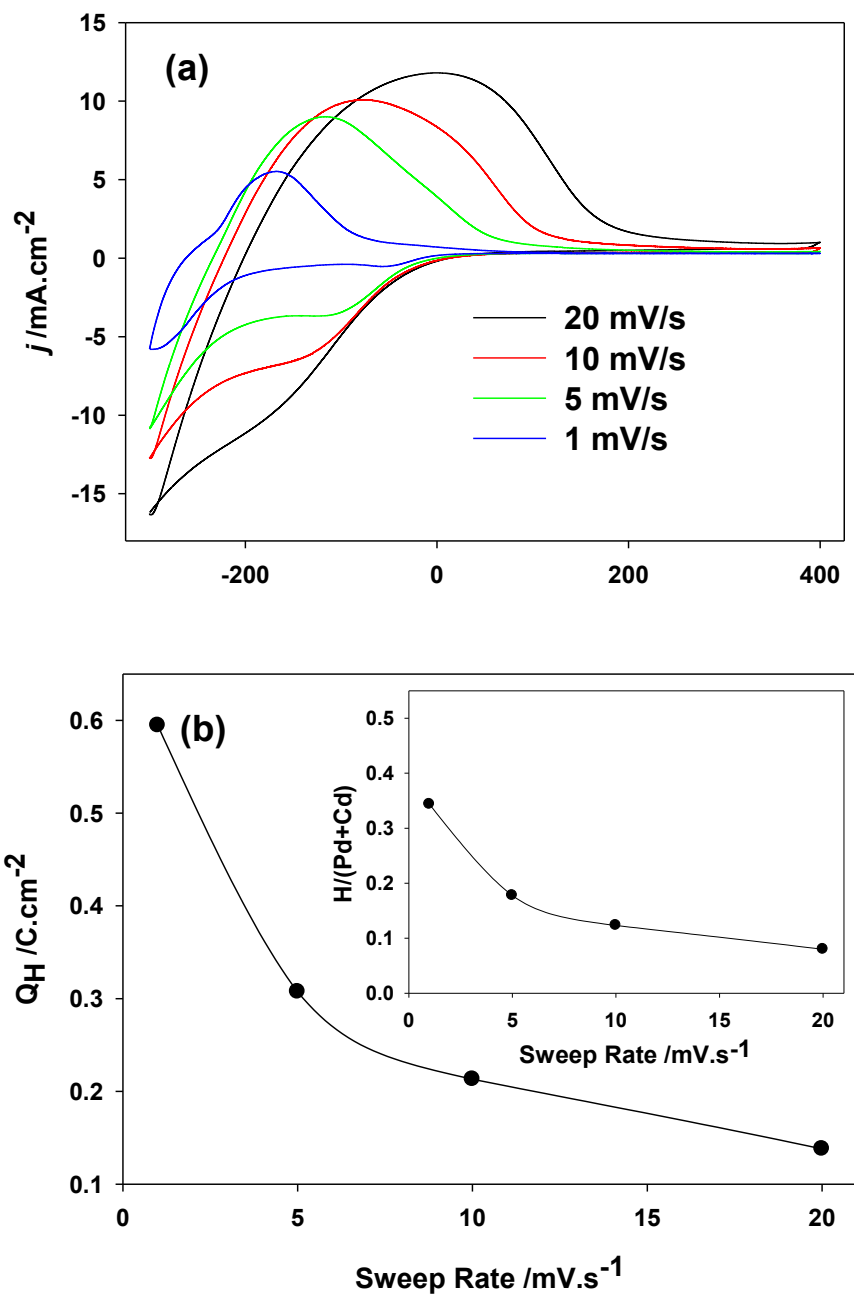
Figure 3.8. (a) Cyclic voltammograms of Pd-Cd(10%) in 0.1 M HClO$_4$ at various scan rates. (b) Charge due to hydrogen desorption versus sweep rate calculated by integrating the area under the anodic peaks in (a). Inset shows the H/(Pd+Cd) ratio versus sweep rate calculated based on the coating load of the Pd-Cd(10%) electrode used.

inset shows the H/(Pd+Cd) ratio which takes into consideration the mass of the PdCd(10%) coating. The amount of electrosorbed hydrogen increases considerably with a slower sweep rate from a H/(Pd+Cd) ratio of less than 0.1 with 20 mV/s to about 0.35 for 1 mV/s.

In order to better study the hydrogen sorbing capabilities of the PdCd nanostructures and to attain the maximum amount of hydrogen which can be adsorbed/absorbed, an extremely slow sweep rate is necessary. The electrodes were saturated with hydrogen by holding the potential for a period of time prior to running the CVs in the next section.

3.6 Potential and Composition Dependence of Hydrogen Electrosorption

The electrosorption of hydrogen into the PdCd nanostructures was examined at various potentials, from 0 to -325 mV. The potential was first held at a constant potential; cyclic voltammetry was run immediately after. The potential was held for 10 minutes, which was much longer than necessary to ensure complete saturation of hydrogen. Figure 3.9 shows the anodic sweeps (desorption of hydrogen) of the CVs of the Pd and PdCd(10%) nanostructures after complete saturation with hydrogen at various potentials. The full desorption of hydrogen was obtainable at 20 mV/s after saturation as proved by the completion of the anodic curves to the double layer before the limit of 400 mV. For Pd, there is a sharp transition between -225 and -250 mV. The amount of desorbed hydrogen at potentials more positive than -225 mV is negligible compared to that at -250 mV and below. For PdCd(10%), the transition is more gradual, and there is still a significant amount of hydrogen desorbed above -225 mV. This transition is the α to β phase transition where both phases exist mutually. For Pd, at potentials more positive than -225 mV, there is exclusive α-phase hydrogen, and at potentials ≤ -250 mV there is exclusive β-phase hydrogen.
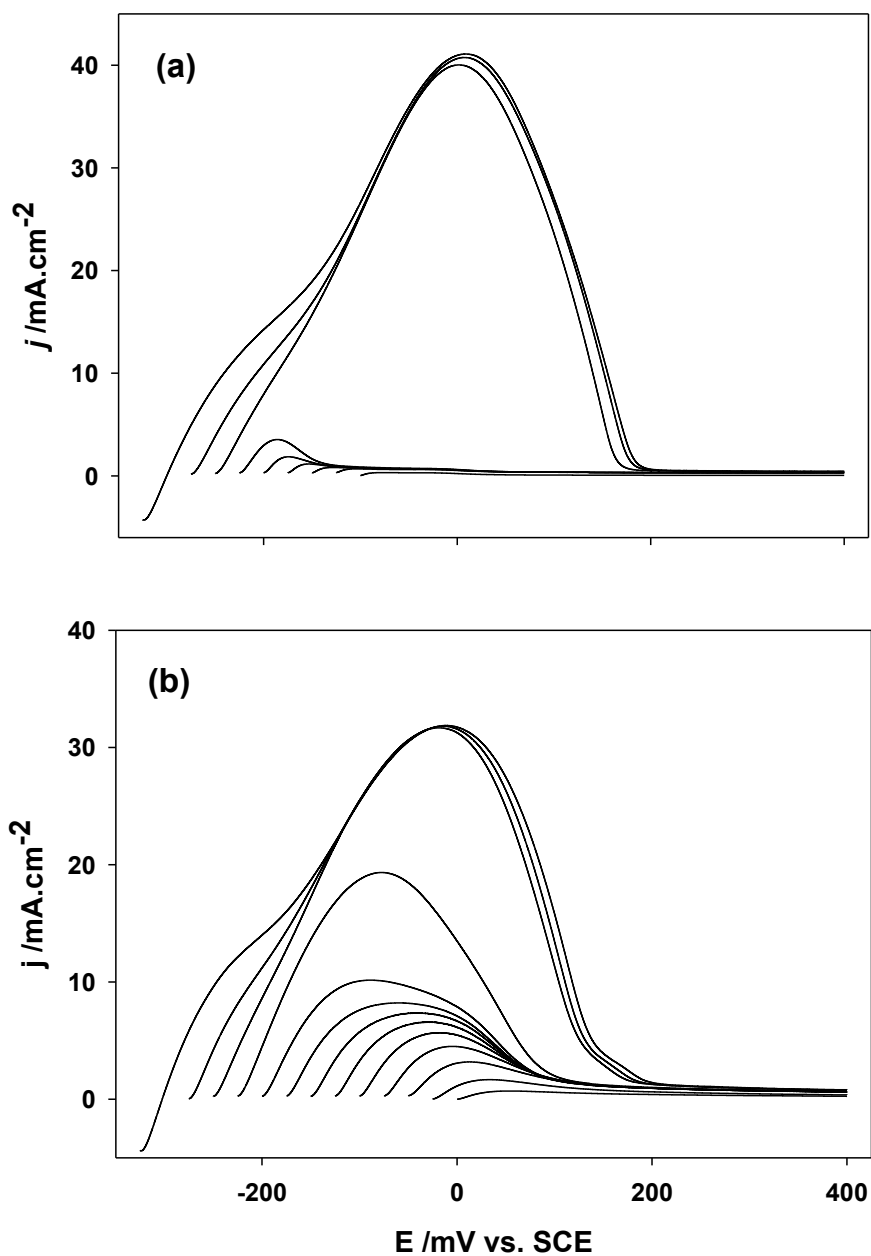
Figure 3.9. Anodic sweeps of the desorption of hydrogen from (a) Pd and (b) Pd-Cd(10%) after holding the potential at various cathodic limits for 10 minutes in 0.1 M HClO$_4$. The scan rate was 20 mV/s in all cases.

The H/(Pd+Cd) ratio was calculated using the same procedure described above in Section 3.6 for electrodes containing less than 15 at.% Cd at various anodic potentials ranging from -325 to 0 mV (Figure 3.10). Pure Pd exhibits the highest maximum value of H/metal ratio of approximately 0.66 at the potential of -325 mV. The maximum H/(Pd+Cd) ratio is seen at -325 mV for all of the PdCd compositions studied. At potentials more negative than this, a substantial amount of hydrogen evolution was observed and this caused cracking and loss of the nanostructured coatings to the electrolyte solution. For the electrodes with a very small amount of Cd (i.e., 0 to 5 at.%), a slight decrease in the amount of hydrogen, which may be electrosorbed, is observed from -325 to -250 mV (β-phase hydrogen), at which point there is a sharp decrease (β to α-phase transition), and only α-phase hydrogen is seen at potentials more positive than -225 mV. For the PdCd(10%) and PdCd(15%) nanostructures, the phase transition is very gradual and can barely be distinguished. For these particular electrodes, there is a considerable amount of hydrogen absorbed in the α-phase. The H/(Pd+Cd) ratio does not reach minimal values until 0 mV for PdCd(10%) and PdCd(15%). This is an excellent trait for a hydrogen selective membrane material, as the abrupt phase transition of Pd is what causes embrittlement.

The dependence of the H/(Pd+Cd) ratio on the composition of Cd in the PdCd nanostructures is displayed in Figure 3.11. It can clearly be seen in this figure that while the amount of β-phase hydrogen decreases with an increasing amount of Cd, the amount of α-phase hydrogen increases substantially. At potentials more positive than -225 mV (α-phase hydrogen region), the solubility of hydrogen is much higher for PdCd alloys than pure Pd. This potential region is analogous to low hydrogen gas pressures in hydrogen sorption measurements carried out in the gas phase.[18] This enhanced solubility effect with the addition of Cd is what was seen in
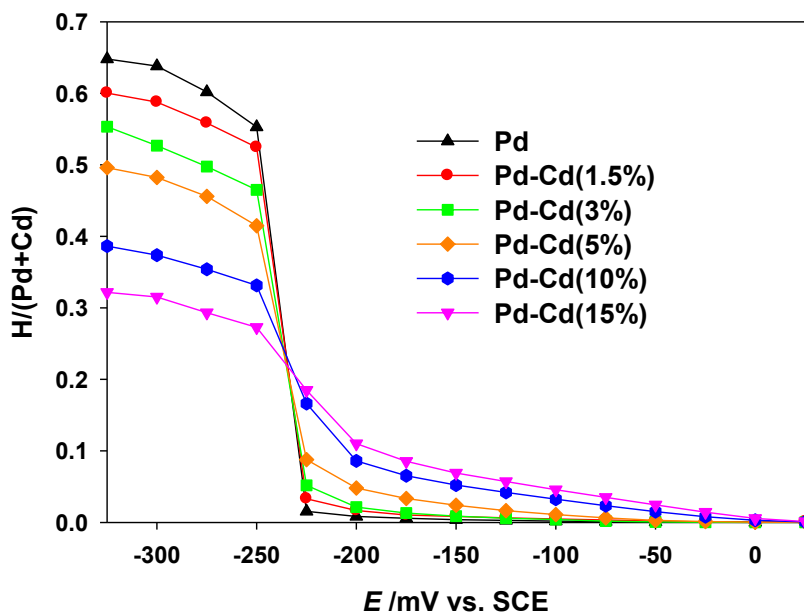
Figure 3.10. H/(Pd+Cd) ratio versus potential for Pd-Cd nanostructures with various compositions indicated on the figure.
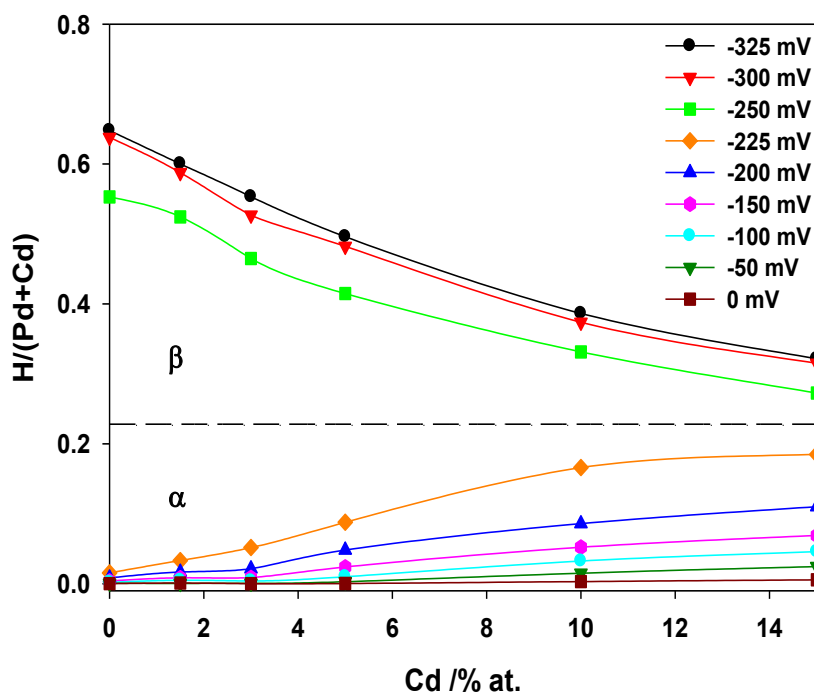
Figure 3.11. H/(Pd+Cd) values versus Cd composition at various potentials indicated on the figure.

Figure 3.7, performed at -200 mV. At this potential, it was found that Pd-Cd(15%) has a hydrogen sorption capacity of approximately 17 times that of pure Pd.

3.7 Kinetics of the Electrosorption of Hydrogen

Figure 3.12a presents a series of chronoamperograms for pure Pd after a potential step from the double layer region (300 mV) to different potentials in the hydrogen region. After this step to a more negative potential, current begins to flow due to the reduction of H^+ ions to H atoms adsorbed on the surface of the Pd and subsequent entry of the H atoms into the Pd (or PdCd) crystal lattice.[22] This forms a bulk phase of absorbed hydrogen in the α or β phase depending on the applied potential. This adsorption/absorption process can be described by the following equations:[7,39]

$$H^+ + M + e^- \rightleftharpoons MH_{ads} \tag{3.6}$$

$$MH_{ads} + M_{subsurface} \rightleftharpoons M_{surface} + MH_{abs \ (subsurface)} \tag{3.7}$$

$$MH_{abs \ (subsurface)} \rightarrow MH_{abs \ (bulk, \ \alpha+\beta)} \tag{3.8}$$
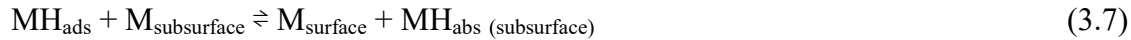
It should be noted that after a certain amount of time, the current reaches a steady state. The current eventually falls to zero at potentials where hydrogen evolution does not occur, as can be expected once the Pd (or PdCd) layer becomes completely saturated with hydrogen. For potentials lower than approximately -250 mV, hydrogen evolution occurs and this results in a negative current. This is determined by the rate of the hydrogen evolution reaction at the surface of the electrode according to one of the following equations:[7,39]

$$MH_{ads} + H^+ + e^- \rightleftharpoons M + H_2 \tag{3.9}$$

Or

$$2MH_{ads} \rightleftharpoons 2M + H_2 \tag{3.10}$$
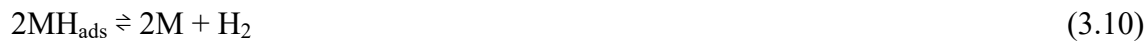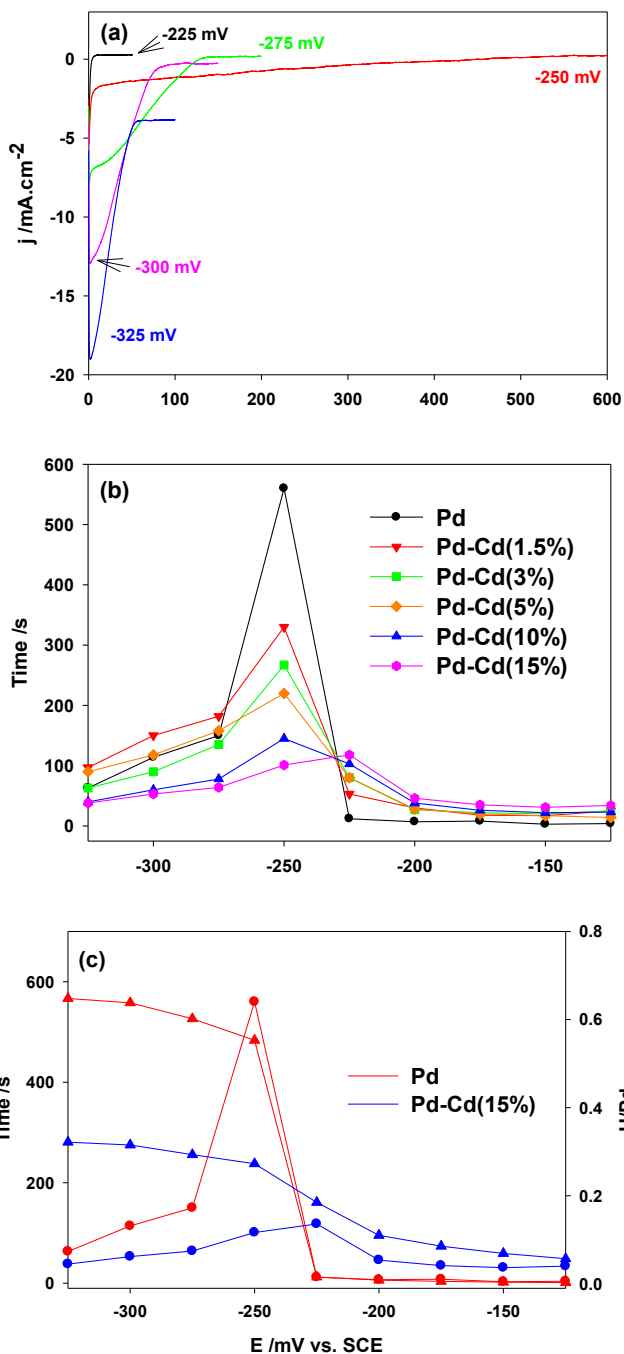
Figure 3.12. Chronoamperometric curves for the electrosorption of hydrogen in the Pd electrode recorded in 0.1 M HClO$_4$ after pre-treatment at 300 mV (a), the time required for obtaining steady state saturation of the electrodes with absorbed hydrogen with respect to potential (b), and an overlay showing the H/(Pd+Cd) ratio (triangles) and time to reach steady state (circles) versus potential for the Pd and Pd-Cd(15%) electrodes(c).

From the chronoamperometric curves, the time to obtain steady-state electrode saturation with hydrogen was determined at various potentials, and is displayed in Figure 3.12b. With a decrease in the electrode potential, the absorption time initially increases until a sharp maximum occurs, and then decreases. The time maxima occurs at the same potential (-250 mV) for all compositions of PdCd except the PdCd(15%) which occurs at -225 mV. A comparison of the potential for time maxima with the respective H/(Pd+Cd) ratio reveals that the potentials are always within the phase transition region (Figure 3.12c), which is consistent with the previous studies.[18,20] This maximum on the *t-E* plot represents the potential at which the slowest absorption step occurs, revealing that the α to β phase transition is the rate limiting step in the absorption process rather than surface kinetics or bulk diffusion. With increasing amounts of Cd, the time maxima is decreased so much that with PdCd(15%) only a slight hump is observed, rather than the sharp peak. This fits with the α to β phase transition being the slowest step, as it was shown in Section 3.4 that the phase transition is diminished with the addition of Cd. The enhanced solubility of hydrogen in PdCd alloys with respect to pure Pd is attributed almost solely to the larger size of the Cd atoms, similar to PdAg.[14,24,40-43]

3.8 Summary

In summary, the electrosorption of hydrogen into nanostructured films of Pd-Cd alloys ranging from 0 at.% to 15 at.% Cd has been systematically studied. The nanostructures were fabricated using a simple hydrothermal reduction technique. Cyclic voltammetric studies showed that the sweep rate has a major influence on the amount of hydrogen which can be absorbed into the Pd-Cd nanostructures. By decreasing the sweep rate, a larger amount of hydrogen can be electrosorbed, indicating that, if only cyclic voltammetric studies are performed, the amount of electrosorbed hydrogen is limited by the sweep rate. A combination of chronoamperometry and

cyclic voltammetry proved to be a more effective method for examining the maximum amount of hydrogen which can be electrosorbed into the Pd-Cd nanostructures.

Both potential and composition were found to be major factors in the H/(Pd+Cd) ratio. The maximum H/(Pd+Cd) ratio was found to be the highest for pure Pd (0.66). The maximum was found to always occur at -325 mV for every composition, but the value decreased with an increasing amount of Cd. Two distinct phases (α and β), with a sharp phase transition between -225 mV and -250 mV, were observed for pure Pd; however, this phase transition was diminished with increasing amounts of Cd. In particular, compositions of PdCd alloys with a higher Cd content (i.e. 10 at% and 15at%) barely displayed any phase transition, and were capable of electrosorbing much more hydrogen at higher potentials (in the α phase) than pure Pd. Our study has shown that the phase transition is the slowest step in the hydrogen absorption process and, therefore, with the doping of Cd, the kinetics is much quicker. The combination of enhanced solubility of hydrogen and diminishing of the α and β-phase transition in PdCd alloys relative to pure Pd makes the Pd-Cd nanostructures attractive for hydrogen selective membranes and hydrogen dissociation catalysts.

References

1. J. Wang, D.F. Thomas, A. Chen, *Chem. Commun*. **2008**, 5010.

2. Y.-J. Zhang, Y. Zhang, Z.-H. Wang, D. Li, T.-Y. Cui, Z.-D. Zhang, *Eur. J. Inorg. Chem*. **2008**, 2733.

3. H. Wang, D.W. Brandl, F. Le, P. Nordlander, N.J. Halas, *Nano Lett*. **2006**, *6*, 827.

4. S. Kishore, J.A. Nelson, J.H. Adair, P.C. Eklund, *J. Alloy. Compd*. **2005**, *389*, 234.

5. M. Yamauchi, R. Ikeda, H. Kitagawa, M. Takata, *J. Phys. Chem. C*. **2008**, *112*, 3294.

6. H. Kobayashi, M. Yamauchi, H. Kitagawa, Y. Kubota, K. Kato, M. Takata, *J. Am. Chem. Soc*. **2008**, *130*, 1828.

7. C. Gabrielli, P.P. Grand, A. Lasia, H. Perrot, *J. Electrochem. Soc*. **2004**, *151*, A1925.

8. C. Gabrielli, P.P. Grand, A. Lasia, H. Perrot, *J. Electrochem. Soc*. **2004**, *151*, A1937.

9. B. Losiewicz, L. Birry, A. Lasia, *J. Electroanal. Chem*. **2007**, *611*, 26.

10. H. Duncan, A. Lasia, *Electrochim. Acta*. **2008**, *53*, 6845.

11. Y. Chen, C. Sequeira, T. Allen, C.P. Chen, *J. Alloy. Compd*. **2005**, *404-406*, 661.

12. R.-R. Jeng, S.-L. Lee, C.-W. Hsu, Y.-P. Wu, J.-C. Lin, *J. Alloy. Compd*. **2008**, *464*, 467.

13. A. Visintin, L.A. Tori, G. Gaaventta, W.E. Triaca, *Electrochem. Soc*. **1998**, *145*, 4169.

14. Y. Sun, Z. Tao, J. Chen, T. Herricks, Y. Xia, *J. Am. Chem. Soc*. **2004**, *126*, 5940.

15. M. Grdeń, A. Czerwiński, J. Golimowski, E. Bulska, B. Krasnodębska-Ostręga, R. Marassi, S. Zamponi, *J. Electroanal. Chem*. **1999**, *460*, 30.

16. A. Czerwiński, I. Kiersztyn, M. Grden, J. Czapla, *J. Electroanal. Chem*. **1999**, *471*, 190.

17. M. Grdeń, A. Piaścik, Z. Koczorowski, A. Czerwiński, *J. Electroanal. Chem*. **2002**, *532*, 35.

18. M. Słojewski, J. Kowalska, R. Jurczakowski, *J. Phys. Chem. C* **2009**, *113*, 3707.

19. A. Żurowski, M. Łukaszewski, A. Czerwiński, *Electrochim. Acta* **2008**, *53*, 7812.

20. A. Żurowski, M. Łukaszewski, A. Czerwiński, *Electrochim. Acta* **2006**, *51*, 3112.

21. M.H. Martin, A. Lasia, *Electrochim. Acta* **2008**, *53*, 6317.

22. M. Łukaszewski, A. Czerwiński, *J. Solid State Electrochem*. **2008**, *12*, 1589.

23. U. Stuhr, T. Striffler, H. Wipf, H. Natter, B. Wettmann, S. Janssen, R. Hempelmann, H. Hahn, *J. Alloy Comp*. **1997**, *253*, 393.

24. H. Li, H. Xu, W. Li, *J. Membrane Sci*. **2008**, *324*, 44.

25. B.D. Adams, G. Wu, S. Nigro, A. Chen, *J. Am. Chem. Soc*. **2009**, *131*, 6930.

26. B.D. Adams, C.K. Ostrom, A. Chen, *Langmuir*, **2010**, *26, 7632.

27. E. Ben-Jacob, P. Garik, *Nature* **1990**, *343*, 523.

28. L. Gránásy, T. Pusztai, J.A. Warren, J.F. Douglas, T. Borzsonyi, V. Ferreiro, *Nature Mater.* **2003**, *2*, 92.

29. T. Haxhimali, A. Karma, F. Gonzales, M. Rappaz, *Nature Mater.* **2006**, *5*, 660.

30. H. Imai, *Top. Curr. Chem.* **2007**, *270*, 43.

31. V. Fleury, *Nature*, **1997**, *390*, 145.

32. Y. Huang, X. Zhou, J. Liao, C. Liu, T. Lu, W. Xing, *Electrochem. Commun.* **2008**, *10*, 1155.

33. H. Barlag, L. Opara, H. Zuchner, *J. Alloy. Compd.* **2002**, *330-332*, 434.

34. G. Fagherazzi, P. Canton, P. Riello, N. Pernicone, F. Pinna, M. Battagliarin, *Langmuir* **2000**, *16*, 4539.

35. C. Amorin, M.-A. Keane, *J. Colloid Inter. Sci.* **2008**, *322*, 196.

36. E.A. Baranova, Y. Le Page, D. Ilin, C. Bock, B. MacDougall, P.H. Mercier, *J. Alloy. Compd.* **2009**, *471*, 387.

37. A.E. Bolzan, *J. Electroanal. Chem.* **1995**, *380*, 127.

38. L. Yang, Y.-T. Cheng, *Int. J. Hydrogen Energy.* **1996**, *21*, 281.

39. A. Lasia, *J. Electroanal. Chem.* **2006**, *593*, 159.

40. E.L. Foletto, J.V.W. Da Silveira, S.L. Jahn, *Lat. Am. Appl. Res*. **2008**, *38*, 79.

41. W.-H. Lin, H.-F. Chang, *Surf. Coat. Tech*. **2005**, *194*, 157.

42. G. Zeng, A. Goldbach, H. Xu, *J. Membrane Sci*. **2009**, *326*, 681.

43. A.K.M. Fazle, Y. Sakamoto, *Int. J. Hydrogen Energ*. **2000**, *25*, 853.

Chapter 4

Hydrogen Spillover from Pd-based Nanoparticles to Activated Carbon

4.1 Introduction

Hydrogen spillover is a mechanism well documented for heterogeneous catalytic reactions.[1] It is described as dissociative adsorption of H_2 on metal catalyst particles, followed by migration of H atoms to the support, and diffusion of H atoms on the support and/or reaction at remote surface sites.[2-4] Hydrogen spillover from metal particles to carbon materials can be assessed in a number of ways, but perhaps the most common is simple measurement of the hydrogen capacity of the metal and the hydrogen capacity of the carbon material at a given H_2 pressure. If spillover occurs, it is expected that the hydrogen capacity of the combined system (carbon + metal) exceeds that of the individual components.[5]

Recent DFT calculations have shown that the migration of atomic hydrogen from the metal nanoparticle to a graphitic substrate is kinetically and thermodynamically inefficient and limits the rate of H spillover.[3,6] Although the hydrogen spillover effect has been observed for Pd-doped activated carbon,[7] other experimental studies have revealed that a further enhancement of the storage capacity of metal-doped activated carbons can be achieved by chemically modifying the carbon substrate through introducing oxygen functionalities.[8,9] Moreover, it was observed that Pd-doped graphite oxide exhibited 3.8 times the capacity of Pd-doped superactivated carbon AX-21, when the uptake was normalized by the specific surface area of the materials.[9] The role of oxygen functional groups in enhancing the hydrogen uptake by spillover may also be operative in the work of Yang's group,[10,11] where the materials were functionalized by mixing

them with "carbon bridges" that are composed of carbonized sugar molecules, and may have contained O left over from the carbonization.

On the topic of hydrogen spillover to carbon materials, most work seems to be focused on increasing the hydrogen capacity by modifying the carbon material, for instance introducing O-containing functional groups. Pozzo and Alfè[12] performed a systematic DFT/PBE study of hydrogen dissociation and subsequent diffusion over Mg surfaces doped with different transition metals. The dopants investigated were Ti, Zr, V, Fe, Ru, Co, Rh, Ni, Pd, Cu and Ag. They found that the transition metals on the left of the periodic table (Ti, V, Zr), together with Ru, eliminate the dissociation barrier altogether; however, the products stick too strongly to the metal dopant, therefore hindering diffusion away from the catalytic sites. This would result in a quick deactivation of the catalyst and therefore a slow absorption process. On the contrary, the transition metals on the right of the periodic table do not bind the H atoms too strongly allowing easy diffusion. However, their effect on the dissociation barrier is small. Based on their results, it appears that an optimal hydrogen dissociation catalyst should have not only good dissociation abilities, but also a low sticking strength of the dissociated hydrogen atoms to the metal. Pd shows a good compromise of these properties but could possibly be further enhanced by alloying Pd with other metals.

In this study, the hydrogen adsorption properties of a commercially available activated carbon material (Norit PAC 200 (M-1620)) are examined at 77 K and room temperature. By dispersing catalysts onto the surface of the activated carbon, the effect of three different Pd-based hydrogen dissociation catalysts, Pd, PdAg and PdCd nanoparticles, was systemically examined for the first time. Compositions of $Pd_{0.85}Cd_{0.15}$ and $Pd_{0.77}Ag_{0.23}$ were strategically chosen to be compared to Pd based on our recent electrochemical studies of PdCd [13,14] and other

research on PdAg,[15,16] showing that they both have similar geometric properties and optimal hydrogen permeability for hydrogen absorption. The objective of this study is to investigate the electronic effect of such alloys in attempts to design high-performance hydrogen dissociation catalysts for hydrogen spillover. The present study shows that at 77K, the catalysts have no effect, and the hydrogen capacity of the materials is strictly related to the specific surface area. At room temperature, hydrogen spillover is observed from the catalysts to the carbon material, and the hydrogen capacity depends on the adsorption strength of the dispersed catalysts. Our study reveals that the PdCd nanoparticles have a very high hydrogen spillover enhancement of 108%.

4.2 Experimental Section

Commercially available activated carbon, Norit PAC 200 (M-1620), from Norit Americas Inc. was used in this study and was chosen due to its high surface area, powder form, and microporous structure. This carbon material has been referred to simply as PAC200. The Pd/PAC200, PdCd/PAC200, and PdAg/PAC200 samples were prepared using the room temperature impregnation method for carbon-supported nanoparticles as described in Chapter 2. The metal precursors used were $PdCl_2$, $Pd(NO_3)_2 \cdot 2H_2O$, $Cd(NO_3)_2 \cdot 4H_2O$, and $AgNO_3$. The amount of carbon used in the preparation of each sample was 3 g, and the according quantities of metal precursors used is shown in Table 4.1, such that the coating load of metal was 5 wt.% in all cases.

The PAC200 and synthesized samples were characterized by TEM, XPS, ICP-AES and gas adsorption/desorption analysis. The N_2 and H_2 gas adsorption studies were performed using a Quantachrome Nova 2200 surface area and pore size analyzer as described in Chapter 2. DFT

calculations were carried out for Pd, Cd, and Ag atoms, as well as Pd-H, Cd-H, and Ag-H molecules with the method described in Chapter 2.

4.3 Surface Analysis of Activated Carbon and Catalysts

Transmission electron microscopy (TEM) was used to characterize the morphology of the prepared catalyst dispersed carbon samples. Typical TEM images of the activated carbon (PAC200), Pd/PAC200, PdCd/PAC200, and PdAg/PAC200 are displayed in Figure 4.1. It can be seen that the unmodified carbon (Figure 1a) possess a microporous structure with most pores less than 3 nm in diameter. The Pd particles on the Pd/PAC200 sample (Figure 4.1b) are very well dispersed and have a narrow size distribution of less than 3 nm in diameter. The Pd nanoparticles appear to be imbedded within the porous structure of the carbon. The PdCd nanoparticles on the PdCd/PAC200 sample (Figure 4.1c) are larger in size than the Pd nanoparticles (Figure 4.1b). The particles range in diameter from 3 to 6 nm, and seem to be situated on the surface of the carbon rather than within micropores as seen for the Pd/PAC200 sample. The PdCd particles are not as well dispersed as the Pd particles and are concentrated in certain areas on the carbon. Compared to the Pd/PAC200 and PdCd/PAC200 samples, the PdAg nanoparticles of the PdAg/PAC200 sample (Figure 4.1d) are the largest in size with a diameter range of 4 – 10 nm. The particles are fairly well dispersed. However, like the PdCd/PAC200 sample, the PdAg nanoparticles are mainly located on the surface of the carbon, since the particles are too large to be imbedded into the pores of the carbon.

The composition of the Pd-based catalysts dispersed on the carbon materials was analyzed using both ICP-AES indirectly and XPS directly. A sample of the solutions with the metal precursors before and after the preparation of the Pd/PAC200, PdCd/PAC200, and PdAg/PAC200 materials was analyzed with ICP for the metal contents of Pd, Pd-Cd and Pd-Ag,
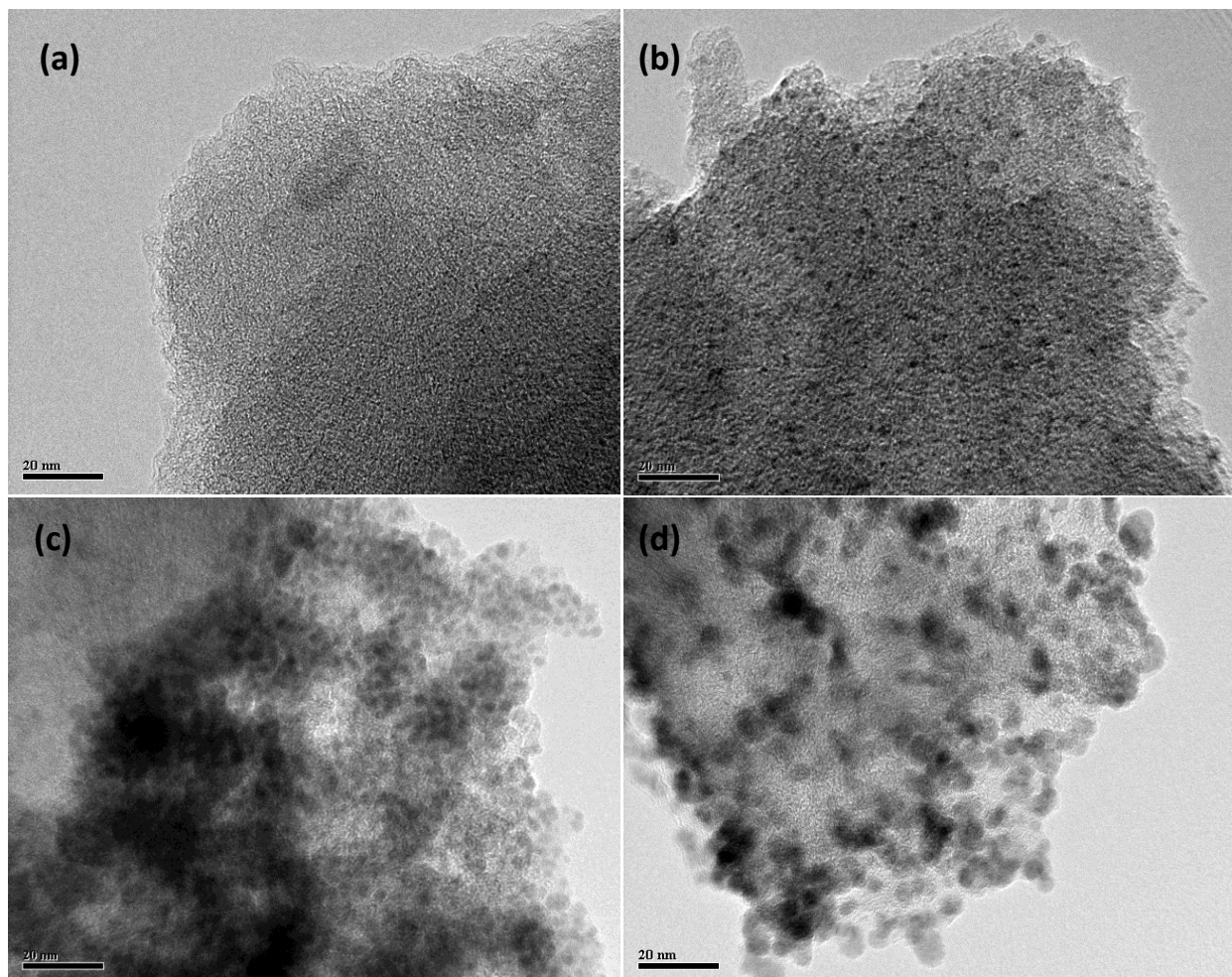
Figure 4.1. TEM images of PAC200 (a), Pd/PAC200 (b), PdCd/PAC200 (c), and PdAg/PAC200 (d).

respectively. Less than 10 ppm of metal remained in solution in all cases, indicating that the metal precursors were completely reduced by sodium borohydride. Through subtraction of the final metal concentrations from the initial metal concentrations, it was found that the bulk composition of the dispersed particles was exactly equal to the input compositions and the coating loads were also as designed (5 wt.% metal in all cases). These results are tabulated in Table 4.1 along with the surface composition results measured from XPS.

The XPS survey scan for the four samples used in this study are displayed in Figure 4.2a. For all the samples, a carbon 1s peak at around 285 eV and an oxygen 1s peak at around 531 eV are observed. The intensity of the oxygen 1s peak is greater for the metal dispersed samples than that for the pure PAC200 sample, indicating that the surface metal particles are partially oxidized. For all three metal dispersed samples, Pd 3d and 3p peaks are observed at around 340 eV and 565 eV, respectively. For the PdCd/PAC200 and PdAg/PAC200 samples, Cd 3d doublets and Ag 3d doublets are also seen centered at around 410 eV and 370 eV, respectively. The high resolution spectra for the Pd 3d region are shown for the Pd/PAC200 (Figure 4.2b), PdCd/PAC200 (Figure 4.2c), and PdAg/PAC200 (Figure 4.2e) samples. The Cd 3d region for the PdCd/PAC200 sample is displayed in Figure 4.2d and the Ag 3d region for the PdAg/PAC200 sample is presented in Figure 4.2f. The Pd $3d_{5/2}$ peak for the Pd/PAC200 and PdCd/PAC200 samples is located at 335.6 eV. However, this peak shifts to 335.8 eV for the PdAg/PAC200 sample. The Cd $3d_{5/2}$ peak is located at 405.1 eV and the Ag $3d_{5/2}$ peak occurrs at 367.7 eV. The above results indicate that the electronic interaction between Pd and Cd in the PdCd particles is weak and that there is some electron density exchange from Pd to Ag in the PdAg particles.

The surface compositions of the metal particles as shown in Table 4.1 were calculated using the area under each of the high resolution 3d metal peaks. It was found that the surface

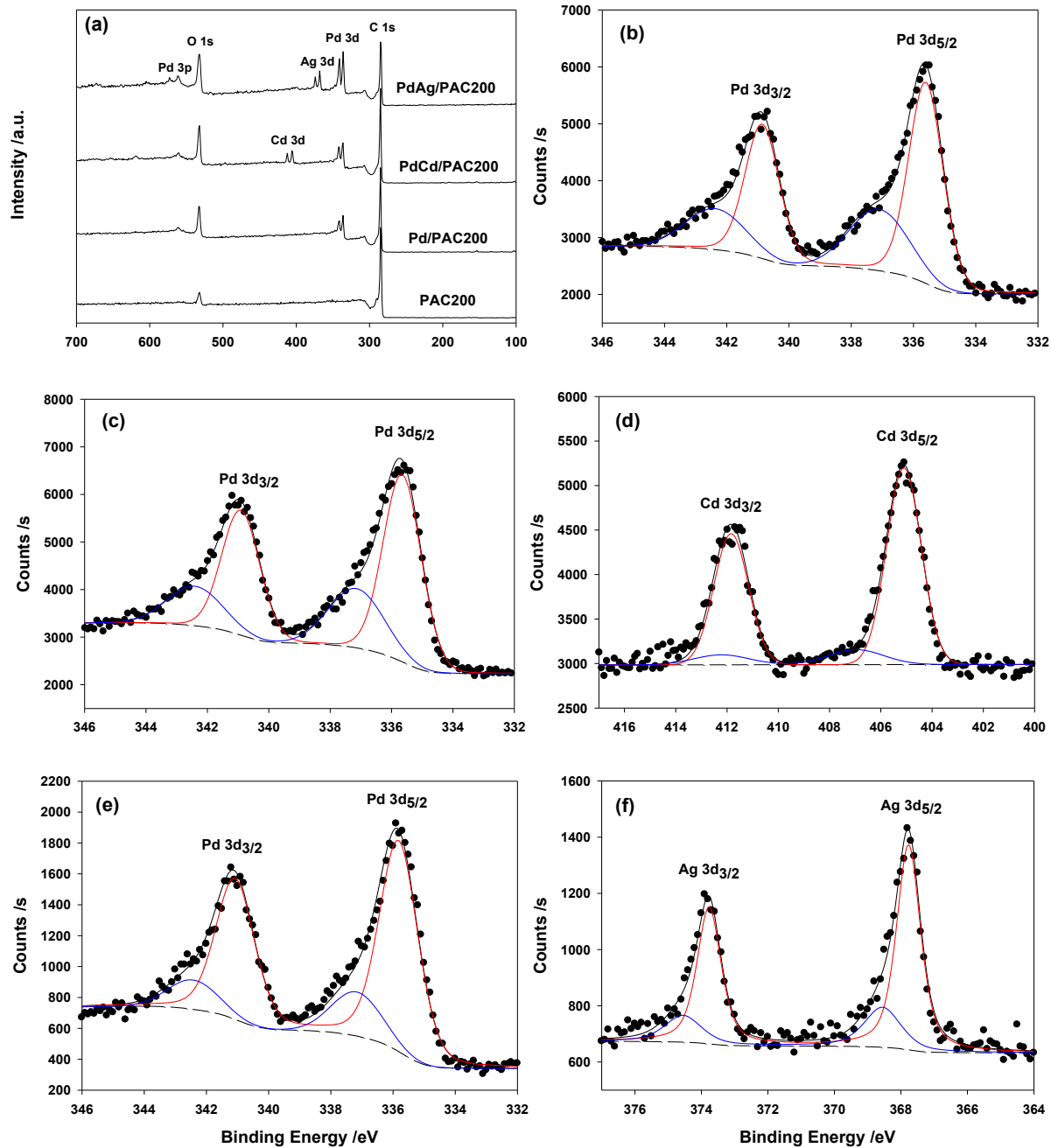**Figure 4.2**. XPS survey scan of the four samples (a); high resolution spectra of the Pd 3d region of Pd/PAC200 (b); Pd 3d region (c) and Cd 3d region (d) of PdCd/PAC200; Pd 3d region (e) and Ag 3d region (f) of PdAg/PAC200. For the high resolution spectra, the dots, dashed lines, and red, blue, and black solid lines represent the raw data, baseline, individual components (zero and high oxidation states) and total fit, respectively.

Table 4.1. Reactant quantities for the preparation of the catalyst dispersed carbon samples along with the corresponding bulk composition of the dispersed metal particles determined by ICP-AES and the surface composition of the particles determined by XPS.

Sample	Metal Precursors	Bulk Composition[a]	Surface Composition[b]
Pd/PAC200	$PdCl_2$ (1.48 mmol)	Pd	Pd
PdCd/PAC200	$PdCl_2$ (1.25 mmol) $Cd(NO_3)_2 \cdot 4H_2O$ (0.22 mmol)	$Pd_{0.85}Cd_{0.15}$	$Pd_{0.73}Cd_{0.27}$
PdAg/PAC200	$Pd(NO_3)_2 \cdot 2H_2O$ (1.14 mmol) $AgNO_3$ (0.34 mmol)	$Pd_{0.77}Ag_{0.23}$	$Pd_{0.75}Ag_{0.25}$

[a] The bulk catalyst composition is the atomic composition of the metal precursors used and was also verified to be the actual bulk composition with ICP-AES. [b] The surface composition of the metal particles is the atomic composition determined with XPS by integrating the area under the high resolution metal 3d peaks.

composition of the PdAg particles was very close to the bulk concentration, whereas the PdCd particles were enriched with Cd on the surface compared to the bulk composition. This can be attributed to the difference in reduction potentials between the Pd^{2+}, Ag^+, and Cd^{2+}. Since both Pd^{2+} and Ag^+ are easily reduced, the relative quantites of Pd and Ag grow at a similar rate in the PdAg particles. Cd^{2+}, on the other hand, is much more difficult to be reduced compared to Pd^{2+} and, therefore, the growth of the PdCd particles begins mainly with Pd atoms and leads to more Cd near the outer surface.

The BET surface areas and pore structures of the samples were studied by N_2 adsorption and desorption at 77 K. Figure 4.3a presents a typical N_2 adsorption/desorption isotherm at 77 K for the PAC200 sample. This type IV isotherm was observed for all of the samples, and the closure at approximately $P/P_0 \sim 0.45$ indicates the presence of small mesopores. The isotherms were fitted using the Quenched Solid Density Functional Theory (QSDFT) method as shown in Figure 4.3b and, using this method, pore size distribution plots were obtained for each of the samples (Figure 4.3c). This method had a much better fitting correlation than the Non-local Density Functional Theory (NTDFT) method[17,18] commonly used for pore size characterization,

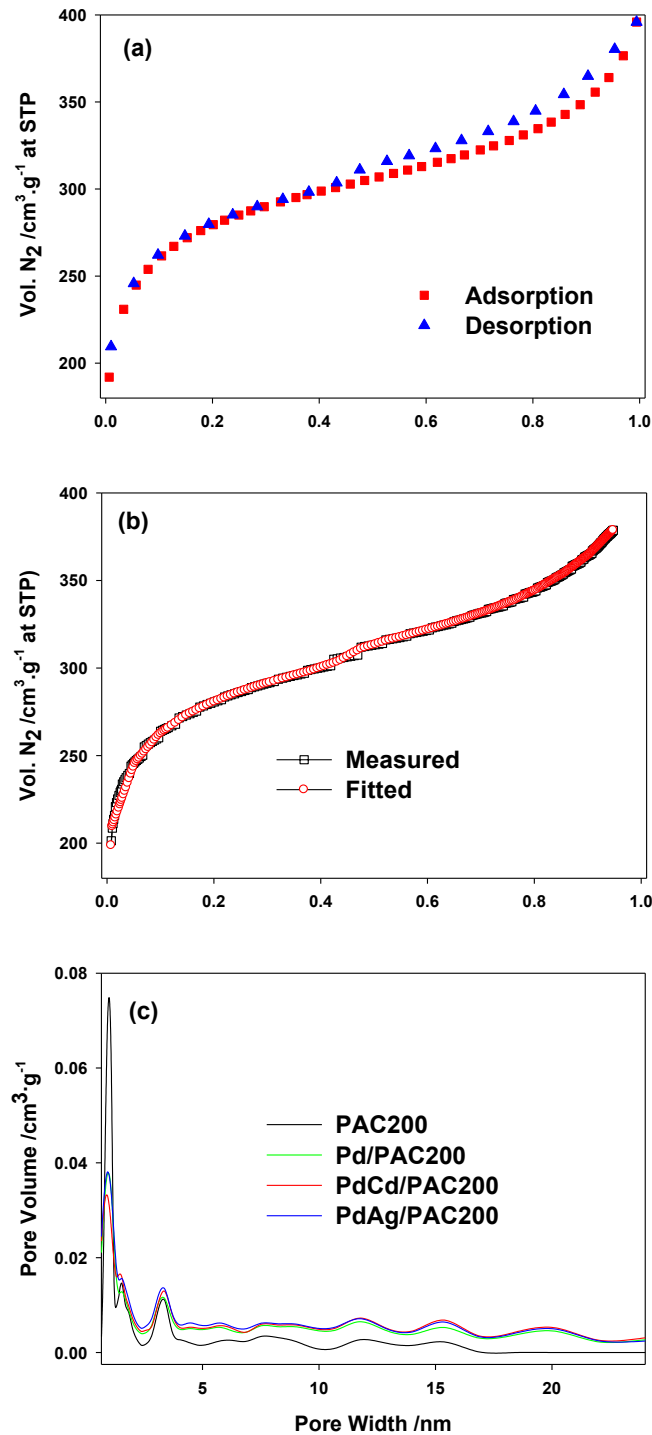**Figure 4.3**. N$_2$ adsorption/desorption isotherm at 77 K on the PAC200 (a) and the corresponding desorption curve fitted using the QSDFT method for slit pores (b). The pore size distributions using the QSDFT method are displayed in (c).

and had a fitting error of less than 0.3% in all cases. The pore size distribution plots show the three main pore specimens. The micropore peak at approximately 0.96 nm is the largest for the pure carbon sample and decreases for the metal dispersed samples. This is due to the metal particles blocking these small micropores. There is a secondary micropore specimen at around 1.5 nm which remains approximately the same for all the samples. Interestingly, the small mesopore peaks at around 3.6 nm increases slightly with the addition of the metal particles to the surface of the carbon. Also, the volumes of the other small mesopores are increased for the metal dispersed samples. It is possible that the impregnation method of dispersing the metal particles increases the volume of some mesopores.

The BET surface areas, total pore volumes, micropore volumes, mesopore volumes, and modal micropore and mesopore diameters are displayed in Table 4.2. The BET surface areas for the metal dispersed samples are all smaller than that of the PAC200 carbon (1037 m^2/g). This can be attributed to the blocking of micropores in the carbon by the metal nanoparticles and the heavier mass of the Pd, Cd, and Ag.[5,19] Consistent with the QSDFT pore size distributions, the micropore volumes decreases whereas the mesopore volumes increase when metal particles are dispersed onto the activated carbon. There is a slight inconsistency between the methods used to obtain the pore volumes since the mesopore volumes and micropore volumes add up to more than the total pore volumes. This is because there is an overlap in pore diameter measured. The Dubinin Astakhov (DA) method for micropore volume examines pores with a diameter between 0.2 Å and 60 Å and the Barret-Jayner-Halenda (BJH) method for mesopore volume examines pores with a diameter between 32.8 and 1895 Å. The modal micropore diameter obtained using the DA method is 1.5 nm for all the samples. The QSDFT method shows a modal micropore diameter of 0.96 nm. However, the second most predominant micropore diameter is 1.5 nm. The

modal mesopore diameter obtained using the BJH method varies from 3.60 to 3.65 nm which is consistant with the QSDFT method.

Table 4.2. Textural parameters of the activated carbon and metal dispersed activated carbon samples from N_2 adsorption/desorption isotherms at 77 K.

Sample	SA_{BET}[a] ($m^2 g^{-1}$)	V_t[b] ($cm^3 g^{-1}$)	$V_{micro, DA}$[c] ($cm^3 g^{-1}$)	$V_{meso, BJH}$[d] ($cm^3 g^{-1}$)	$D_{micro, DA}$[e] (nm)	$D_{meso, BJH}$[f] (nm)
PAC200	1037	0.6702	0.618	0.181	1.5	3.65
Pd/PAC200	920	0.5707	0.419	0.191	1.5	3.60
PdCd/PAC200	803	0.6288	0.520	0.201	1.5	3.61
PdAg/PAC200	933	0.6328	0.537	0.212	1.5	3.60

[a] The Brunauer- Emmet-Teller (BET) surface area (SA_{BET}) was obtained using 5 points within the relative pressure range of 0.1-0.3. [b] The total pore volume (V_t) was calculated at a relative pressure of 0.99. [c] The micropore volume ($V_{micro, DA}$) was obtained using the Dubinin Astakhov (DA) method of analysis. [d] The Barret-Jayner-Halenda (BJH) method was used to determine the volume of mesopores ($V_{meso, BJH}$) using the desorption branch and ignoring points below a relative pressure of 0.35. [e] The modal micropore diameter ($D_{micro, DA}$) was obtained using the Dubinin Astakhov (DA) method. [f] The modal mesopore diameter ($D_{meso, BJH}$) was obtained using the Barret-Jayner-Halenda (BJH) method.

4.4 Hydrogen Gas Adsorption at 77 K

It is well established and agreed in the current literature that high hydrogen adsorption capacity on carbon materials can only be achieved at low temperatures and/or high pressures.[20,21] In this study, we measured the hydrogen capacity of these carbon materials at low pressure (up to 1.01 bar) and at liquid nitrogen temperature (77 K). The hydrogen adsorption isotherms are displayed in Figure 4.4a. The maximum volumetric H_2 capacity achieved (at 1.01 bar) was converted to wt.% H_2 and plotted with respect to the BET surface area. As seen in Figure 4b, a linear trend was observed, indicating that hydrogen adsorption at 77 K is completely dependent on the overall surface area. This result is consistent with a recent report by van der Berg and Areán;[22] at low temperatures, the hydrogen molecules remain undissociated and are physically adsorbed to the surface of the carbon material with weak Van der Waals forces. As seen in
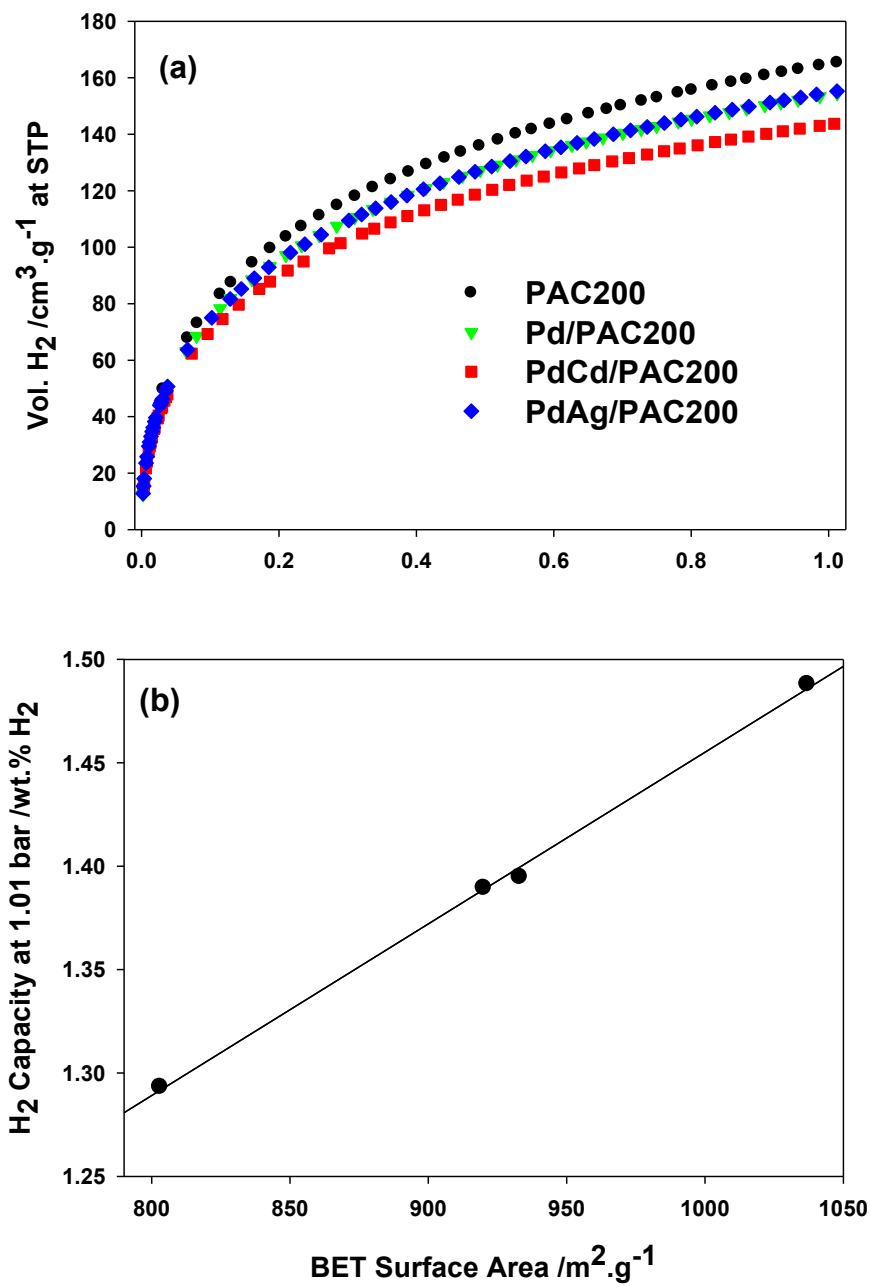
Figure 4.4. The hydrogen adsorption isotherms for the activated carbon and metal dispersed activated carbon samples at 77 K (a) and the relationship between the hydrogen adsorption capacity at 1.01 bar and the BET surface area of the carbon samples.

Figure 4.4b, the maximum hydrogen capacity is 1.49 wt.% H_2 for the commercially available PAC200 activated carbon at 1.01 bar at 77 K.

4.5 Hydrogen Spillover at Room Temperature

For practical application of carbon materials for hydrogen storage, it is necessary to increase the capacity at higher temperatures. Since physisorption is considered negligible at room temperature, this requires the dissociation of the H_2 molecule and chemisorption of H atoms. Unlike other hydrogen dissociation catalysts, Pd and Pd-based catalysts have the ability to absorb large volumetric quantities of hydrogen at room temperature.[13,14,23] Hydrogen absorption isotherms of unsupported Pd, PdCd, and PdAg nanoparticles at room temperature (295±2 K) are displayed in Figures 4.5. It can be seen from the absorption isotherms with the logarithmic pressure scale that the α/β phase transition is decreased and the maximum H/metal ratio is lower than that of pure Pd. These results are consistent with what was observed when hydrogen was electrosorbed into Pd and PdCd nanostructures in Chapter 3.[13] It appears that the PdCd and PdAg particles have very similar hydrogen absorption properties, which can be associated with the geometric dilation of the face-centered cubic lattice constant.[14]

In the absence of spillover hydrogen, at any given pressure, the volumetric capacity of the metal dispersed carbon materials can be calculated as a combination of the capacity of the metal particles and that of the PAC200 carbon according to:

$$V_{M/PAC200} = 0.05V_M + 0.95V_{PAC200} \qquad (4.1)$$

In this equation, $V_{M/PAC200}$ is the volumetric hydrogen capacity of a metal dispersed (5 wt.%) PAC200 material, V_M is the volumetric hydrogen capacity of a metal, and V_{PAC200} is the volumetric hydrogen capacity of the PAC200 carbon.
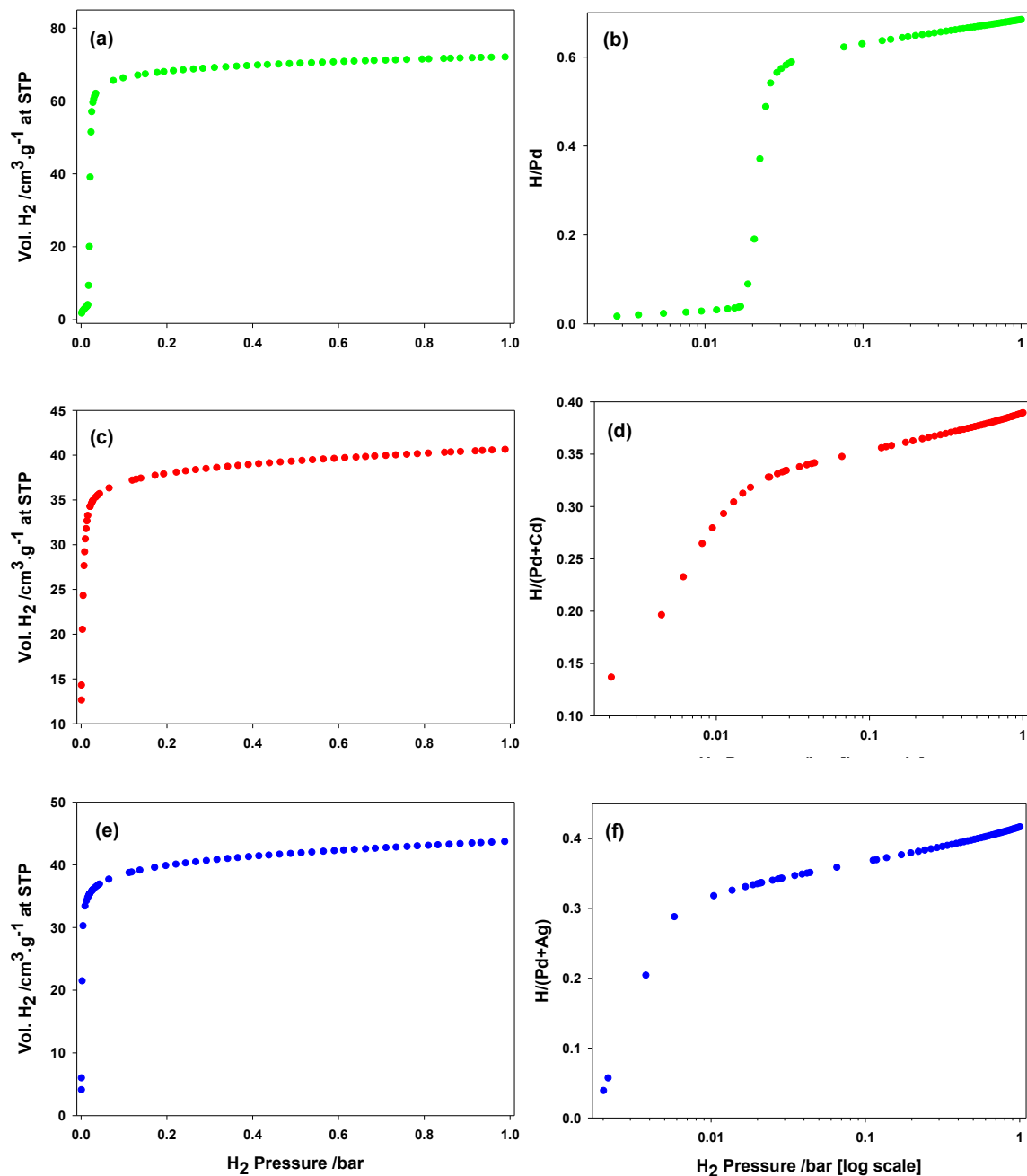
Figure 4.5. Hydrogen absorption isotherms at room temperature (295±2 K) for the prepared unsupported Pd (a, b), PdCd (c, d), and PdAg (e, f) nanoparticles. The isotherms on the left (a, c, e) display the volumetric hydrogen capacity with respect to H_2 pressure. The isotherms on the right (b, d, f) display the hydrogen-to-metal ratio with respect to a logarithmic H_2 pressure scale.

Hydrogen adsorption isotherms of the PAC200 and metal dispersed PAC200 samples at room temperature (295±2 K) are displayed in Figures 4.6. The volumetric capacity of the PAC200 is shown with black dots in Figure 4.6. The values of the term V_M were determined from the hydrogen absorption isotherms at room temperature for samples of unsupported Pd, PdCd, and PdAg nanoparticles with the same composition dispersed on the PAC200 carbon (Figure 4.5a, 4.5c, and 4.5e). The isotherms calculated using equation 4.1, with the assumption of no hydrogen spillover, are shown with crosses in Figure 4.6. It can be seen that there is minimal spillover effect from the Pd to the PAC200 substrate, whereas the effect is slightly enhanced for the PdAg particles. The enhancement due to spillover hydrogen from the PdCd particles is quite large. The above results indicate that the spillover effect is electronic in nature, rather than geometric. The maximum volumetric hydrogen capacities of the four samples are displayed in Table 4.3 along with the enhancement due to hydrogen spillover for the metal dispersed samples. The hydrogen spillover effect by the catalysts increases in the order of: Pd<PdAg<<PdCd.

Table 4.3. Hydrogen adsorption capacities at 1.01 bar and room temperature

Sample	Calculated H_2 Volumetric Capacity (cm^3g^{-1} at STP)	Actual H_2 Volumetric Capacity (cm^3g^{-1} at STP)	Enhancement by Hydrogen Spillover (%)
PAC200	1.20	1.20	0.000
Pd/PAC200	4.74	4.89	3.188
PdAg/PAC200	3.33	3.57	7.162
PdCd/PAC200	3.17	6.61	108.3

Although the hydrogen spillover mechanism is not fully understood, it has been thought that the rate limiting step in the process is the migration of dissociated hydrogen atoms from the metal catalyst to the carbon substrate.[3] This is due to the difference in adsorption strength of the
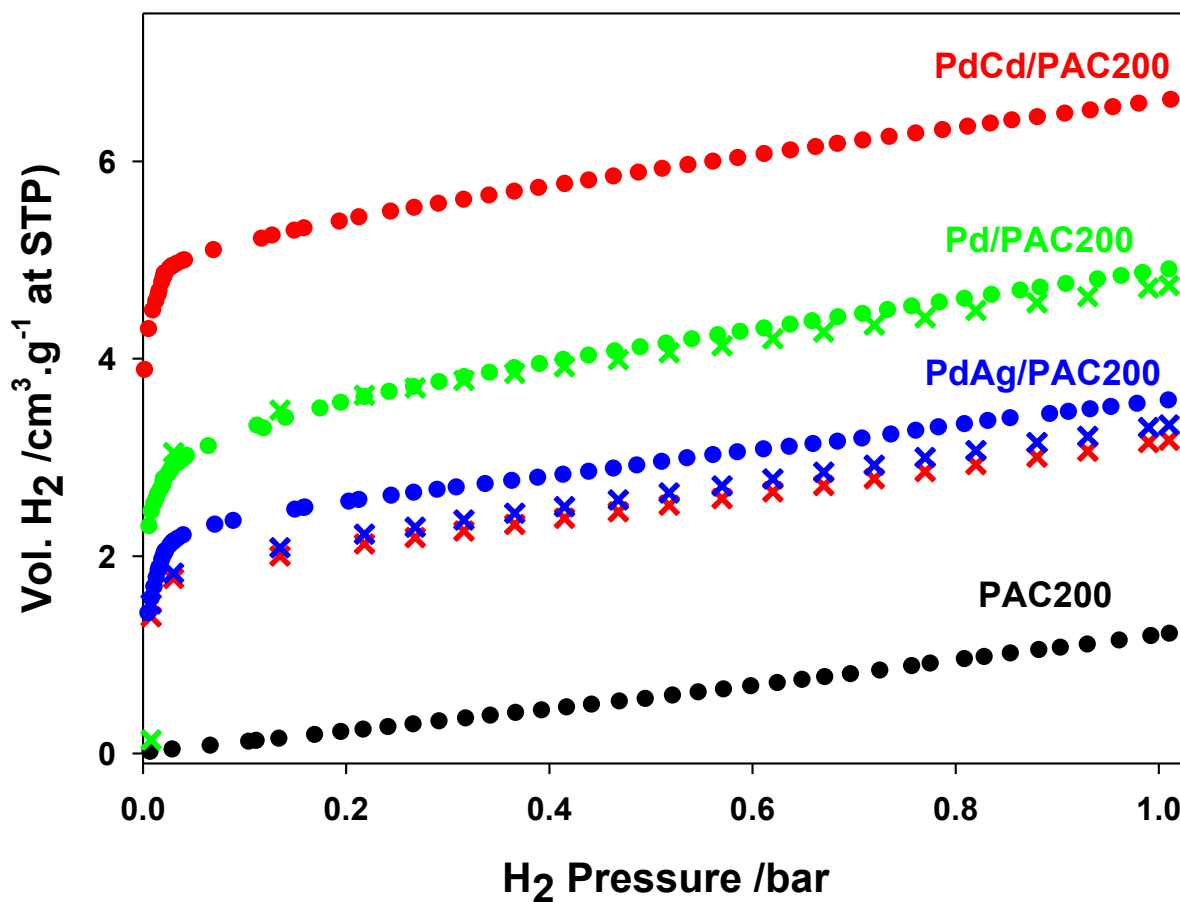
Figure 4.6. Hydrogen adsorption isotherms at room temperature (295±2 K) for the PAC200, Pd/PAC200, PdCd/PAC200, and PdAg/PAC200 samples. Hypothetical isotherms (calculated using Equation 4.2) are shown with crosses and experimentally observed isotherms are shown with dots.

hydrogen atom to the two different materials. The hydrogen atoms prefer to stay adhered to the surface metal atoms and, in order to migrate to the carbon material, an energy barrier must be overcome. To examine the adsorption strength of hydrogen atoms to the possible metal surface atoms in this study, a Density Functional Theory (DFT) method was used. All systems considered were fully optimized and characterized through harmonic frequency analysis. The total energy of Pd, Ag, Cd, and H atoms as well as Pd-H, Ag-H, and Cd-H molecules were calculated at various spin multiplicities. The lowest energy spins were used in calculating the adsorption energies according to the following equation:

$$E_{ads} = E_{M\text{-}H} - E_M - E_H \tag{4.2}$$

where $E_{M\text{-}H}$, E_M, and E_H are the total energies of the metal–hydrogen molecule, the metal atom, and a hydrogen atom, respectively. As the E_{ads} becomes more negative, the adsorption of H to the metal atom is favoured due to stabilization of the metal-H molecule. The Pd and Cd atoms as well as the Ag-H molecule were determined to be lowest in energy in the singlet state. The H and Ag atoms as well as the Pd-H and Cd-H atoms were lowest in energy as doublets.

^{2}SG
$d_{Pd\text{-}H} = 1.54$ Å
$E_{ads} = -59.19$ kcal/mol

^{1}SG
$d_{Ag\text{-}H} = 1.62$ Å
$E_{ads} = -54.50$ kcal/mol

^{2}SG
$d_{Cd\text{-}H} = 1.87$ Å
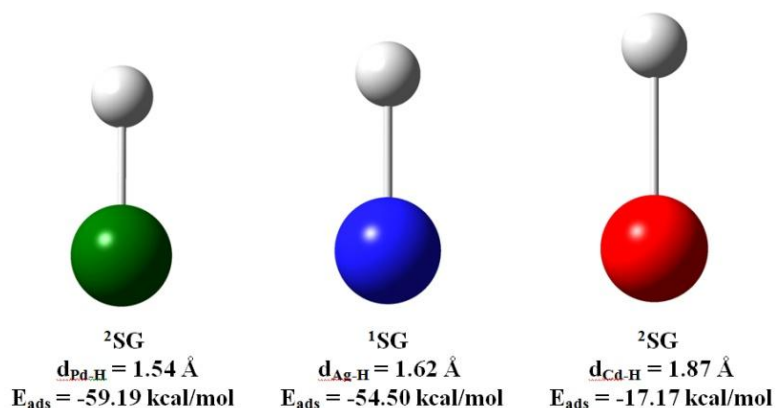$E_{ads} = -17.17$ kcal/mol

Figure 4.7. Optimized molecular geometries and adsorption energies for Pd-H, Ag-H, and Cd-H calculated using DFT. The H atoms are shown in white, Pd in green, Ag in blue, and Cd in red.

Shown in Figure 4.7 are the optimized molecular geometries of the M-H models and corresponding M-H bond distances and adsorption energies. The adsorption of hydrogen to a Pd atom is the strongest (E_{ads} = -59.19 kcal/mol) and the Pd-H bond distance is the shortest (1.54 Å). This is closely followed by Ag (E_{ads} = -54.50 kcal/mol), with an Ag-H bond distance of 1.62 Å. The adsorption strength of hydrogen to a Cd atom is much weaker (E_{ads} = -17.17 kcal/mol) and has a Cd-H bond distance of 1.87 Å. The migration of dissociated hydrogen atoms is thus less energetically demanding from surface Cd atoms than Pd (or Ag) atoms, resulting in a much higher hydrogen capacity of the PdCd/PAC200 material at room temperature.

4.6 Summary

In summary, three different hydrogen dissociation catalysts (Pd, PdAg, and PdCd) were dispersed onto surfaces of activated carbon; their effect on the hydrogen gas adsorption properties was systematically studied. The Pd, PdAg, and PdCd nanoparticles were dispersed onto the surface of the carbon using a facile room temperature reduction technique with sodium borohydride as the reducing agent. The coating load of the particles was 5 wt.% on the activated carbon in all cases, and the bulk composition of the particles was verified using ICP-AES to be Pd, $Pd_{0.85}Cd_{0.15}$, and $Pd_{0.77}Ag_{0.23}$. The surface compositions of the fabricated samples were analyzed using XPS and the pore sizes and BET specific surface areas were determined by N_2 adsorption/desorption isotherms at 77 K.

For hydrogen adsorption at 77 K, a linear trend was observed between the specific surface area of the samples and the maximum hydrogen capacity at 1.01 bar, showing that hydrogen adsorption at 77 K is completely dependent on the overall surface area. This proves that, at low temperatures, the hydrogen molecules remain undissociated and are physically adsorbed to the surface of the carbon material. Hydrogen spillover was observed for each of the

catalyst dispersed carbon samples at room temperature. It was found that the hydrogen spillover effect by the catalysts increased in the order of: Pd<PdAg<<PdCd. The PdCd catalyst had a hydrogen spillover enhancement of 108%. The nature of this hydrogen spillover enhancement was found to be electronic in nature rather than geometric. It was further verified using DFT calculations that the large hydrogen capacity of the PdCd/PAC200 sample is due to a weak adsorption strength of hydrogen atoms to surface Cd atoms, enabling energetically favourable migration of dissociated hydrogen atoms to the carbon substrate. In the past, the enhancement of hydrogen spillover to carbon materials has been mainly focused on modifying the carbon. The present study suggests that modification of the catalyst may be necessary to achieve large hydrogen adsorption capacities at room temperature on carbon materials via the hydrogen spillover mechanism.

References

1. F. Su, F. Y. Lee, L. Lv, J. Liu, X. N. Tian, X. S. Zhao, *Adv. Funct. Mater*. **2007**, *17*, 1926.

2. C. I. Contescu, C. M. Brown, Y. Liu, V. V. Bhat, N. C. Gallego, *J. Phys. Chem. C* **2009**, *113*, 5886.

3. G. M. Psofogiannakis, G. E. Froudakis, *J. Phys. Chem. C* **2009**, *113*, 14908.

4. L. Chen, A. C. Cooper, G. P. Pez, H. Cheng, *J. Phys. Chem. C* **2007**, *111*, 18995.

5. S.-W. Hwang, S.-U. Rather, M.-U.-D. Naik, C. S. Soo, K.-S. Nahm, *J. Alloy. Compd*. **2009**, *480*, L20.

6. G. M. Psofogiannakis, G. E. Froudakis, *J. Am. Chem. Soc*. **2009**, *131*, 15133.

7. C.-C. Huang, H.-M. Chen, C.-H. Chen, *Int. J. Hydrogen Energ*. **2010**, *35*, 2777.

8. Q. Li, A. D. Lueking, *Prepr. Pap.-Am. Chem. Soc., Div. Fuel Chem*. **2008**, *53*, 1.

9. J. Wang, F. H. Yang, R. T. Yang, M. A. Miller, *Ind. Eng. Chem. Res*. **2009**, *48*, 2920.

10. A. D. Lueking, R. T. Yang, *Appl. Catal A-Gen*. **2004**, *265*, 259.

11. F. H. Yang, A. J. Lachawiec, R. T. Yang, *J. Phys. Chem. B* **2006**, *110*, 6236.

12. M. Pozzo, D. Alfè, *Int. J. Hydrogen Energ*. **2009**, *34*, 1922.

13. B. D. Adams, C. K. Ostrom, A. Chen, *Langmuir,* **2010**, *26,* 7632.

14. B. Adams, G. Wu, S. Nigro, A. Chen, *J. Am. Chem. Soc.* **2009**, *131*, 6930.

15. S. Uemiya, T. Matsuda, E. Kikuchi, *J. Membr. Sci.* **1991**, *56*, 315.

16. A. Weiss, S. Ramaprabhu, N. Z. Rajalakshmi, *Phys. Chem.* **1997**, *199*, 165.

17. G. Yushin, R. Dash, J. Jagiello, J. E. Fischer, Y. Gogotsi, *Adv. Funct. Mater*. **2006**, *16*, 2288.

18. Y. X. Yang, R. K. Singh, P. A. Webley, *Adsorption* **2008**, *14*, 265.

19. L. Wang, F. H. Yang, R. T. Yang, *Ind. Eng. Chem. Res*. **2009**, *48*, 2920.

20. H. Wang, Q. Gao, J. Hu, *J. Am. Chem. Soc*. **2009**, *131*, 7016.

21. H. G. Schimmel, G. J. Kearley, M. G. Nijkamp, C. T. Visser, K. P. de Jong, F. M. Mulder, *Chem.-Eur. J.* **2003**, *9*, 4764.

22. A. W. C. van den Berg, C. O. Areán, *Chem. Commun*. **2008**, 668.

23. F. Berger, M. Varga, G. Mulas, Á. Molnár, I. Dékány, *Langmuir* **2003,** *19*, 3692.

Chapter 5

Electrochemical Reduction of Hydrogen Peroxide on Pd-Pt Catalysts

5.1 Introduction

The anode reaction of a fuel cell is either the direct oxidation of hydrogen[1] or another hydrogen containing fuel such as methanol,[2-5] ethanol,[6,7] formic acid,[7,8,9] or sodium borohyride.[10] The cathode reaction has typically always been the reduction of oxygen, either pure or from air.[1,11] Recently, attention has been directed towards the use of hydrogen peroxide as the oxidant in fuel cells. Hydrogen peroxide is a powerful oxidizer and its reduction takes place via a two-electron transfer.[12] This has a much lower activation barrier, and thus, much faster kinetics than the four-electron reduction of oxygen.[13]

Several types of fuel cells using hydrogen peroxide as the oxidant have already been tested, including metal semi-fuel cells (MSFCs),[14-18] direct borohydride fuel cells (DBFCs),[19-24] and direct formic acid fuel cells (DFAFCs).[25] Walsh et al.[19] tested a direct borohydride-acid peroxide fuel cell, but had challenges with the decomposition of hydrogen peroxide on the Pt/C cathode they used. Sahai et al.[23] tested direct borohydride fuel cells with both oxygen and hydrogen peroxide as oxidants, using Pt/C, and Pd/C as the cathodes, respectively. They found that by using hydrogen peroxide as the oxidant (on the Pd/C cathode) rather than oxygen (with the Pt/C cathode), the power density could be increased from 270 $mW.cm^{-2}$ to 665 $mW.cm^{-2}$.

The purpose of this study is to compare the activity of Pd to Pt as well as to PdPt bimetallic catalysts for hydrogen peroxide reduction in acidic media. While there have been many studies showing that PdPt catalysts demonstrate enhancement over both Pt and Pd for methanol oxidation,[26] hydrogen oxidation,[27] and oxygen reduction,[26,28,29] we know of no

previous examination of PdPt catalysts for hydrogen peroxide reduction. In this chapter, a treatment process for the carbon support material of these catalysts is discussed. The performance of these Pd, Pt, and PdPt catalysts towards hydrogen peroxide electroreduction with the use of a rotating disk electrode system is also examined.

5.2 Experimental Section

Commercially available carbon black, Vulcan XC72R (Cabot Corp.), was used as the support material in this study. To improve its hydrophillicity, the carbon black was first treated with 3 M HNO_3 for 1.5 hours. The carbon/HNO_3 slurry was then centrifuged and washed with pure water. Next, it was treated with a 3:1 ratio of 3.8 M H_2SO_4 and 7.5% H_2O_2 for 1.5 hours, centrifuged, and washed with water. After drying at 60 °C for 12 hours, the carbon was finally degassed under vacuum at 250 °C for 3 hours. This treated carbon was used as the support material for the Pt, Pd and PdPt nanoparticles.

The Pd-Pt catalysts were prepared using a room temperature impregnation method as described in Chapter 2. The metal precursors used were $PdCl_2$ (Alfa Aesar, 99.9%) and $H_2PtCl_6.6H_2O$ (Alfa Aesar, 99.9%). HCl (1wt%) was added to the $PdCl_2$ solution to aid in the solubility. The quantities of precursors and carbon used for each sample are displayed in Table 5.1. The coating load was 20 wt% metal in all cases.

Table 5.1. Reactant quantities for the preparation of the Pd, Pt, and PdPt catalysts.

Catalyst	Metal Precursors	Carbon	Input Composition
Pd	$PdCl_2$ (0.25 mmol)	106.42 mg	Pd/C
$Pd_{0.5}Pt_{0.5}$	$PdCl_2$ (0.125 mmol) $H_2PtCl_6.6H_2O$ (0.125 mmol)	150.74 mg	$Pd_{0.5}Pt_{0.5}$/C
$Pd_{0.25}Pt_{0.75}$	$PdCl_2$ (0.0835 mmol) $H_2PtCl_6.6H_2O$ (0.25 mmol)	230.64 mg	$Pd_{0.25}Pt_{0.75}$/C
Pt	$H_2PtCl_6.6H_2O$ (0.25 mmol)	195.08 mg	Pt/C

The synthesized Pd/C, Pt/C, and PdPt/C samples were characterized by TEM, EDS, XRD, and specific surface area analysis. The XRD patterns were obtained using a spinning stage on a PAN analytical X'Pert Pro MPD powder diffractometer with CuKα radiation at an accelerating voltage of 40 kV and a current of 30 mA. The specific surface areas of the samples were determined using a Quantachrome Nova 2200 surface area and pore size analyzer.

For the rotating disk electrode (RDE) experiments, a catalyst ink was applied to a glassy carbon RDE (Pine Instruments Co., 0.196 cm^2). First, 4 mg of catalyst was added to 4 mL of 40 wt.% isopropanol. The solution was sonicated for one hour. Next, 15 µL of Nafion® perfluorinated ion exchange resin (10 wt.% dispersion in water) was added and the solution was sonicated again for 30 minutes. Coating of the RDE was done immediately using 10 µL aliquots a total of 8 times, drying each coat under argon at room temperature, for a total coating load of 81.3 µg metal/cm^2.

The RDE experiments were performed in a three-electrode cell setup consisting of the catalyst-coated glassy carbon RDE as the working electrode, a Pt wire (10 cm^2) as the counter electrode, and an Ag/AgCl reference electrode. The supporting electrolyte used was 0.1 M HClO$_4$ in all cases. The solution was deoxygenated by bubbling argon through it for 15 minutes prior to the experiments. Cyclic voltammetry was then performed for 50 cycles within the range of -200 mV to 1000 mV to clean the RDE surface of impurities. The hydrogen peroxide (30%, Sigma-Aldrich) was added to the electrolyte immediately after the cyclic voltammetric studies such that the concentration of H$_2$O$_2$ was 0.03 M and argon was again bubbled through the solution for 5 minutes to ensure proper mixing. Argon was continuously passed above the solution during the RDE studies. For all linear sweep voltammetric studies and chronoamperometric studies, the rotation speed of the RDE was adjusted using a modulated

speed rotator from Pine Instruments. All potentials reported herein are with respect to the Ag/AgCl reference electrode used in these studies (0.199 V vs. SHE).

5.3 Treatment of Carbon Black

The Vulcan XC72R carbon black was chosen as a support material since it is possibly the most commonly used carbon support material for platinum-based and palladium-based electrocatalysts.[30-33] Although carbon is an excellent electronic conductor, it is a very poor proton conductor, mainly because of its hydrophobicity.[34] Surface hydrophilic groups such as phenoxy, carbonyl, carboxyl, quinine, and lactone can be introduced by acid treatment or chemical oxidation methods.[34,35] Nafion, a proton conducting polymer, is commonly used as a glue to adhere carbon-supported catalysts to a substrate. This can also be used to increase the hydrophillicity. However, when too much Nafion is used, catalytic activity is decreased,[36] due to blocking of active sites by the polymer. Here we used a combination of HNO_3, H_2SO_4, and H_2O_2 as oxidizing agents in order to create a hydrophilic surface appropriate for electrochemical reactions while keeping the Nafion loading quite low. Displayed in Figure 5.1 is a comparison of the hydrophobicity of the untreated (Figure 5.1a) and the treated (Figure 5.1b) carbon after a coating (with no metal catalyst) was applied to the RDE using Nafion as described in Section 5.2. The untreated Vulcan XC72R carbon black is hydrophobic whereas the treated carbon is hydrophilic even though only a very small amount of Nafion was used.

5.4 Surface Analysis of Pd/C, Pt/C and PdPt/C Catalysts

Shown in Figure 5.2 are typical TEM images of the catalysts. All of the particles appear to be less than 5 nm in diameter. The pure Pt particles are the most uniform and evenly distributed, whereas the pure Pd particles are more agglomerated. This is characteristic of the
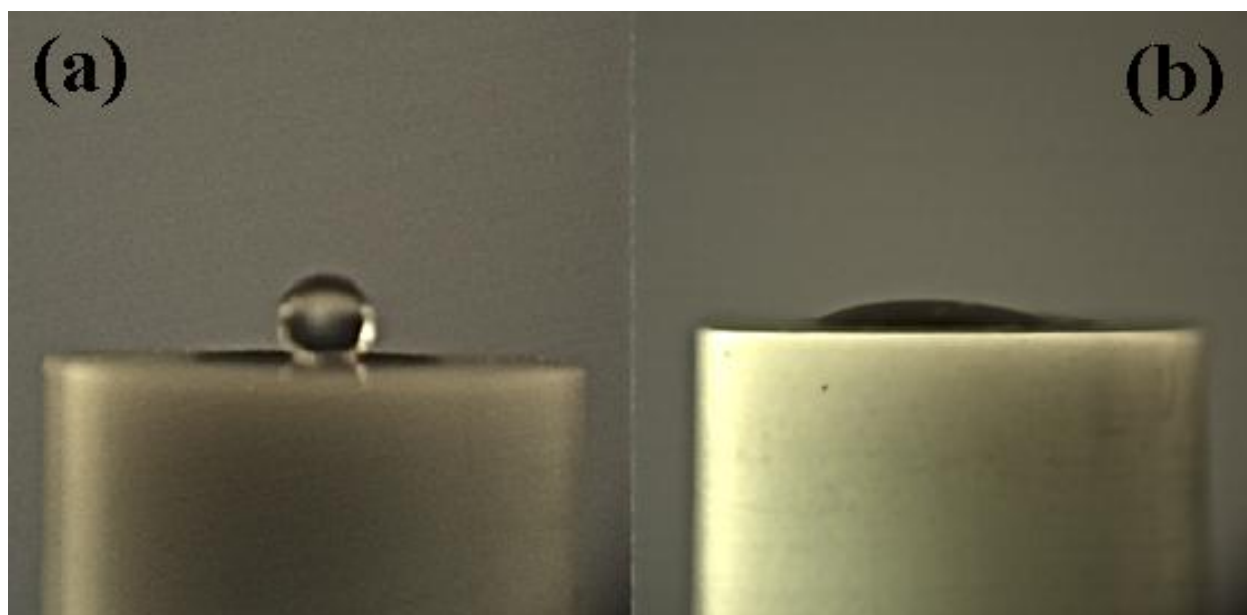
Figure 5.1. Optical images showing the water contact angle (hydrophobicity) for a rotating disk electrode coated with untreated Vulcan XC72 carbon black (a) and treated Vulcan XC72 carbon black.
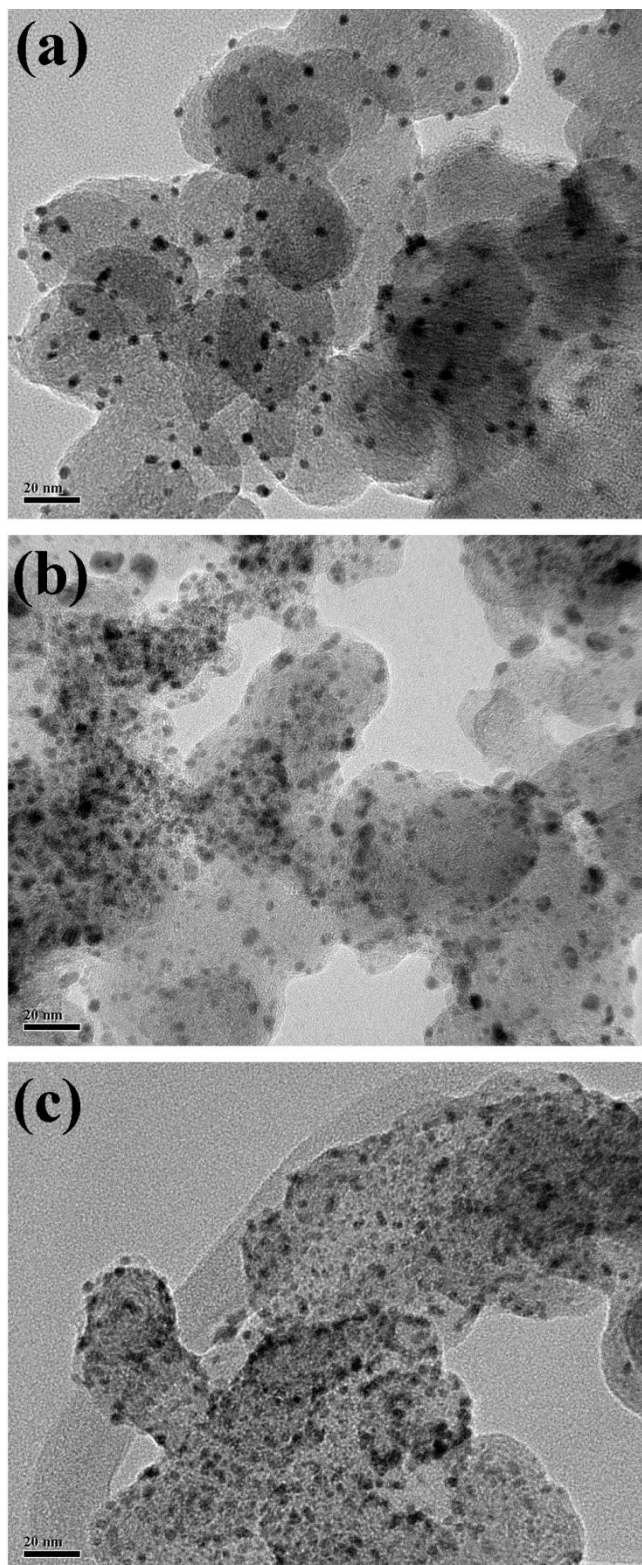
Figure 5.2. Typical TEM images of the prepared carbon-supported catalysts. (a) Pt/C, (b) Pd/C, and (c) $Pd_{0.25}Pt_{0.75}$/C.

two metals, and it is known to be a major challenge to create nanosized Pd particles without the formation of aggregates.

The composition of the catalysts was verified using EDS. Shown in Figure 5.3, are the EDS spectra of the prepared catalysts for the Pt and Pd region. For pure Pd, the main peaks appear at 2.77 and 2.92 keV. For the Pt/C sample, the two Pt peaks are centred at 2.00 and 2.27 keV. For the $Pd_{0.5}Pt_{0.5}$ and $Pd_{0.25}Pt_{0.75}$ catalysts, both these sets of peaks can be seen. Although not shown here, for all the catalysts, a large carbon peak was also observed at 0.25 keV due to the support material as well as a very small oxygen peak was observed at 0.5 keV due to the oxidation treatment of the carbon.

X-ray diffraction was carried out to examine the crystal structure of the catalysts (Figure 5.4). All of the catalysts exhibit the 002 peak of the carbon support material, as well as the face-centered cubic structure of Pd and/or Pt. The broad shape of the diffraction signals is due to small particle size.

Table 5.2 displays the BET surface areas and average particle sizes calculated from the 220 peak of the XRD patterns according to the Scherrer equation:[37]

$$L = \frac{0.94\lambda}{\beta \cos \theta} \tag{5.1}$$

where L is the average crystallite size, 0.94 is a constant for small spherical particles of similar size and distribution, λ is the wavelength of X-ray radiation (Cu Kα = 0.15405 nm), β is the full-width at half maximum (FWHM) in radians, and θ is the location of the (220) peak.

Table 5.2. Average particle size calculated from XRD and BET surface area of catalysts.

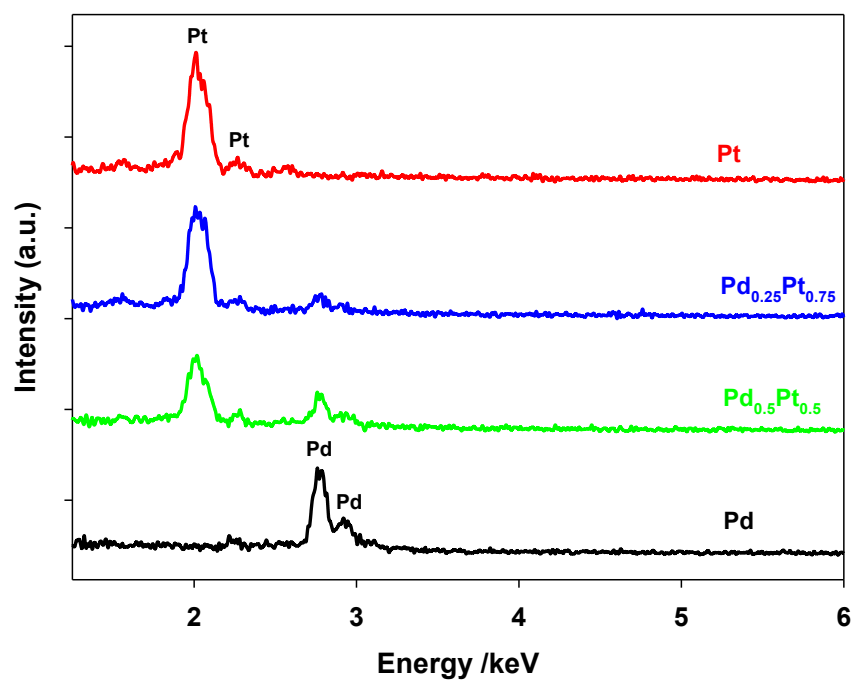| Catalyst	Average Particle Size (nm)	BET Surface Area (m^2/g)
Pd	3.95	183
$Pd_{0.5}Pt_{0.5}$	3.85	186
$Pd_{0.25}Pt_{0.75}$	3.76	182
Pt	4.90	184

Figure 5.3. EDX spectra of the prepared catalysts for the region for Pt and Pd.

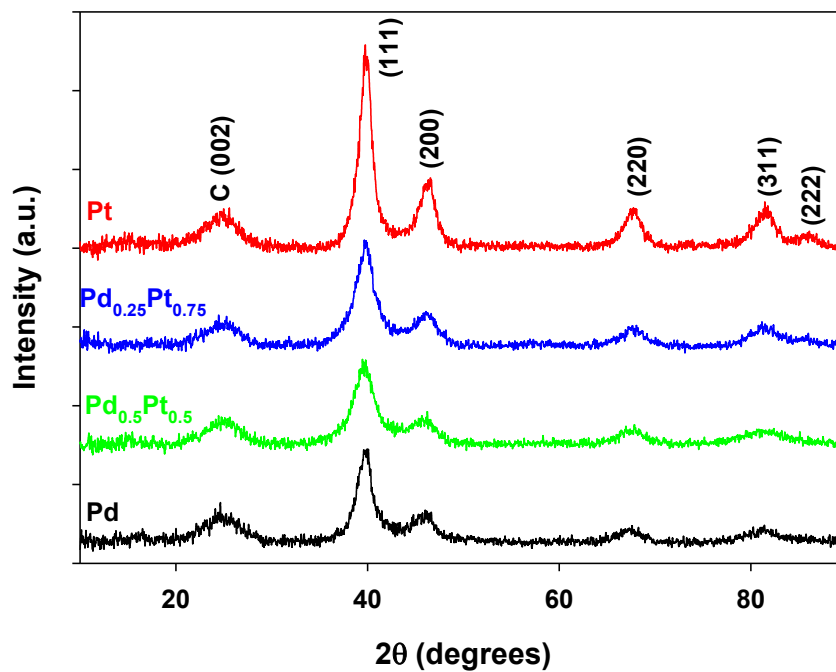**Figure 5.4.** X-ray diffraction patterns of the prepared catalysts.

The BET surface areas are all less than that of the Vulcan XC72R carbon (239 m^2/g) which can be attributed to blocking of certain pores in the carbon by the metal nanoparticles and the heavier mass of the Pd and Pt.[38,39] It was found that the initial surface treatment of the Vulcan XC72R had little effect on the BET surface area (231 m^2/g after treatment). The average particle sizes as estimated from the XRD patterns are consistent with the TEM images (Figure 5.2).

5.5 Electrochemical Reduction of H_2O_2 with Pd/C, Pt/C and PdPt/C Catalysts

Cyclic voltammograms of the four catalysts recorded at a scan rate of 20 mV/s in 0.1 M $HClO_4$ are displayed in Figure 5.5. These were obtained after cycling the potential several times at 50 mV/s to clean the surface of impurities. These voltammograms are typical of carbon-supported Pt and Pd catalysts in an acidic medium. The hydrogen adsorption/desorption peaks are present at -200 to approximately 100 mV and the double-layer region occurs between 100 and 200 mV. Surface oxidation begins at around 200 mV for the Pt, $Pd_{0.5}Pt_{0.5}$, and $Pd_{0.25}Pt_{0.75}$ catalysts. However, for the Pd catalyst, it does not occur until around 400 mV. The onset of oxide reduction for the Pt, $Pd_{0.5}Pt_{0.5}$, and $Pd_{0.25}Pt_{0.75}$ catalysts also occurs at more positive potentials than on the Pd catalysts. The peak current of the oxide reduction is the greatest for the Pd and $Pd_{0.5}Pt_{0.5}$ catalysts.

Rotating disk experiments were perfomed using linear sweep voltammetry (LSV) and chronoamperometry in the presence of 0.03 M H_2O_2. This low concentration of H_2O_2 was used to avoid spontaneous decomposition of H_2O_2 (to O_2 and H_2O) as reported by others.[8,9] Figure 5.6 displays the LSVs at a rotation speed of 1000 rpm. From this set of experiments, the general hydrogen peroxide reduction behaviour of each of the catalysts was inspected. From Figure 5.6a, the onset potential for hydrogen peroxide electroreduction was the greatest for the Pt catalyst and the lowest for the Pd catalyst. As shown in Table 5.3, the onset potentials for the $Pd_{0.5}Pt_{0.5}$ and
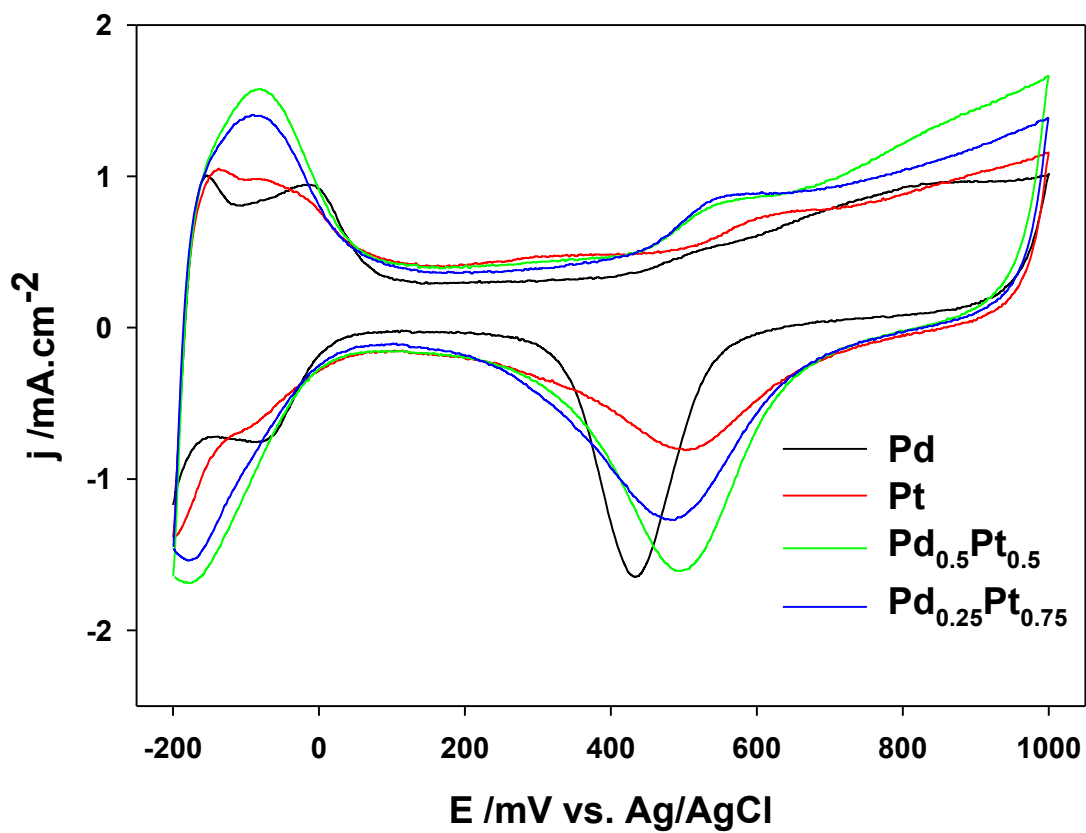
82

Figure 5.5. Cyclic voltammograms of the glassy carbon RDE coated with the catalyst inks in 0.1 M HClO$_4$ at a scan rate of 20 mV/s.

$Pd_{0.25}Pt_{0.75}$ catalysts were practically identical and fell directly between Pd and Pt. Although the Pd had a lower onset potential than the Pt, its limiting current density was higher. The limiting current densities of the two PdPt catalysts were greater than both the Pd and Pt catalysts, with the $Pd_{0.25}Pt_{0.75}$ being the highest. The shapes of the LSVs vary slightly between each of the catalysts. For Pd, the electroreduction of hydrogen peroxide appears to occur in two steps as seen by the presence of an initial small reduction peak at approximately 475 mV, whereas the others all have a similar wave-like shape. Figure 5.6b shows the LSV for the $Pd_{0.25}Pt_{0.75}$ RDE in 0.1 M $HClO_4$ with and without 0.03 M H_2O_2 added as a reference. It is clear that the current densities observed are due to the reduction of hydrogen peroxide and not to the perchloric acid electrolyte (oxide reduction or hydrogen desorption).

Table 5.3. Onset potentials E_i measured at -0.05 mA and reduction current densities j_c at -200 mV.

Catalyst	E_i (mV)	j_c (mA)
Pd	543.9	-29.0
$Pd_{0.5}Pt_{0.5}$	559.7	-31.2
$Pd_{0.25}Pt_{0.75}$	557.9	-36.1
Pt	593.9	-23.9

To further compare the performance of the four catalysts, chronoamperometry was performed, again at 1000 rpm. The potential was first held at 650 mV, which was higher than the onset potential for the electroreduction of hydrogen peroxide on any of the catalysts. Then, it was stepped down to a potential at which the electroreduction of hydrogen peroxide occurs and held for 5 minutes. The current densites at 400 mV, 200 mV, 0 mV, and -200 mV were examined. At higher potentials (Figures 5.7a and 5.7b), the current density of Pd was the lowest, and reached steady-state very quickly. The Pt had the second lowest current density, followed by $Pd_{0.5}Pt_{0.5}$, and the highest current density was exhibited by the $Pd_{0.25}Pt_{0.75}$ electrode. At lower potentials
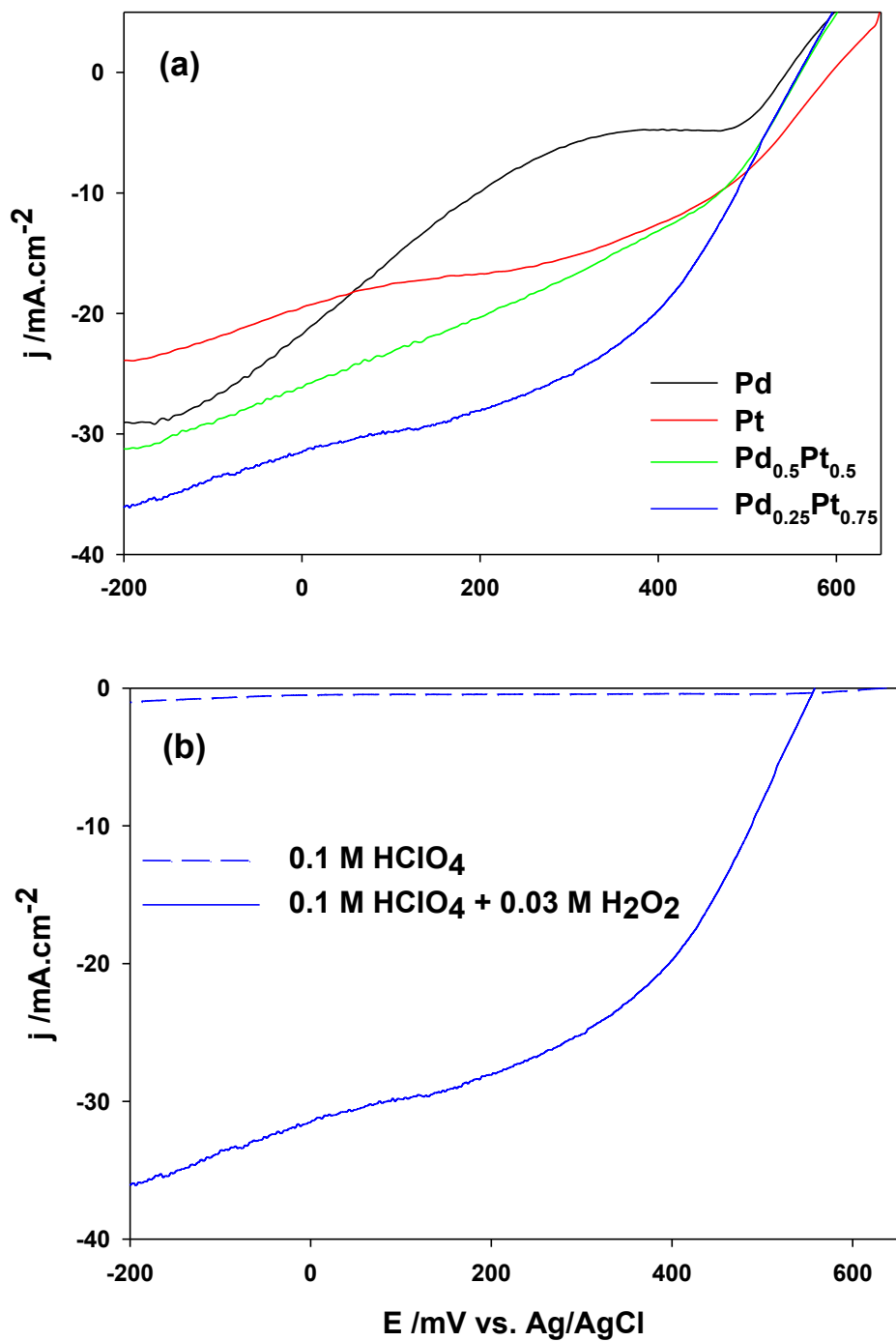
Figure 5.6. Linear sweep voltammograms in 0.1 M $HClO_4$ + 0.03 M H_2O_2 for the catalysts at 1000 rpm and a scan rate of 10 mV/s (a) and a comparison of linear sweep voltammograms for $Pd_{0.25}Pt_{0.75}$ with and without H_2O_2 present (b).
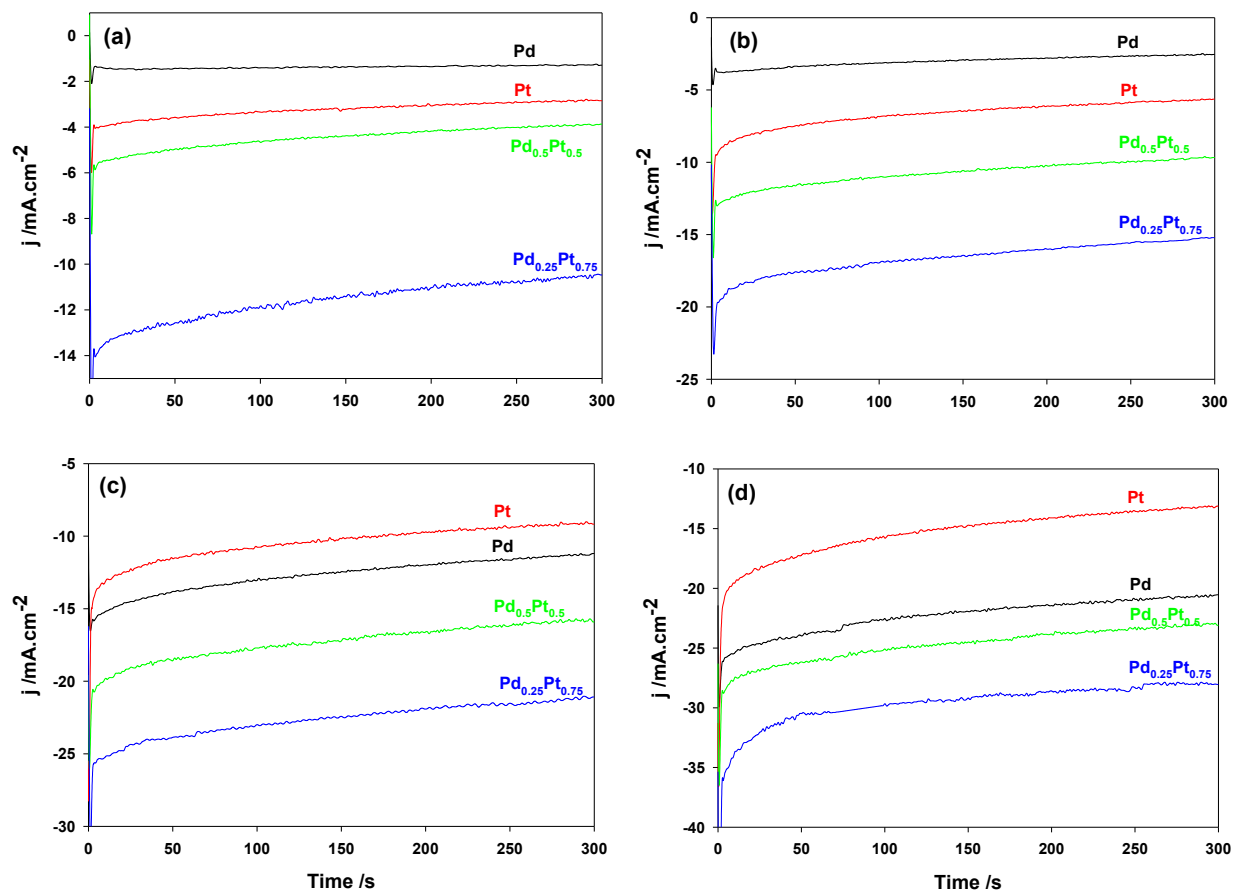
Figure 5.7. Chronoamperometric curves of the prepared catalysts at 1000 rpm after holding the potential at 650 mV for 30 seconds and stepping the potential down to 400 mV (a), 200 mV (b), 0 mV (c), and -200 mV (d).

(Figures 5.7c and 5.7d), the trend was different. The current densities increased in the following order: $Pt < Pd < Pd_{0.5}Pt_{0.5} < Pd_{0.25}Pt_{0.75}$. In all cases, as the potential decreased, the reduction current density was greater for each electrode. The $Pd_{0.25}Pt_{0.75}$ catalyst outperformed the others at every potential in terms of steady-state current density.

5.6 Summary

In this study, Pd/C, Pt/C, and PdPt/C catalysts were fabricated and tested for their activity towards the electrochemical reduction of H_2O_2 in acidic conditions. The Vulcan XC72R carbon black support was treated with HNO_3, H_2SO_4, and H_2O_2, to increase the hydrophillicity of the catalysts. The surface of the catalysts were analyzed with TEM, EDS, XRD, and BET. It was found that the Pd and Pt particles were well dispersed on the surface of the carbon black, with a well defined particle size range below 5 nm. The $Pd_{0.5}Pt_{0.5}$ and $Pd_{0.25}Pt_{0.75}$ catalysts both outperformed the Pt and Pd catalysts, with the $Pd_{0.25}Pt_{0.75}$ having the highest activity for hydrogen peroxide reduction.

References

1. C.V. Rao, B. Viswanathan, *J. Phys. Chem. C* **2010**, 114, 8661.

2. T.-Y. Jeon, K.-S. Lee, S.J. Yoo, Y.-H. Cho, S.H. Kang, Y.-E. Sung, *Langmuir* **2010**, 26, 9123.

3. K. Koczkur, Q. Yi, A. Chen, *Adv. Mater.* **2007**, *19* 2648.

4. G. Wu, B. Adams, M. Tian, A. Chen, *Electrochem. Commun.* **2009**, *11*, 736.

5. J. Wang, P. Holt-Hindle, D. MacDonald, D. F. Thomas, A. Chen, *Electrochim. Acta* **2008**, *53*, 6944.

6. A.A. El-Shafei, M. Eiswirth, *Surf. Sci.* **2010**, *604*, 862.

7. A. Ghumman, G. Li, D.V. Bennett, P.G. Pickup, *J. Power Sources* **2009**, *194*, 286.

8. H. Meng, S. Sun, J.-P. Masse, J.-P. Dodelet, *Chem. Mater.* **2008**, *20*, 6998.

9. J. Wang, R.M. Asmussen, B. Adams, D.F. Thomas, A. Chen, *Chem. Mater.* **2009**, *21*, 1716.

10. D.M.F. Santos, C.A.C. Sequeira, *J. Electrochem. Soc.* **2010**, *157*, F16.

11. Y. Shao, S. Zhang, C. Wang, Z. Nie, J. Liu, Y. Wang, Y. Lin, *J. Power Sources* **2010**, *195*, 4600.

12. L. Sun, D. Cao, G. Wang, *J. Appl. Electrochem.* **2008**, *38*, 1415.

13. D. Cao, L. Sun, G. Wang, Y. Lv, M. Zhang, *J. Electroanal. Chem.* **2008**, *621*, 31.

14. M.G. Medeiros, R.R. Bessette, C.M. Deschenes, C.J. Patrissi, L.G. Carreiro, S.P. Tucker, D.W. Atwater, *J. Power Sources* **2004**, *136*, 226.

15. W. Yang, S. Yang, W. Sun, G. Sun, Q. Xin, *Electrochim. Acta* **2006**, *52*, 9.

16. R.R. Bessette, J.M. Cichon, D.W. Dischert, E.G. Dow, *J. Power Sources* **1999**, *80*, 248.

17. R.R. Bessette, M.G. Medeiros, C.J. Patrissi, C.M. Deschenes, N.N. LaFratta, *J. Power Sources* **2001**, *96*, 240.

18. W. Yang, S. Yang, W. Sun, G. Sun, Q. Xin, *J. Power Sources* **2006**, *160*, 1420.

19. C. Ponce de León, F.C. Walsh, A. Rose, J.B. Lakeman, D.J. Browning, R.W. Reeve, *J. Power Sources* **2007**, *164*, 441.

20. N.A. Choudhury, R.K. Raman, S. Sampath, A.K. Shukla, *J. Power Sources* **2005**, *143*, 1.

21. N. Luo, G.H. Miley, K.-J. Kim, R. Burton, X. Huang, *J. Power Sources* **2008**, *185*, 685.

22. G. Selvarani, S.K. Prashant, A.K. Sahu, P. Sridhar, S. Pitchumani, A.K. Shukla, *J. Power Sources* **2008**, *178*, 86.

23. J. Ma, Y. Sahai, R.G. Buchheit, *J. Power Sources* **2010**, *195*, 4709.

24. R.K. Raman, S.K. Prashant, A.K. Shukla, *J. Power Sources* **2006**, *162*, 1073.

25. E. Kjeang, A.G. Brolo, D.A. Harrington, N. Djilali, D. Sinton, *J. Electrochem. Soc.* **2007**, *154*, B1220.

26. Y. Xu, X. Lin, *J. Power Sources* **2007**, *170*, 13.

27. S.J. Yoo, H.-Y. Park, T.-Y. Jeon, I.-S. Park, Y.-H. Cho, Y.-E. Sung, *Angew. Chem. Int. Ed.* **2008**, *47*, 9307.

28. X.-M. Miao, R. Yuan, Y.-Q. Chai, Y.-T. Shi, Y.-Y. Yuan, *J. Electroanal. Chem.* **2008**, *612*, 157.

29. B. Lim, M. Jiang, P.H.C. Camargo, E.C. Cho, J. Tao, X. Lu, Y. Zhu, Y. Xia, *Science* **2009**, *324*, 1302.

30. Z. Zhou, S. Wang, W. Zhou, L. Jiang, G. Wang, G. Sun,B. Zhou, Q. Xin, *Phys. Chem. Chem. Phys.* **2003**, *5*, 5485.

31. L. Zhang, T. Lu, J. Bao, Y. Tang, C. Li, *Electrochem. Commun.* **2006**, *8*, 1625.

32. A. Sarkar, A. Vadivel Murugan, A. Manthiram, *J. Phys. Chem. C* **2008**, *112*, 12037.

33. X. Yu, P.G. Pickup, *Int. J. Green Energy* **2009**, *6*, 571.

34. N. Lakshmi, N. Rajalakshmi, K.S. Dhathathreyan, *J. Phys. D: Appl. Phys.* **2006**, *39*, 2785.

35. W. Shen, Z. Li, Y. Liu, *Rec. Pat. Chem. Eng.* **2008**, *1*, 27.

36. J.M. Sieben, M.M.E. Duarte, C.E. Mayer, *Int. J. Hydrogen Energ.* **2010**, *35*, 2018.

37. T. Maiyalagan, K. Scott, *J. Power Sources* **2010**, *195*, 5246.

38. S.-W. Hwang, S.-u. Rather, M.-u.-d. Naik, C.S. Soo, K.-S. Nahm, *J. Alloy. Compd.* **2009**, *480*, L20.

39. L. Wang, F.H. Yang, R.T. Yang, *Ind. Eng. Chem. Res.* **2009**, *48*, 2920.

Chapter 6

CO Adsorption on Pd-based Nanomaterials

6.1 Introduction

Carbon monoxide adsorption on metallic nanoparticles has been extensively investigated due to its importance in the water-gas shift reaction, emission control, and fuel cell reactions.[1] In the case of fuel cells, CO is generated in the process of electro-catalytic oxidation of formic acid and other small organic compounds (often via dissociative chemisorption) and it causes substantial poisoning of the active sites on precious metal catalysts.[2] Likewise, if hydrogen gas is used as a fuel, the presence of CO at trace levels (>10 ppm) as an impurity resulting from the production of H_2 by steam reforming of methane also gives rise to catalyst poisoning and performance degradation.[3]

When metals are combined in an appropriate manner, the chemisorption of CO can be tuned and controlled. As catalyst design becomes more involved, alloying of various compounds becomes an attractive method to control the reaction pathway. In order to properly design catalysts, it is important to have an understanding of the interaction between the catalyst and the chemisorbed reactant or intermediate species. CO poisoning of alloyed PtRu and PtPb catalysts is diminished compared to pure Pt.[4,5] PtRu is possibly the most commonly studied anode catalyst material for direct methanol fuel cells.[6,7] It has been proposed that the enhanced activity of PtRu towards methanol oxidation compared to Pt arises from ruthenium's ability to generate oxygen-containing species on the catalyst surface to easily oxidize the poison CO species.[8-10] In the case of PtPb, CO adsorption is avoided or very weak due to modification of the catalyst crystal

structure. This alters the reaction mechanism for formic acid oxidation, greatly enhancing its performance.[4,11]

In the past few decades, Pd-based materials have been studied rigorously in order to improve and extend their environmental applications for the elimination of contaminants related with automobile exhaust pipe gases like CO, NO_x and SO_x,[12] and are viewed as the most promising alternative to Pt-based catalysts at one-fifth of the cost.[13,14] For example, Pd has been shown to possess superior performance as anodes for the oxidation of formic acid compared to Pt-based catalysts.[15,16] Despite the promising properties of Pd-based catalysts, not nearly as much research has gone into studying them compared to Pt-based material. The aim of this study is to use standard computational techniques to examine the adsorption of CO on small Pd-containing metal clusters, with attempts to expand the research involving Pd-based catalytic materials.

There is an ongoing debate regarding the type of model to use for simulations of adsorption on catalytic surfaces. Periodic boundary conditions can be used to reproduce extended surfaces.[17-19] In this method one defines a unit cell which is then used to expand the cell in x, y, and/or z directions, thus providing the electronic structure for linear, slab (surface), and bulk materials, respectively.[20] Alternatively, in the cluster approach, a discrete number of atoms are used to represent the active site region. The basic premise is that chemisorption and reactivity are local phenomena, primarily affected only by the nearby surface structure.[20-22] The properties of nanostructured materials are known to differ greatly from extended single crystalline surfaces. Several studies have shown that models based on clusters containing a very small number of atoms can obtain results for local phenomena such as CO stretches and bond distances closer to experiment than slab models for nanosized particles.[23,24] Bertin et al. compared CO adsorption

on Pd nanosized clusters with n > 50 atoms to their work of n = 2, 4 and found that Pd$_4$ clusters give results close to experimental work with nanoparticles.[12]

In many studies, the adsorption energy of carbon monoxide on certain transition metals is compared.[25,26] To the best of our knowledge, never before has an extensive comparison been made of the CO adsorption on the entire series of transition metals. This could give insight to new combinations of metals for catalysts involving CO as a reactant or intermediate. In this study, the CO adsorption energy is studied on single metal atoms for all of the transition metals using density functional theory (DFT). Also, CO adsorption on Pd$_4$, Pd$_2$Au$_2$, and Pd$_2$Pt$_2$ clusters is calculated and compared with results from the electrochemical oxidation of adsorbed CO on Pd, PdAu, PdPt nanostructures and C-O stretch frequency analysis of CO-adsorbed nanostructures by *in situ* attenuated total reflection-Fourier transform infrared spectroscopy (ATR-FTIR).[11,27]

6.2 Experimental Section

Density functional theory (DFT) calculations were carried out as described in Chapter 2. It is well known that CO can bond to a metal surface in three possible ways (on-top, bridging, and hollow sites) as displayed in Figure 6.1.
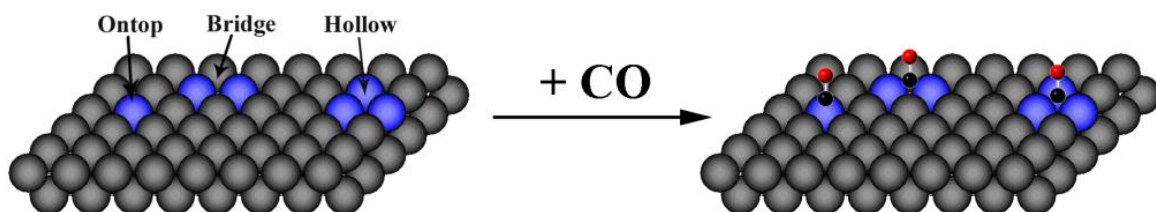

Figure 6.1. Possible adsorption sites for CO to a metal surface.

By using four-atom metal clusters all of these bonding positions can be examined with minimal computational demands.[25] Various spin multiplicities were examined for the individual metal atoms and the metal-CO clusters. The lowest energy spins were used in calculating the adsorption energies according to the following equation:

$$E_{ads} = E_{cluster-CO} - E_{cluster} - E_{CO} \tag{6.1}$$

where $E_{cluster-CO}$, $E_{cluster}$, and E_{CO} are the total energies of the metal–carbonyl cluster, the metal cluster, and molecular CO, respectively. From this equation, as the E_{ads} becomes more negative, the adsorption of CO to the metal cluster is favoured. While basis set superposition errors (BSSE) were not considered, our results are extremely close to experimentally determined CO adsorption energies (see Section 6.3).[25]

The nanostructured catalysts were fabricated using the hydrothermal reduction of Pd, Au, and Pt precursors as described in Chapter 2. Ammonium formate was used as the reducing agent and the metal precursors were $PdCl_2$, $HAuCl_4 \cdot xH_2O$, and $H_2PtCl_6 \cdot 6H_2O$. In all cases, the total amount of inorganic precursor and reducing agent added were kept constant at 5 mM and 1M, respectively. Pure water was used as the solvent in all cases, with a dilute HCl solution used to aid in the solubility of $PdCl_2$. For the Pd catalyst, only $PdCl_2$ was added to the vessel, whereas for the PdAu and PdPt catalysts, stoichiometric amounts of the $PdCl_2$, $HAuCl_4 \cdot xH_2O$, and $H_2PtCl_6 \cdot 6H_2O$ precursors were added to obtain the desired composition of Pd:Au and Pd:Pt of 50:50 as displayed in Table 6.1.

Table 6.1. ICP-AES results for the final concentration of solution after hydrothermal reduction of metal salts.

Compostion	Initial Concentration[a] (ppm/mM)	Final Concentration[b] (ppm/mM)	Actual Composition[c]
Pd	Pd: 532.10/5	Pd: 0.0550/5.17x10^{-4}	Pd
Pd$_{0.5}$Au$_{0.5}$	Pd: 266.05/2.5 Au: 492.43/2.5	Pd: 0.1939/1.82x10^{-3} Au: 0.0136/6.90x10^{-5}	Pd$_{0.5}$Au$_{0.5}$
Pd$_{0.5}$Pt$_{0.5}$	Pd: 266.05/2.5 Pt: 487.70/2.5	Pd: 0.0298/2.80x10^{-4} Pt: 0.0178/9.12x10^{-5}	Pd$_{0.5}$Pt$_{0.5}$

[a] The concentration of precursors added to the reaction vessel prior to the reductions. [b] Concentrations of metals remaining in solution after the hydrothermal reductions determined by ICP-AES. [c] Actual composition of nanostructures determined by subtracting the final solution concentrations from the initial concentrations.

The electrochemical performance of the electrodes towards the oxidation of surface adsorbed carbon monoxide was characterized using cyclic voltammetry (CV). For this, a three-electrode cell system was used as described in Chapter 2. The reference electrode was a saturated calomel electrode connected to the cell through a salt bridge, thus all potentials mentioned herein are with respect to the SCE (0.244 V vs. SHE). The working electrodes used were the prepared Ti/Pd, Ti/PdAu, and Ti/PdPt plates (1 cm^2). The coated Ti plates were annealed at 250 °C for 2 h in a tube furnace under argon to ensure a good surface adhesion of the particles. These plates were then soldered to Ti wire leads for use as working electrodes. The electrolyte for these CV studies was 0.5 M H$_2$SO$_4$, and the solution was deaerated with ultrapure argon gas prior to measurements to remove any dissolved oxygen. Argon gas was continually passed over the solution throughout the experimentation. Data acquisition and analysis were performed using VoltMaster 4 software. Carbon monoxide was used for the CO-stripping study. Before scanning the applied potential, the working electrode was held at −0.1 V for 360 s while a stream of pure CO was bubbled into the solution during the first 180 s. Then the solution was purged with pure Ar for the remaining 3-min holding period. Immediately following the electrode pretreatment,

two cycles of CV were recorded for each electrode. The ATR-FTIR experiments were carried out as described in Chapter 2.

6.3 CO Adsorption onto Single Metal Atoms

Calculations were run first on both the metal atoms and CO in various spin states to determine the lowest energy spin. As expected, CO is most stable in the singlet state and the ground state spin multiplicity for the metal atoms varies depending on the electron configuration. For the metal-CO molecules (M-CO), an initial linear structure ($C_{\infty v}$) was considered and fully optimized, again assessing various spin states. The adsorption energies for the most stable species were calculated as described in Section 6.2 and are reported in Table 6.2 along with the corresponding structural parameters, M-C, M-C-O, and C-O frequencies. It can be seen that all of the metal carbonyl molecules are linear, except for Cr-CO, Mn-CO, and those involving to group 11 and 12 metals. In general, the smallest adsorption energies are for those which do not possess a linear geometry. As expected, the platinum group metals have the largest CO adsorption energies. Consistent with another DFT study,[25] iridium exhibits the largest adsorption energy and is closely followed by platinum. CO stretching frequencies range from 1918 cm^{-1} (Y-CO) to 2212 cm^{-1} (Hg-CO).

There does not seem to be a good linear relationship between adsorption energy and either the bond lengths or the vibrational frequencies over the complete set of transition metals.[25,28] On the other hand, a link between the accepted number of d electrons (d^{n}) on the metal and the M-C bond distances as well as the CO stretching frequencies can be seen in Figure 6.2a and Figure 6.2b. The principle quantum number has little effect on either the CO stretching frequencies or the M-C bond distances. The classical model for CO chemisorbed onto metals is

Table 6.2. The adsorption energies, structural parameters, and harmonic frequencies for single metal atoms bonded to CO.

	Molecule	Spin	E_{ads} (kcal/mol)	M-C Bond Length (Å)	C-O Bond Length (Å)	M-C-O Angle (°)	v MC (cm^{-1})	v MCO (cm^{-1})	v CO (cm^{-1})
	ScCO	Quartet	-17.98	2.105	1.168	180.0	397	260	1968
	TiCO	Quintet	-27.22	2.052	1.161	180.0	394	257	2011
	VCO	Sextet	-21.70	2.001	1.157	180.0	394	248	2031
	CrCO	Quintet	4.64	2.081	1.151	161.6	292	235	1987
3d	MnCO	Sextet	9.57	2.044	1.157	172.7	342	54	2060
	FeCO	Triplet	-24.76	1.771	1.157	180.0	437	293	2051
	CoCO	Doublet	-22.68	1.703	1.159	180.0	482	335	2025
	NiCO	Singlet	-30.12	1.669	1.160	180.0	597	347	2098
	CuCO	Doublet	-9.05	1.999	1.151	137.2	316	205	2056
	ZnCO	Singlet	1.05	3.866	1.138	117.0	19	48	2209
	YCO	Quartet	-17.50	2.231	1.174	180.0	367	282	1918
	ZrCO	Quintet	-36.17	2.152	1.167	180.0	387	289	1970
	NbCO	Sextet	-35.59	2.088	1.160	180.0	407	300	2017
	MoCO	Quintet	-36.11	1.948	1.171	180.0	479	349[a] 329	1977
4d	TcCO	Quartet	-46.10	1.841	1.174	180.0	557	390	1988
	RuCO	Triplet	-50.45	1.827	1.167	180.0	534	364	2031
	RhCO	Doublet	-46.20	1.819	1.161	180.0	508	333	2063
	PdCO	Singlet	-42.97	1.867	1.151	180.0	456	250	2127
	AgCO	Doublet	-1.17	2.517	1.143	127.5	82	187	2130
	CdCO	Singlet	1.12	4.026	1.138	122.7	19	47	2209
	LaCO	Quartet	-24.45	2.437	1.167	180.0	306	263	1951
	HfCO	Triplet	-33.72	2.076	1.170	180.0	401	313	1950
	TaCO	Quartet	-29.26	2.028	1.163	180.0	422	322	2002
	WCO	Quintet	-27.10	1.918	1.178	180.0	509	379	1940
5d	ReCO	Doublet	-15.43	1.818	1.176	180.0	599	439	1994
	OsCO	Triplet	-52.89	1.795	1.168	180.0	618	449	2055
	IrCO	Doublet	-69.30	1.777	1.162	180.0	622	438	2100
	PtCO	Singlet	-67.76	1.781	1.156	180.0	589	402	2132
	AuCO	Doublet	-7.96	2.080	1.148	139.2	330	205	2086
	HgCO	Singlet	1.07	4.061	1.137	140.5	7	45	2212

[a] Renner-Teller splitting, two π-type frequencies 349 and 329 cm^{-1}

the Blyholder model,[29] where there is a combination of σ donation from the carbon atom's highest occupied molecular orbital (HOMO) to the metal's lowest unoccupied molecular orbital (LUMO) as well as π back-donation from a metal HOMO to the antibonding $2\pi^*$ LUMO orbital of the CO. This model fits well with our calculations. As the d orbitals become more filled at a given quantum number, the M-C bond distance decreases slightly for d^1 to d^8 metals, and then greatly increases from d^8 to d^{10} (Figure 6.2a). From d^1 to d^8, the metals can accept donation from the 5σ orbital (HOMO) of CO and there is an increasing amount of donation from the
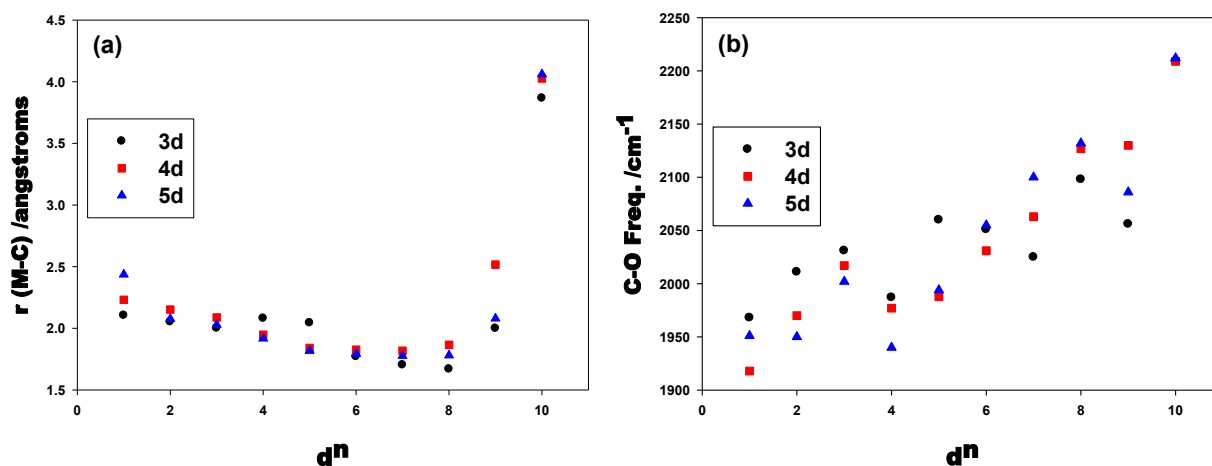
Figure 6.2. The metal-carbon bond distance (a) and vibrational CO stretching frequencies (b) versus the number of d electrons of the metal for all of the transition metal-carbonyl clusters of the form M-CO. The 3d, 4d, and 5d metals are represented by black circles, red squares, and blue triangles, respectively.
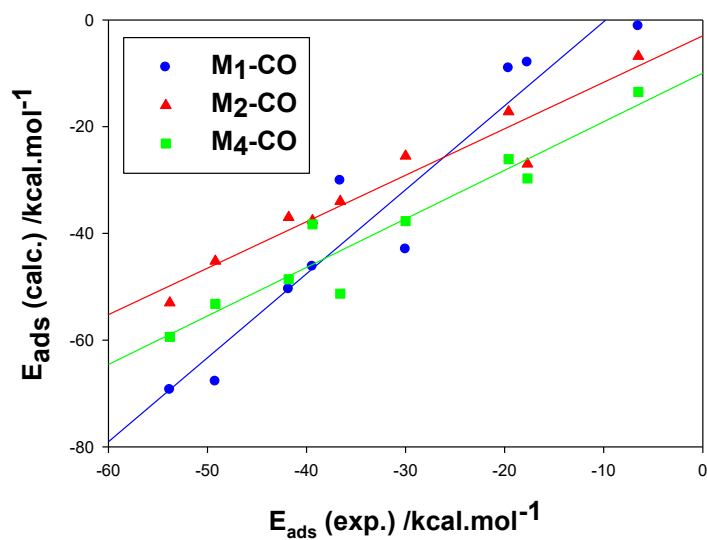

Figure 6.3. Comparison of adsorption energies of our M-CO clusters with an M_2-CO cluster model, an M_4-CO cluster model, and experimental values taken from Ref. 17 and references therein. The metals compared were Ni, Cu, Ru, Rh, Pd, Ag, Ir, Pt, and Au.

metal's HOMO to the CO's LUMO. This binding combination strengthens the metal-carbon bond. When the d orbitals of the metals become full, from d^8 to d^{10}, there is no more contribution of σ donation to the metal LUMO, which causes a very sharp increase in the M-C bond distance. Similarly, the ν(CO) increases with an increasing number of d electrons of the metals (Figure 6.2b), due to the effect of progressively less σ donation from the CO HOMO to the metal LUMO.

Shown in Figure 6.3 is a comparison of selected calculated M_1-CO adsorption energies from this study with experimental work by others and larger M_2-CO and M_4-CO clusters studied by Zeinalipour-Yazdi et al.[25] It can be seen that while this work varies slightly from the experimental values, the same general trend can be observed for the chosen metals studied by Zeinalipour-Yazdi et al. Thus, although CO bonded to single metal atoms does not give realistic values of CO adsorption energies, this method can be used to compare the metal-CO bond strength between different elements and screen their usability as catalyst components. To examine the effect of CO adsorption on combined metals, Pd was chosen because it is a commonly used catalyst for CO oxidation and fuel cell reactions. We then chose a metal with a stronger affinity for CO and a metal with a much weaker CO bond to combine with Pd to assess the preferential binding sites of CO to these bimetallic clusters. Pt (E_{ads} = -67.76 kcal/mol) and Au (E_{ads} = -7.96 kcal/mol) were chosen since these metals are possibly the most widely studied as catalysts on the nanoscale.[4,27,30-32]

6.4 CO Adsorption onto a Pd$_4$ Cluster

A Pd$_4$ cluster was optimized (Figure 6.4a) starting from high T_d symmetry using the DFT method described above, considering both low and high spin cases. The known ground state triplet spin of this cluster was reproduced[12,33] possessing C_S symmetry. It is well known that CO
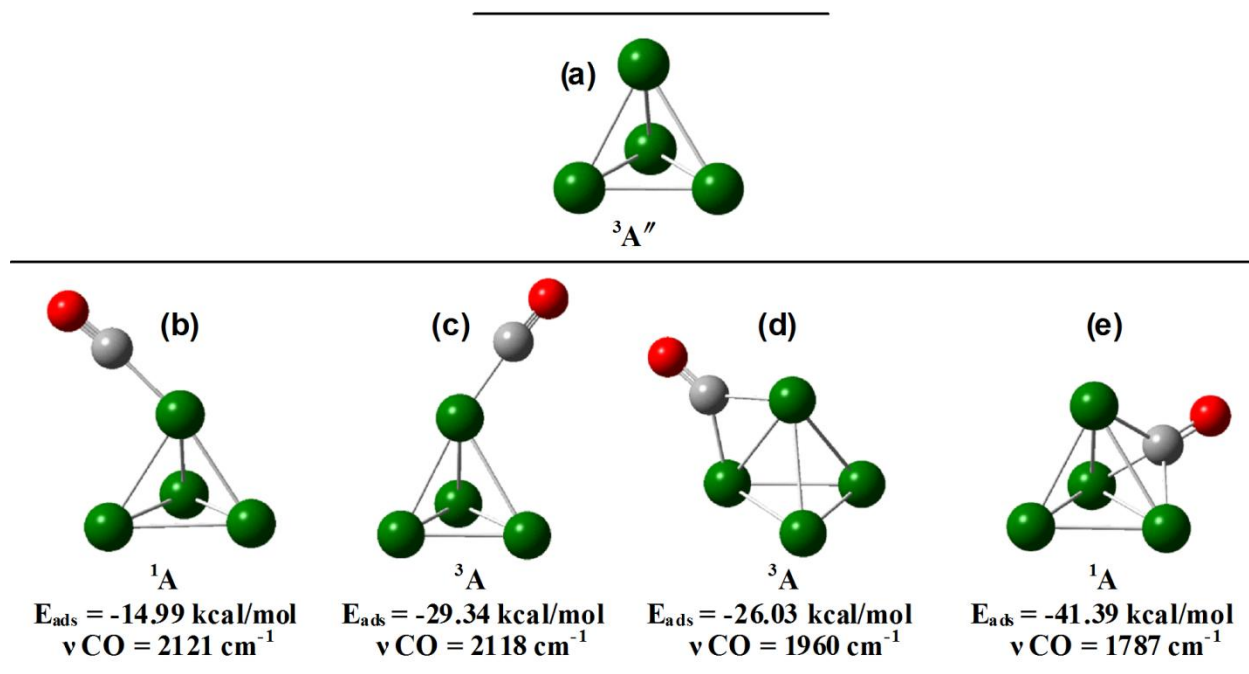
Figure 6.4. Optimized structures of the Pd$_4$ clusters: (a) initially (triplet) and with (b) CO on-top (singlet), (c) CO on-top (triplet), (d) CO bridged (triplet), and (e) CO in a hollow position (singlet). Palladium, carbon, and oxygen are shown in green, grey, and red, respectively.

can bind to a Pd surface via the carbon atom in three ways: on-top of a single Pd atom; bridged between two Pd atoms; or in a hollow three-fold position (Figure 6.1). Each of these binding sites were examined in both singlet and triplet spin states. Figure 6.4b-e present the optimized Pd_4-CO clusters for each of the CO bonding modes in both the singlet and triplet states. With CO on-top a Pd atom, complete optimization could be obtained in both the singlet state (Figure 6.4b) and triplet state (Figure 6.4c). With CO initially bridging two Pd atoms in the singlet state, the structure was optimized to the hollow site binding motif (Figure 6.4e). The optimization of CO initially bound to three Pd atoms in the triplet state led to the bridging motif (Figure 6.4d). The adsorption energies for the two on-top spin cases are quite different (-14.99 kcal/mol for the singlet state vs. -29.34 kcal/mol for the triplet state), yet the CO stretching frequencies are close (2121 cm^{-1} for the singlet state vs. 2118 cm^{-1} for the triplet state). This is because only the electronic state of the Pd cluster changed; the CO retained the singlet configuration in both cases. Similarly, the CO adsorption strength for the on-top sites differ greatly between the four atom Pd cluster and the single Pd atom studied in section 6.3. However, the CO stretching frequencies compare favourably. The variance of adsorption energy between cluster sizes is in part due to the fact that the adsorption energy is a property that reflects the characteristics of metal surfaces in a global fashion, whereas the CO stretch is a very local phenomenon.[23] For the on-top binding site, Zeinalipour-Yazdi et al.[25] report a bond dissociation energy of 37.7 kcal/mol for their Pd_4-CO cluster without correcting for BSSE. Their BSSE corrected bond dissociation energy at the corresponding BSSE corrected minimum is 30.8 kcal/mol, which compares quite well with an experimental thermal decomposition spectroscopic value of 30.0 kcal/mol.[34] Our corresponding calculation for CO bonded to the Pd_4 cluster on-top a single Pd atom gives a bond dissociation energy of 29.34 kcal/mol which is extremely close to experiment even without BSSE correction.

This is possibly due to the use of an all-electron basis set for describing CO. Using the four atom cluster model here, the hollow site attachment has the strongest CO adsorption strength, followed by the on-top site and, lastly, the bridged site.

6.5 CO Adsorption onto a Pd$_2$Pt$_2$ Cluster

In order to examine the effect of a metal with greater adsorption strength for CO than Pd, a Pd$_2$Pt$_2$ cluster was modeled. As found in section 6.3, the adsorption energy for CO on-top a single Pd atom is -42.97 kcal/mol, whereas for CO on-top a Pt atom, the value is -67.76 kcal/mol. The optimized molecular structure of the Pd$_2$Pt$_2$ cluster is displayed in Figure 6.5a. It was found that the lowest energy Pd$_2$Pt$_2$ cluster was in the triplet state and the initial C$_{2V}$ symmetry was maintained. Again, CO binding to on-top, bridging, and hollow site positions were explored. For this cluster, more sites were possible because of the combination of Pd and Pt atoms. All of these optimized Pd$_2$Pt$_2$-CO clusters are displayed in Figure 6.5b-n. For CO bridging two Pd atoms, the singlet state possesses a more energetically favourable planar structure (Figure 6.5f) which is unique compared to all the other tetrahedral-like cluster geometries. Similar to the Pd$_4$-CO system, CO bound in a hollow site between one Pt atom and two Pd atoms optimized to a CO bridging a Pt atom and a Pd atom (Figure 6.5k). The strongest adsorption site for CO is ontop a Pt atom, with an E$_{ads}$ of -36.91 kcal/mol in the singlet state and -44.83 kcal/mol in the triplet state. The next favoured site is CO bridging two Pt atoms with an E$_{ads}$ of -33.85 kcal/mol in the singlet state. The same binding motif in the triplet state has a much weaker CO interaction (E$_{ads}$ = -19.35 kcal/mol). The large differences in E$_{ads}$ emphasizes the importance of considering various spin multiplicities when performing DFT calculations on these small metal clusters. Other sites, such as on-top a Pd atom and three-fold PtPtPd still had large adsorption energies, indicating strong interaction between CO and these sites as well.

Figure 6.5. Optimized structures of the Pd_2Pt_2 clusters: (a) initially (triplet) and with (b) CO on-top Pd (singlet), (c) CO on-top Pd (triplet), (d) CO on-top Pt (singlet), and (e) CO on-top Pt (triplet), (f) CO bridging PdPd (singlet), (g) CO bridging PdPd (triplet), (h) CO bridging PtPt (singlet), (i) CO bridging PtPt (triplet), (j) CO bridging PdPt (singlet), (k) CO bridging PdPt (triplet), (l) CO in a hollow PdPdPt position (singlet), (m) CO in a hollow PtPtPd position (singlet), and (n) CO in a hollow PtPtPd position (triplet). Palladium, platinum, carbon, and oxygen are shown in green, blue, grey, and red, respectively.

6.6 CO Adsorption onto a Pd$_2$Au$_2$ Cluster

The opposite effect of the Pd$_2$Pt$_2$ cluster was examined by modelling a Pd$_2$Au$_2$ cluster. As found in section 6.3, Au has a much lower affinity for CO than Pd (-7.96 kcal/mol for Au-CO vs. -42.97 kcal/mol for Pd-CO). The optimized molecular structure of the Pd$_2$Au$_2$ cluster is displayed in Figure 6.6a. For both the Pd$_4$ and Pd$_2$Pt$_2$ clusters, the lowest energy spin state was a triplet, whereas for this cluster it is a singlet with C$_{2V}$ symmetry. The following adsorption sites were considered: CO on-top a single Pd atom; CO on-top a single Au atom; CO bridging two Pd atoms, CO bridging two Au atoms; CO bridging one Pd atom and one Au atom; CO in a three-fold Pd-Pd-Au hollow site; and CO in a three-fold Au-Au-Pd hollow site. Interestingly, only the first three were obtained (Figure 6.6b-h), with CO bonded on-top a single Pd atom possessing the strongest adsorption energy (Figure 6.6b). When attempting a bridged Pd-Au position, a bridge Au-Au position, and a Pd-Au-Au threefold position, the result was CO bonded on-top a single Pd atom. In the triplet state, a more energetically favoured planar structure was located (Figure 6.6d). In the singlet state, the CO arranged itself in this position as well when initially bound to a hollow Pd-Pd-Au position, however in the triplet state, the CO preferred to be bridged between two Pd atoms. In all cases, the addition of Au to Pd completely hindered CO adsorption to hollow sites.

6.7 Electrochemical CO Stripping from Pd, PdPt and PdAu

Because CO is strongly adsorbed to platinum group metals, it is a major poisoning species for many catalysts in the process of the oxidation of small organic molecules. Therefore, one of the most important merits of an effective catalyst is its efficient removal of surface adsorbed CO.[18] To compare the performance of the as-synthesized Pd, PdAu, and PdPt
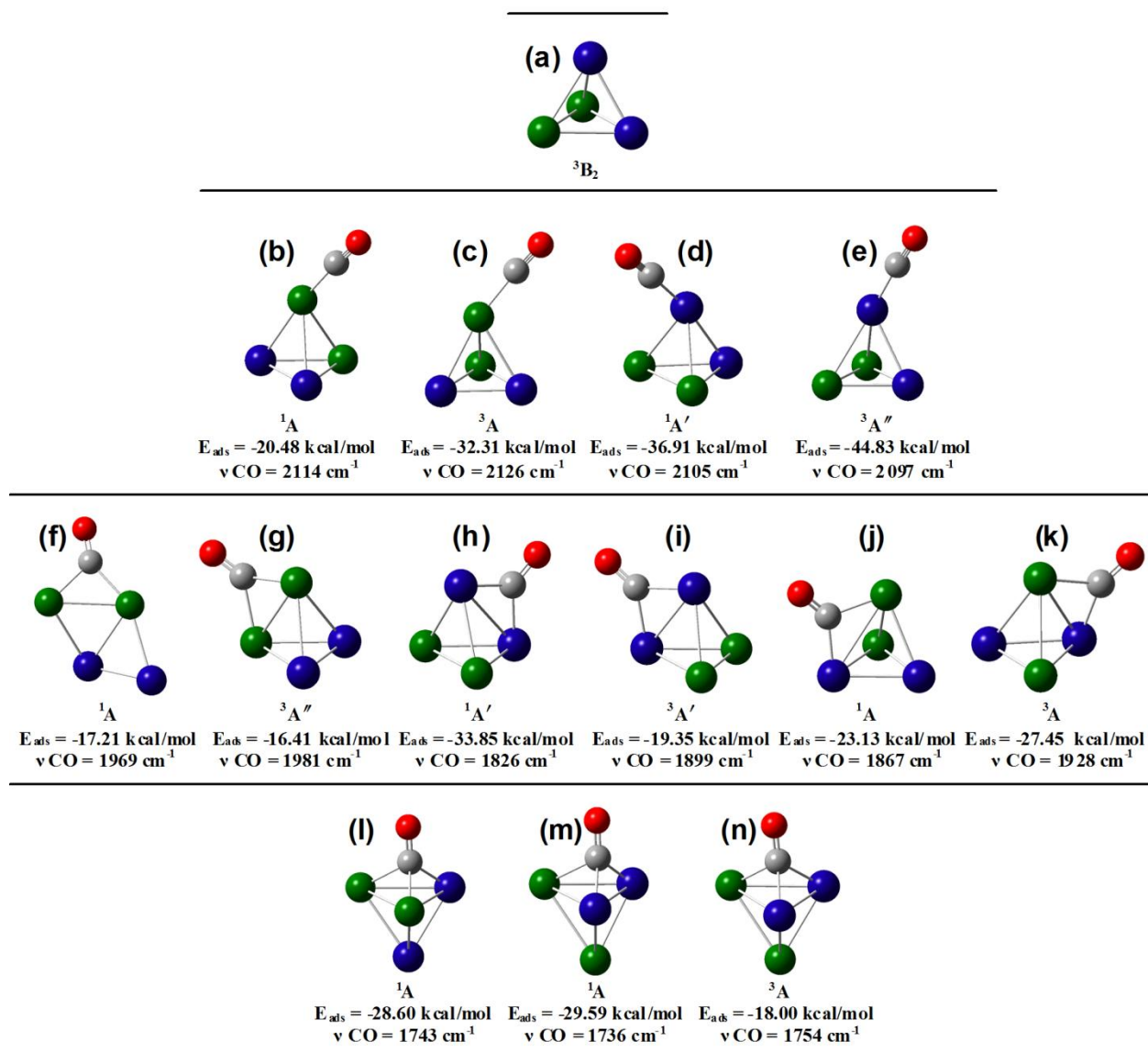
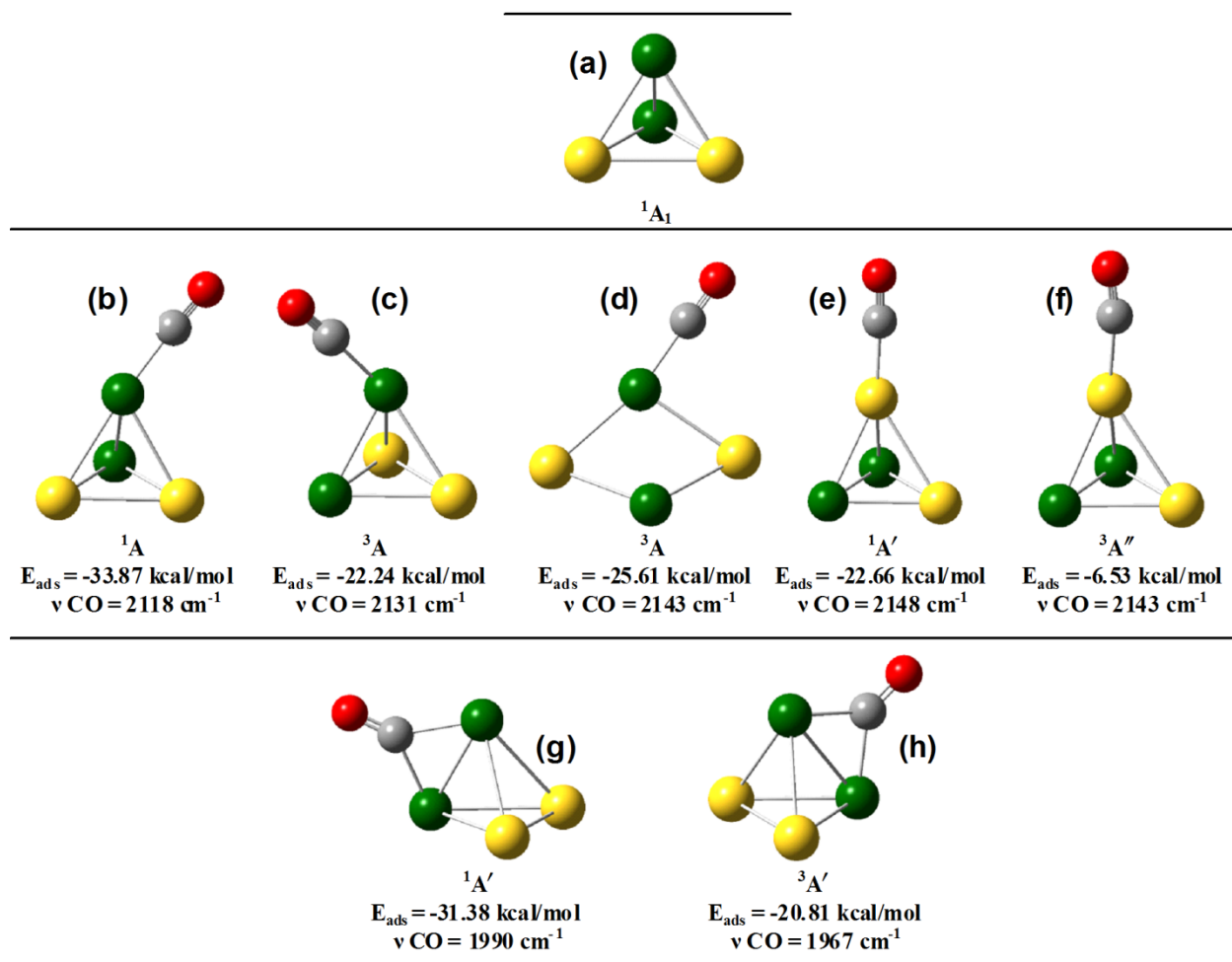**Figure 6.6.** Optimized structures of the Pd_2Au_2 clusters: (a) initially (singlet) and (b) CO on-top Pd (singlet), (c) CO on-top Pd (triplet), (d) CO on-top Pd (triplet, planar), (e) CO on-top Au (singlet), (f) CO on-top Au (triplet), (g) CO bridging PdPd (singlet), and (h) CO bridging PdPd (triplet). Palladium, gold, carbon, and oxygen are shown in green, yellow, grey, and red, respectively.

electrodes towards CO poisoning, CO stripping experiments were carried out in a 0.5 M H_2SO_4 solution. The results are presented in Figure 6.7.

There are two common characteristics in Figure 6.7a–c. First, the hydrogen desorption peaks of these electrodes are suppressed in the first positive-going scan due to pre-adsorbed CO blocking the active surface sites. Second, a current peak resulting from CO oxidation appear in the potential range from 0.0 to 0.8 V. The Pd catalyst (Figure 6.7a) displays a very sharp CO oxidation peak centered at approximately 675 mV, indicating that all of the adsorbed CO is rapidly oxidized at this potential. In the first forward scan of the PdAu CV (Figure 6.7b), the entire hydrogen desorption peak is not suppressed. This shows that CO did not adsorb to all of the surface sites of the PdAu catalyst. Also, the CO oxidation peak is significantly small compared to the pure Pd peak. The hydrogen adsorption/desorption peaks of PdAu are notably larger than those of Pd, demonstrating that Au must have the opposite adsorption energy effect on Pd for hydrogen than carbon monoxide. The CV for PdPt (Figure 6.7c) shows some catalytic improvement towards the oxidation of CO compared to pure Pd. There is a shoulder beginning at around 75 mV on the broad CO oxidation peak centered at 550 mV. This shift to a much lower potential as well as the onset shoulder suggests that CO is being oxidized in two steps, both of which are slower and are yet, energetically favoured relative to Pd.

The oxidation of adsorbed CO is a common method to determine the electroactive surface area of catalysts for electrochemical measurements.[35] The CO oxidation charge, Q_{CO}, can be determined by integrating the area under the CO oxidation peaks in the CVs, and this charge is proportional to the amount of CO which has been adsorbed to the catalyst surface. The Q_{CO} for Pd, PdAu and PdPt, are 19.67, 7.93 and 23.18 mC/cm^2, respectively. These values can be explained using the possible binding sites for CO on these catalysts as well as their
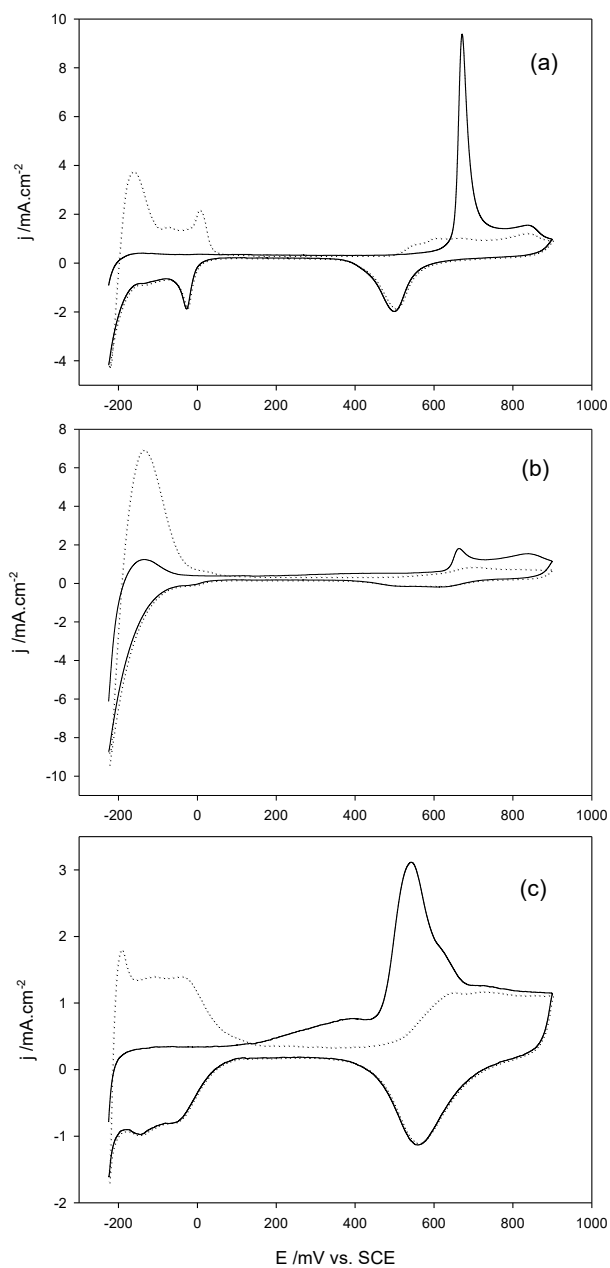
Figure 6.7. Cyclic voltammograms of CO stripping on the prepared electrodes: (a) Pd; (b) PdAu; and (c) PdPt. Two cycles of the CV were recorded for each electrode in 0.5 M H_2SO_4 at a potential scan rate of 20 mV/s. The first cycle is shown with solid line and the second cycle with a dotted line.

106

respective adsorption binding energies (Figures 6.4-6.6) obtained from the DFT calculations. For pure Pd, all three binding sites are possible (on-top, bridging, and hollow), although the hollow site has the strongest interaction with CO. On PdPt, all sites are possible with the strongest CO adsorption interaction with single Pt atoms, followed by a bridge between two Pt atoms, and then on-top single Pd atoms. The preferential hollow binding site for pure Pd requires three Pd atoms per CO ligand which limits the CO coverage on the surface, as compared to the preferential on-top and bridging sites for PdPt which require one and two atoms per CO ligand, respectively. For PdAu, on the other hand, all hollow sites are unattainable and the bridging site is limited to two Pd atoms adjacent to each other. Because of the limited number of binding sites on PdAu, Q_{CO} is smallest for this electrocatalyst.

6.8 *In situ* Electrochemical ATR-FTIR Study of Surface Adsorbed CO

There has been a lot of work done in the past to determine which Pd sites are preferential for CO adsorption.[26,36-39] Theoretical studies suggest that CO is adsorbed most strongly to the three-fold hollow site,[12,40] whereas experimental spectroscopy has shown that the surface site is dependent on the coverage of CO on the surface of Pd.[37-39] On the basis of vibrational spectroscopy, CO is known to adsorb at 3-fold hollow sites of well-prepared Pd(111) when the coverage is up to half a monolayer (v ~1895 cm^{-1}). When the coverage is greater than half a monolayer, CO is preferentially bridge-bonded (~1960 cm^{-1}) with a small amount being located at on-top sites (~2090 cm^{-1}).[37-39] The C-O stretching frequency is highly sensitive to the nature of the binding site and its electronic configuration.[26] This is seen with the DFT-predicted frequencies having values ranging from 2097 cm^{-1} to 2148 cm^{-1} for on-top sites. Infrared Reflection-Adsorption Spectroscopy (IRAS), using CO as a probe, is an effective technique for investigating alloying effects of metal catalysts.[47] The presence or absence of characteristic CO

stretches can be used to monitor adsorption sites on the surface, providing insight into the ensemble (geometric) effect. The CO vibrational frequency shift can be used to identify changes in the interaction between the substrate and CO molecules, which reflect the electronic modifications of the substrate surface induced by the second metal (the ligand effect).[41] By comparing the results obtained from theoretical simulations in this study to those obtained from experimental ATR-FTIR we are able to see what sites are preferential for CO to bind to Pd-alloys.

Shown in Figure 6.8 are the ATR-FTIR spectra for CO adsorbed to Pd, PdAu, and PdPt. For pure Pd, a majority of the CO is bridge-bonded, as witnessed by the intensity of the peak at 1957 cm^{-1}. Small amounts of CO appear to be bonded to both on-top sites (2068 cm^{-1}) and hollow sites (1908 cm^{-1}). For the PdPt alloy, most of the CO is bonded on-top single metal atoms with a C-O stretch of 2067 cm^{-1}. Upon first glance, it may seem that the other small peak at 1866 cm^{-1} would be due to CO adsorbed to hollow sites if comparing it to the Pd spectra, since this is close to the experimental hollow site adsorption of CO on Pd.[37-39] When examining the calculations carried out for the Pd$_2$Pt$_2$-CO cluster (Figure 6.5), however, it is found that the bridging C-O stretches are shifted to lower values relative to the Pd$_4$-CO (Figure 6.4). Accordingly, the peak at 2067 cm^{-1} can be assigned to CO adsorbed linearly to Pt atoms and the peak at 1866 cm^{-1} can be assigned to CO adsorbed to sites bridging two Pt atoms or one Pd atom and one Pt atom. Consistent with the DFT calculations, the addition of Au to Pd completely limits CO adsorption to on-top sites (2076 cm^{-1}) and bridging sites (1950 cm^{-1}). The hollow sites are completely excluded due to the weak adsorption energy of CO on Au.
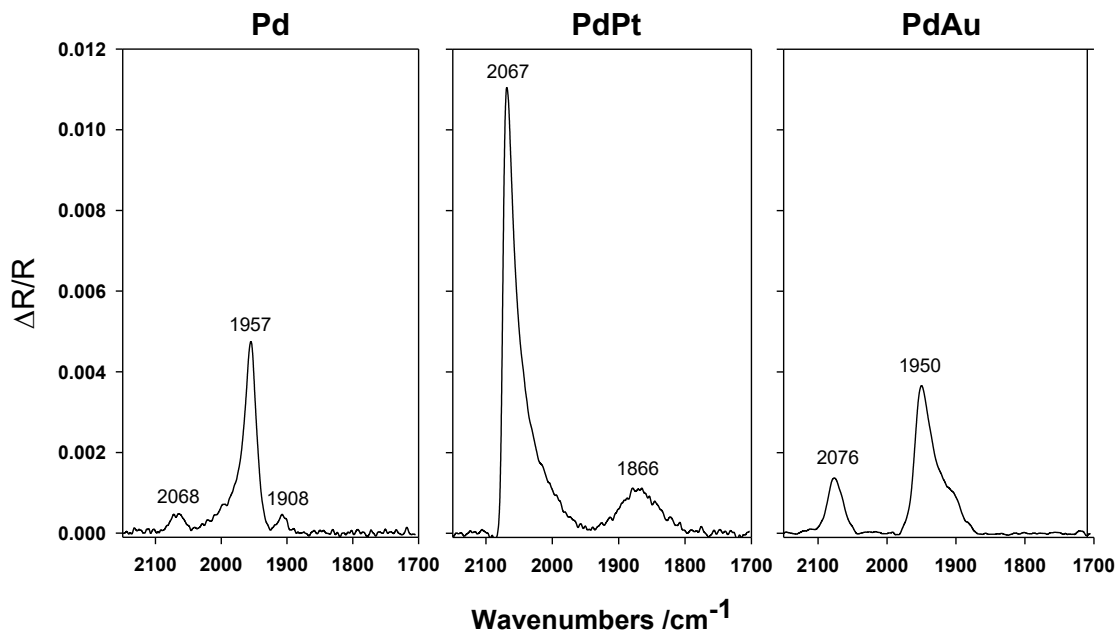
Figure 6.8. *In situ* electrochemical ATR-FTIR spectra for the oxidation of CO adsorbed to the surfaces of Pd, PdPt, and PdAu at a potential of -0.1 V. The spectra recorded at -0.2 V were used as reference.

In order to judge if the 4-atom clusters are a good model for CO adsorption onto transition metals, the experimental values for the C-O stretch frequencies obtained here from ATR-FTIR for pure Pd nanoparticles were compared to those obtained by the DFT calculations. Table 6.3 is a compilation of the CO stretching frequencies obtained in this study for Pd using the Pd_4-CO clusters and ATR-FTIR spectroscopic techniques, as well as experimental and theoretical results by others.[12,26,39,42] It was found that the theoretical values were almost identical to our experimental values for bridging CO (1960 cm^{-1} vs. 1957 cm^{-1}), but were slightly different for on-top (2121/2118 cm^{-1} vs. 2068 cm^{-1}) and significantly different for hollow site adsorbed CO (1787 cm^{-1} vs. 1908 cm^{-1}). When examining the results of other groups, it can be seen that there is a much larger range of the CO stretching frequency for on-top (1994-2122 cm^{-1}),

bridging (1855-1967 cm^{-1}), and hollow (1735-1898 cm^{-1}) sites. The predicted DFT harmonic

frequencies for each of the adsorption sites lie within the range of work by others. The CO

frequencies obtained by ATR-FTIR lie in these ranges as well for ontop and bridging sites, and

our hollow site frequency is slightly higher. Table 6.3 shows that the value of the ν(CO) can vary

with different test conditions. However, from the results obtained here, small cluster models can

be an excellent method of determining the adsorption sites for CO ligands when examining an IR

spectrum.

Table 6.3. Comparison of theoretical and experimental C-O stretching frequencies on Pd.

CO Binding Site	Pd$_4$ cluster (Spin)	ATR-FTIR	Other Studies
Ontop	2121/2118 cm^{-1} (S/T)	2068 cm^{-1}	2050-2058 cm^{-1} [a] 2000 cm^{-1} [b] 2086-2107 cm^{-1} [c] 1994-2122 cm^{-1} [d]
Bridged	1960 cm^{-1} (T)	1957 cm^{-1}	1900-1955 cm^{-1} [a] 1855 cm^{-1} [b] 1925-1958 cm^{-1} [c] 1875-1967 cm^{-1} [d]
Hollow	1787 cm^{-1} (S)	1908 cm^{-1}	1815-1870 cm^{-1} [a] 1735 cm^{-1} [b] 1866-1898 cm^{-1} [c] 1787-1791 cm^{-1} [d]

[a]   Attenuated total reflection surface enhanced infrared reflection absorption spectroscopy[42]
[b]   Infrared multiple photon dissociation spectroscopy of anionic and cation Pd[26]
[c]   Vibrational sum frequency generation spectroscopy[39]
[d]   DFT cluster model[12]

6.9 Summary

In summary, DFT calculations were carried out for CO bonded to individual atoms of the

transition metals. It was found that this method, although not a good model for actual adsorption

energies, is very efficient for comparing the strength of CO adsorption to different metals.

Calculations were also performed for Pd$_4$-CO, Pd$_2$Pt$_2$-CO, and Pd$_2$Au$_2$-CO. The preferential sites

of CO attachment were located and C-O stretching frequencies were obtained. Because CO is more strongly adsorbed to Pt than Pd, in the Pd_2Pt_2 cluster, the preferred sites were on-top Pt atoms. In the Pd_2Au_2 cluster, the hollow sites were completely avoided as a result of the weak interaction between Au and CO. By combining metals in an appropriate manner, the adsorption sites of CO can be controlled. Experimental electrochemical results confirmed the weaker interaction of CO with PdAu than Pd and showed that PdPt has a greater catalytic activity for the electrochemical oxidation of CO. ATR-FTIR was used as a tool to compare the C-O stretching frequencies obtained from the DFT calculations to those on actual nanostructured Pd, PdAu and PdPt surfaces. The simplistic cluster model computational technique described here can be adapted to many other catalytic adsorbate reactants or intermediates as well as countless adsorbent catalysts, allowing for easy screening of catalyst properties.

References

1. M.M. Sadek, L. Wang, *J. Phys. Chem. A* **2006**, *110*, 14036.

2. M. Oana, R. Hoffmann, H.D. Abruña, F. DiSalvo, F. J. *Surf. Sci*. **2005**, *574*,1.

3. N. de-los-Santos-Álvarez, L.R. Alden, E. Rus, H. Wang, F.J. DiSalvo, H.D. Abruña, *J. Electroanal. Chem*. **2009**, *626*, 14.

4. C. Ranjan, R. Hoffmann, F.J. DiSalvo, H.D. Abruña, *J. Phys. Chem. C* **2007**, *111*, 17357.

5. Y. Shimodaira, T. Tanaka, T. Miura, A. Kudo, H. Kobayashi, *J. Phys. Chem. C* **2007**, *111*, 272.

6. E.S. Steigerwalt, G.A. Deluga, C.M. Lukehart, *J. Phys. Chem. B* **2002**, *106*, 760.

7. K. Koczkur, Q. Yi, A. Chen, *Adv. Mater.* **2007**, *19*, 2648.

8. K.W. Park, Y.E. Sung, *J. Phys. Chem. B* **2005**, *109*, 13585.

9. M. Watanabe, S. Motoo, *J. Electroanal. Chem.* **1975**, *60*, 267.

10. Z. Liu, J.Y. Lee, W. Chen, M. Han, L. Gan, M. *Langmuir* **2004**, *20*, 18.

11. J. Wang, R.M. Asmussen, B. Adams, D.F. Thomas, A. Chen, *Chem. Mater.* **2009**, *21*, 1716.

12. V. Bertin, E. Agacino, R. Lopez-Rendon, E. Poulain, *J. Mol. Struct.: THEOCHEM* **2006**, *796*, 243.

13. H. Liu, A. Manthiram, *Electrochem. Commun*. **2008**, *10*, 740.

14. B. Lim, M. Jiang, P.H.C. Camargo, E.C. Cho, J. Tao, X. Lu, Y. Zhu, Y. Xia, *Science* **2009**, *324*, 1302.

15. R. Wang, S. Liao, S. Ji, *J. Power Sources* **2008**, *180*, 205.

16. R.S. Jayashree, J.S. Spendelowa, J. Yeomb, C. Rastogi, M.A. Shannon, P.J.A. Kenis, *Electrochimica Acta* **2005**, *50*, 4674.

17. R. de Souza Monteiro, L.W.C. Paes, J.W. de M. Careiro, D.A.G. Aranda, *J. Clust. Sci*. **2008**, *19*, 601.

18. M. Lischka, C. Mosch, A. Groß, *Surf. Sci*. **2004**, *570*, 227.

19. J.C. Davies, J. Bonde, Á. Logadottir, J.K. Nørskov, I. Chorkendorff, *Fuel Cells 05* **2005**, *4*, 429.

20. M. Neurock, *J. Catal*. **2003**, *216*, 73.

21. P.J. Roach, W.H. Woodward, A.W. Castleman Jr., A.C. Reber, S.N. Khanna, *Science* **2009**, *323*, 492.

22. G.E. Johnson, R. Mitrić, V. Bonačić-Koutecký, A.W. Castleman Jr., *Chem. Phys. Let*. **2009**, *475*, 1.

23. K.M. Neyman, R. Sahnoun, C. Inntam, S. Hengrasmee, N. Rsch, *J. Phys. Chem. B* **2004**, *108*, 5424.

24. L. Chen, B. Chen, C. Zhou, J. Wu, R.C. Forrey, H. Cheng, *J. Phys. Chem. C*, **2008**, *112*, 13937.

25. C.D. Zeinalipour-Yazdi, A.L. Cooksy, A.M. Efstathiou, *Surf. Sci*. **2008**, *602*, 1858.

26. P. Gruene, A. Fielicke, G. Meijer, D.M. Rayner, *Phys. Chem. Chem. Phys*. **2008**, *110*, 6144.

27. J. Wang, P. Holt-Hindle, D. MacDonald, D.F. Thomas, A. Chen, *Electrochim. Acta* **2008**, *53*, 6944.

28. A.M. Joshi, M.H. Tucker, W.N. Delgass, K.T. Thomson, *J. Chem. Phys*. **2006**, *125*, 194707.

29. G. Blyholder, *J. Phys. Chem. B*. **1964**, *68*, 2772.

30. J. Zhang, H. Jin, M.B. Sullivan, F.C.H. Lim, P. Wu, *Phys. Chem. Chem. Phys*. **2009**, *11*, 1441.

31. N. Tian, Z.-Y. Zhou, S.-G. Sun, *J. Phys. Chem. C* **2008**, *112*, 19801.

32. B.L. Moroz, P.A. Pyrjaev, V.I. Zaikovskii, V.I. Bukhtiyarov, *Catal. Today* **2009**, *144*, 292.

33. F. Illas, N. López, J.M. Ricart, A. Clotet, J.C. Conesa, M. Fernández-Garcia, *J. Phys. Chem. B* **1998**, *102*, 8017.

34. J. Szanyi, W.K. Kuhn, D.W. Goodman, *J. Vac. Sci. Technol. A*. **1993**, *11*, 1969.

35. C. Bock, B. MacDougall, *J. Electrochem. Soc.* **2003**, *150*, E377.

36. I.V. Yudanov, R. Sahnoun, K.M. Neyman, N. Rsch, J. Hoffmann, S. Schauermann, V. Johnek, H. Unterhalt, G. Rupprechter, J. Libuda, H.-J. Freund, *J. Phys. Chem. B* **2003**, *107*, 225.

37. H. Unterhalt, G. Rupprechter, H.-J. Freund, *J. Phys. Chem. B* **2002**, *106*, 356.

38. G. Rupprechter, H. Unterhalt, M. Morkel, P. Galletto, L. Hu, H.-J. Freund, *Surf. Sci.* **2002**, *502-503*, 109.

39. M. Morkel, H. Unterhalt, M. Salmeron, G. Rupprechter, H.-J. Freund, *Surf. Sci*. **2003**, *532*, 103.

40. E.D. German, M. Sheintuch, *J. Phys. Chem. C* **2008,** *112*, 14377.

41. T. Wei, J. Wang, D.W. Goodman, *J. Phys. Chem. C*, **2007**, *111*, 8781.

42. H. Miyake, T. Okada, G. Samjeskéb, M. Osawa, *Phys. Chem. Chem. Phys*. **2008**, *10*, 3662.

Chapter 7

Summary and Future Work

Pd-based nanomaterials possess unique catalytic and hydrogen absorbing properties which make them very attractive towards the development of technologies in a hydrogen-based economy. Hydrogen purification, hydrogen storage, and fuel cell catalysis are among the main applications in which Pd-containing nanomaterials show great potential. Two different techniques, a hydrothermal reduction method and a room-temperature impregnation method, were used to synthesize the Pd-containing nanomaterials examined in this work. All the synthesized Pd-based nanomaterials were characterized using a combination of surface analytical techniques, electrochemical methods, gas adsorption, and DFT calculations. The major results obtained during the course of this M. Sc. project are summarized below.

7.1 Hydrogen Electrosorption into PdCd Nanostructures

Hydrogen absorbing materials are crucial for both the purification and storage of hydrogen. Pd and Pd-based alloys have been studied extensively for their use as both hydrogen dissociation catalysts and hydrogen selective membrane materials. It is known that incorporating metal atoms of different sizes into the Pd lattice has a major impact on the hydrogen absorption process. In Chapter 3, hydrogen electrosorption into nanostructured Pd-Cd alloys with 0 at.% to 20 at.% was studied. The low cost of Cd makes it an attractive material to combine with Pd for hydrogen sorption. A combination of chronoamperometry and cyclic voltammetric experiments were used to determine the ratio of the H/(Pd+Cd) and the kinetics of hydrogen sorption into these Pd-Cd alloys at different potentials. It was found that the maximum H/(Pd+Cd) value was 0.66 for pure Pd, and this decreased with increasing the amount of Cd. A large expansion of the

lattice constant due to the α (solid solution) to β-phase (metal hydride) hydrogen transition can cause cracking of the membrane. For the Pd-Cd nanostructures, the α to β phase transition was determined to be the slowest step in the absorption process, and was practically eliminated when the optimum amount of Cd atoms was doped (i.e., $Pd_{0.85}Cd_{0.15}$). Increasing Cd content allowed for a higher hydrogen solubility into the Pd-Cd nanostructures, particularly at the higher potentials (the α phase region), and increased the kinetics of hydrogen absorption. The faster kinetics, along with the decrease in the phase transition of hydrogen sorption into the Pd-Cd nanostructures when compared to pure Pd, makes the Pd-Cd nanostructures attractive for use as a hydrogen dissociation catalytic capping layer for other metal hydrides or as a hydrogen selective membrane.

7.2 Hydrogen Spillover from Pd-based Nanoparticles to Activated Carbon

High surface area carbon materials are promising for low-temperature storage of hydrogen by physisorption. In order to achieve acceptable hydrogen capacities at ambient temperature, chemisorption must come into play. The dispersion of transition metal catalysts to carbon materials can enhance the ambient temperature adsorption capacity of carbon materials via the hydrogen spillover mechanism. In Chapter 4, the hydrogen adsorption properties of a commercially available activated carbon were studied at 77 K and room temperature using a volumetric gas adsorption technique. By dispersing catalysts onto surfaces of the activated carbon, three different hydrogen dissociation catalysts (Pd, PdAg, and PdCd) were examined. The surface composition of these metal dispersed carbon materials was analyzed using X-ray photoelectron spectroscopy and the specific surface areas and pore sizes were obtained using N_2 adsorption/desorption. At 77 K, the catalysts have no effect, and the hydrogen capacity of the materials is strictly related to the specific surface area. At room temperature, hydrogen spillover

was observed from the catalysts to the carbon material, and the hydrogen capacity depends on the adsorption strength of the catalyst particle surface atoms which is supported by DFT calculations. The PdCd catalyst has a hydrogen spillover enhancement of 108%.

7.3 Electrochemical Reduction of Hydrogen Peroxide on Pd-Pt Catalysts

In Chapter 5, carbon-supported PdPt catalysts were studied and found to outperform both Pt and Pd in terms of hydrogen peroxide reduction activity. The preparation of these catalysts involved a treatment process of the carbon support material to enhance the hydrophillicity, and a room temperature reduction of the metal precursors with sodium borohydride. The surfaces of the PdPt/C catalysts were characterized using transmission electron microscopy, energy dispersive X-ray spectroscopy, X-ray diffraction, and specific surface area analysis. The electrocatalytic activities of the synthesized catalysts were analyzed using a rotating disk electrode system with a combination of linear sweep voltammetry and chronoamperometry in an acidic electrolyte. The catalyst of composition $Pd_{0.25}Pt_{0.75}$ had the greatest activity towards hydrogen peroxide electroreduction.

7.4 CO Adsorption on Pd-based Nanomaterials

In Chapter 6, the adsorption of CO molecules onto small metal clusters was studied using theoretical density functional theory calculations and experimental electrochemical and ATR-FTIR techniques. The adsorption strengths and CO vibrational stretching frequencies (ν(CO)) were calculated and analyzed for clusters of the form M-CO for all of the period 4, 5, and 6 d-block transition metals. No correlation was found between the adsorption energy (E_{ads}) and ν(CO), although a direct link between ν(CO) and the population of d orbitals of the metal was observed. All possible binding sites for CO on clusters of the form Pd_4-CO, Pd_2Pt_2-CO, and

Pd_2Au_2-CO were determined and the corresponding E_{ads} and $\nu(CO)$ were examined. Pure Pd and bimetallic PdPt and PdAu nanostructures were fabricated and used as catalysts for the electrochemical oxidation of CO. The relative quantities of CO molecules adsorbed to surface of the catalysts decrease in the order of PdPt > Pd > PdAu. The location of $\nu(CO)$ bands of CO adsorbed onto the nanostructured catalysts were determined by means of ATR-FTIR, and were found to have values close to the predicted DFT harmonic frequencies. This work suggests that DFT calculations on very small metal clusters M_n-CO ($n \leq 4$) can be an effective and simplistic way of screening catalysts for their CO adsorbing properties.

7.5 Closing Remarks and Future Work

In summary, PdCd nanostructures have been fabricated for the first time and their hydrogen electrosorption properties have been analyzed. The α to β phase transition was determined to be the slowest step in the absorption process, and was practically eliminated by incorporating 15% Cd. This resulted in more hydrogen present in the α phase region along with faster sorption kinetics.

From hydrogen gas absorption/adsorption experiments, hydrogen spillover was observed for Pd, PdAg, and PdCd nanoparticles to activated carbon. The $Pd_{0.85}Cd_{0.15}$ nanoparticles again showed the best performance with a hydrogen capacity enhancement of 108% due to spillover. This enhancement is attributed to hydrogen dissociation of H_2 coupled with the weak adsorption strength of hydrogen atoms to Cd.

The use of hydrogen peroxide as the oxidant to replace oxygen in low temperature fuel cells has also been explored. A study of carbon-supported PdPt catalysts for hydrogen peroxide reduction showed that $Pd_{0.25}Pt_{0.75}$ nanoparticles have a high activity for the electrochemical reduction of hydrogen peroxide. This PdPt catalyst outperforms both Pd and Pt nanoparticles.

The effect of carbon monoxide, a catalytic poisoning species, on Pd, PdPt, and PdAu nanostructures was studied. It was found that the relative quantities of CO molecules adsorbed to surface of the catalysts decrease in the order of: PdPt > Pd > PdAu. This phenomenon has been further verified using simple DFT calculations on small metal clusters.

The results of this work indicate that PdCd nanostructures are promising for application as hydrogen selective membrane materials or hydrogen dissociation catalysts for other hydrogen storage materials. PdPt nanoparticles have high catalytic activity for hydrogen peroxide reduction. For oxidation catalysts, poisoning by CO can be limited by alloying Pd with a metal in which CO is weakly adsorbed, such as Au. The adsorption strength can easily be determined using DFT calculations.

It appears that for all hydrogen absorbing applications there are two common issues which should be the focus of research: hydrogen embrittlement and poisoning species. In addition, hydrogen solubility plays an important kinetic role in some applications. For hydrogen dissociation applications (hydrogen storage and catalysts), where surface interactions are of greater concern than bulk phase absorption, the adsorption strength is the most crucial factor. All of these properties can be modified by alloying Pd with other metals. More studies on the alloying effect would help us gain an understanding between the electronic and geometric results of alloying in order to develop high-performance Pd-based catalysts for a hydrogen-based economy.